Measuring the anti-quark contribution to the proton spin using parity violating W production in polarized proton proton collisions

A Dissertation presented

by

Ciprian Gal

to

The Graduate School

in Partial Fulfillment of the

Requirements

for the Degree of

Doctor of Philosophy

in

Physics

Stony Brook University

August 2014

Stony Brook University
The Graduate School

Ciprian Gal

We, the dissertation committee for the above candidate for the
Doctor of Philosophy degree, hereby recommend
acceptance of this dissertation

Abhay Deshpande - Dissertation Advisor
Professor, Department of Physics and Astronomy

Dmitri Tsybychev - Chairperson of Defense
Professor, Department of Physics and Astronomy

Tom Allison
Professor, Department of Physics and Astronomy

Martin Purschke
Physicist, Brookhaven National Laboratory

Jianwei Qiu
Senior Physicist, Brookhaven National Laboratory
Brookhaven Professor, C.N. Yang Institute for Theoretical Physics

This dissertation is accepted by the Graduate School

Charles Taber
Dean of the Graduate School

Abstract of the Dissertation

Measuring the anti-quark contribution to the proton spin using parity violating W production in polarized proton proton collisions

by

Ciprian Gal

Doctor of Philosophy

in

Physics

Stony Brook University

2014

Since the 1980s the spin puzzle has been at the heart of many experimental measurements. The initial discovery that only ∼30% of the spin of the proton comes from quarks and anti-quarks has been refined and cross checked by several other deep inelastic scattering (DIS) and semi inclusive DIS (SIDIS) experiments. Through measurements of polarized parton distribution functions (PDFs) the individual contributions of the u, d, $\bar{u}$, $\bar{d}$, quarks have been measured. The flavor separation done in SIDIS experiments requires knowledge of fragmentation functions (FFs). However, due to the higher uncertainty of the anti-quark FFs compared to the quark FFs, the quark polarized PDFs ($\Delta u(x)$, $\Delta d(x)$) are significantly better constrained than the anti-quark distributions ($\Delta\bar{u}(x)$, $\Delta\bar{d}(x)$). By accessing the anti-quarks directly through W boson production in polarized proton-proton collisions ($u\bar{d} \to W^+ \to e^+/\mu^+$ and $d\bar{u} \to W^- \to e^-/\mu^-$), the large FF uncertainties are avoided and a cleaner measurement can be done. The parity violating single spin asymmetry of the W decay leptons can be directly related to the polarized PDFs of the anti-quarks. The $W^{\pm} \rightarrow e^{\pm}$ measurement has been performed with the PHENIX central arm detectors at $\sqrt{s} = 510$ GeV at the Relativistic Heavy Ion Collider (RHIC) and is presented in this thesis.

Approximately 40 pb^{-1} of data from the 2011 and 2012 was analyzed and a large parity violating single spin asymmetry for $\mathrm{W}^{\pm}$ has been measured. The combined data for 2011 and 2012 provide a single spin asymmetry for both charges:

- W^{+}: $-0.27 \pm 0.10(stat) \pm 0.01(syst)$
- W^{-}: $0.28 \pm 0.16(stat) \pm 0.02(syst)$

These results are consistent with the different theoretical predictions at the 1σ level.

The increased statistical precision enabled and required a more careful analysis of the background contamination for the this measurement. A method based on Gaussian Processes for Regression has been employed to determine this background contribution. This thesis contains a detailed description of the analysis together with the asymmetry results and future prospects.

To Cecilia and Valerian, for their unwavering support
and innumerable sacrifices.

Table of Contents

Contents

List of Figures

List of Tables

Acknowledgements

I would like to start by thanking my advisor Abhay Deshpande for his years of support and guidance. Like many of his students, I have benefited greatly from all the discussions about my analysis but more importantly discussions about the bigger picture in Nuclear Physics. One of the main reasons I have reached this level of understanding is the way he asked questions. Varying and widening the narrow scope of my problems, these questions involved solving much more than just my problem of the week. Each and every one of them was designed to make me reach an answer myself and thus take one further step to becoming a real physicist.

Years have passed since I have joined the Physics Department and the Nuclear Experimental Group at Stony Brook. Over and above the experiences and lesson I have learned here the friendly (almost family like) atmosphere that I found in throughout the department and the group stands as the most important thing. Under no circumstances can I imagine a better place to attempt the long and arduous trek towards Ph.D. Starting from everyone in the Main Office that helped me disentangle all the paperwork (always with a smile) and enabled me to do research, going on to colleagues and fellow students (particularly Andrew Manion and Paul Kline) that helped me pass those daily small bumps in my analysis, to postdocs in the group (especially Swadhin Taneja) who taught me so much, to my closest friends Betul and David, I cannot thank everyone enough. Anyone would be fortunate to have you in their lives.

None of this work would be possible without the PHENIX collaboration. Going through the list of people who make it such a great experiment and why, would require a whole chapter in this thesis. However, I would like to especially thank everyone involved in the day to day operations of the 1008 complex (especially John Haggerty, Martin Purschke, Chris Pinkenburg and Ed Desmond). What they do is often taken for granted, but without them PHENIX would grind to a halt. Almost as important to this analysis is the help provided by the PHENIX spin and W analysis groups. The careful scrutiny and attention to all aspects of the analysis provided by the members has been invaluable to bringing this work where it is now. Particularly, discussion with Kensuke Okada and Sasha Bazilevsky have been vital to

pushing this result through. A special thank you to Sanghwa for all the help. It would be remiss of me to not mention two great scientists that have guided and mentored me throughout my years at PHENIX: Kieran Boyle and Joseph Seele. They always took time to talk to me, understand what I was doing and suggest new ways to improve and refine my results.

Before I end, I need to thank the people I left behind in Europe. Every time one of the great friends I made during my undergraduate years at Jacobs kept in touch, was a joy. My family has provided me with more support that I probably deserved on a regular basis. In many ways this work is a testimony of their firm belief in me.

Nothing will deter me from trying to repay each and everyone of you. Everyone mentioned here (and people I have somehow missed) has had a major impact not only on my life as a researcher but also on me as a human being: thank you!

1 Introduction

This thesis is focused on the single spin asymmetry of electrons and positrons measurement in the PHENIX central arms.

The first chapter introduces Quantum Chromodynamics (QCD) and gives a motivation for this measurement. Following the chronological developments a series of both theoretical and experimental breakthroughs in the field are discussed. QCD is a perfect example how experiment and theory work hand in hand to provide insights and push understanding further. After initial experimental discovery of larger number of fundamental particles, theoretical models give an elegant way to explain all the new particles by introducing a set of new fundamental particles called quarks. The development of deep inelastic scattering provided a confirmation of the model but also give evidence that it is still incomplete. The momentum fractions carried by quarks turned out to be insufficient to account for the total momentum of hadrons. Like the quarks, the gluon was predicted by theory and shortly after discovered by experiments setting the basis for what is now the description of the strong interaction (QCD). Further refinements of the parton momentum distribution function measurements eventually lead to taking into account of the spin direction of these partons. Again experimental evidence collided with theoretical predictions when the expectation that the spin 1/2 quarks make up most of the proton spin was disproven. This last conundrum (called the Spin Puzzle) is still being investigated to this day. Here is where the measurement presented in this thesis provides some insights to constrain the anti-quark polarized parton distribution functions.

The second chapter focuses on the experimental setup at the Relativistic Heavy Ion Collider (RHIC) and PHENIX central arm spectrometer. RHIC is, as it's name suggests a heavy nuclei collider. It was the place of the discovery of the quark gluon plasma and has made strides towards describing the properties of this new state of matter. Along side the heavy ion program, through polarizations of the proton proton collisions (originally needed as a refference for the heavy nuclei collisions), a whole new physics program has been added. This chapter presents a general description of the production and acceleration of the polarized proton beams in RHIC. Following, the PHENIX experimental subsystems are detailed with a particular focus on how they are used for this measurement. The PHENIX central arms provide excellent electron energy resolution however the lack of 2π coverage in the θ polar angle makes this measurement a challenging one.

The third chapter gives a detailed description of the measurement procedure and results. It is separated into three parts: a) the data obtained in 2011 and 2012, b) the detector status and behavior during the data taking periods and c) the measurement procedures and results. The first part gives information on two of the three components needed for a single spin asymmetry measurement: relative luminosity and beam polarization. The second part of the data analysis shows quality assurance plots from the main detector subsystems needed for this measurement. The last, and most challenging, component needed for the asymmetry measurement (the polarization separated yields) is presented in the third part. The transverse momentum spectrum of the electron/positron is obtained with the telltale appearance of a Jacobian peak. Finally the background dilution factor and final asymmetry values for this measurement are obtained.

The last chapter of this thesis focuses on a discussion and interpretation of the results. Theoretical predictions are presented for the single spin asymmetry and the prospects of constraining the anti-quark polarized parton distributions functions are discussed.

A series of appendices that support this thesis (but are not necessary for this measurement) can be found at the end of this thesis.

1.1 Quantum Chromodynamics

Being the two constituent parts of nuclei, protons and neutrons make up almost all of the mass of the known matter in the universe. As such, having a full understanding of their properties and interactions is essential to our knowledge of the physical world.

With the advent of high energy (at the time) particle accelerators, the 1950s and 1960s saw a myriad of new *fundamental* particles being discovered (collectively called the Particle Zoo). These particles, dubbed hadrons, had similar properties with protons and neutrons however they had different masses or charges. All of this suggested the existence of an underlying symmetry. Gell-Mann and Zweig, in 1964 [9], introduced the constituent quark model. It suggested that all of these hadrons, including the proton and neutron, were in fact composite particles made out of elementary particles called quarks. These quarks had what some considered strange properties. They had fractional electric charge (in terms of electron charge) and could be combined in either pairs of quark anti-quark to produce what was called a meson, or in three quarks to produce a baryon. The proton and neutron were differentiated only by the replacement of a quark in the three quark composition (proton having a up-up-down (*uud*) configuration while the neutron being made out of *udd* quarks).

This underlying symmetry in the model was an SU(3) symmetry between the lightest three quarks: u (up quark), d (down quark) and s (strange quark). This symmetry holds to a large degree due to the very small differences between the masses of these quarks. The theory proved to be a great success, providing a clear explanation of the charge and magnetic moment of hadrons.

Experimental evidence for the existence of quarks was obtained through Deep Inelastic Scattering (DIS) experiments (the first being an experiment at SLAC in 1969 [10]). However, together with this came the realization that the momenta carried by charged particles (quarks) could only account for about half of the total proton momentum. Shortly after, Feynman proposed the parton model, where charged particles (quarks) were mediated by massless photon-like particles, which could explain the rest of the momentum of the proton. The photon-like particles, called gluons, mediated the interactions between color-charged particles. For example, gluons could split into quark anti-quark pairs, a quark and an anti-quark could annihilate to produce a gluon and a quark could radiate or observe a gluon and change its color charge. However, unlike the photon which is chargeless, the gluon has it's own color charge, meaning it can couple to other gluons.

The introduction of gluons and quark anti-quark pairs meant that quarks can be separated into two categories. The first type is called sea quarks, because through annihilation and pair production quarks appear and disappear inside hadrons all the time, forming something similar to a *sea*. The second is called valence quarks, quarks that would remain inside the proton if all possible pairs of quark anti-quark would produce gluons.

The color-SU(3) symmetry of the parton model, and the dynamics that it describes are the basis for Quantum Chromodynamics (QCD). QCD is part of the Standard Model for particle physics (one of the most successful theories to date). However, one question remained. There were no experimental measurements that showed the existence of colored objects, all of the particles measured so far had been color neutral. The answer to this color confinement comes from the theory behind QCD. A large part of this theory has parallels in Quantum Electrodynamics (the quantum theory of electromagnetism), however there are some significant differences. On top of the color charge of the gluon mentioned before, the most important difference is the fact that the coupling for the strong force α_s increases as the distance between interactiong partons becomes larger. This means that if a quark somehow is pushed a large distance (the dimension of a hadron size) away from the other quarks or gluons the energy in the field is sufficient to produce a quark anti-quark pair neutralizing the color charge of the newly formed system. Production of color neutral hadrons from quarks or gluons is called hadronization. The opposite case happens when quarks are very close together, each quark being asymptotically free.

Another consequence of the increase of α_s with distance is restrictions on how predictions can be made from QCD. In QED all calculations of amplitude integrals that involve intermediate vertices (other vertices except the initial and final scattering vertices) contain an additional factor of the coupling constant. The smallness of the coupling constant ($\alpha = 1/137$), means that these intermediate states can be truncated and calculations can be made up to a desired precision in powers of $alpha$. However, in QCD, α_s increases with distance, meaning that at large distances the coupling will be equally as important. In order for predictions to be made many intermediate states need to be considered. This is not possible right now, and so a framework of perturbative calculations (pQCD) is used where only short distance interactions are taken into account where α_s is small. Another way to think about this is related to the energy of an interaction. The energy scale μ^2 needed to probe at a small distance is very high. This means that α_s increases as the energy scale decreases. Usually an energy scale of $\mu^2 \gg 1$ GeV is considered safe for pQCD calculations (because $\alpha_s \ll 1$).

In order to be able to make accurate predictions these nonperturbative components of the calculations need to be handled somehow. This is where the Factorization Theorem comes into play. It states that processes can be separated cleanly into two parts: a) an initial state large distance part described by parton distributions functions and b) a small distance pertubartive, calculable part, which (like in QED) can be calculated to varying degrees of precision in terms of powers of α_s. For example in the typical DIS diagram shown in figure 1 the initial state of the proton is characterized by a momentum parton distribution function (P^μ) and a polarized parton distribution function (S) to give the spin information of the quarks and gluons. The amplitude of the interaction that happens at small distances between a particular parton (quark or gluon characterized by xP^μ and spin λ) with the lepton (characterized by 4-momentum k^μ and spin λ_l), through a virtual photon (γ^*) can be calculated using our current theoretical uncerstanding.

The nonperturbative component is obtained from experimental data and is assumed to be universal. That is, the distributions of partons (and their momenta) inside a proton are the same no matter what type of experiment you perform. This assumption has proved correct so far, but further experiments are being designed to test it.

1.2 Parton Distribution Functions

As stated above, the initial state of the hadron that is studied cannot be calculated precisely from first principles. Experimental measurements have been performed to study these initial states. The most effective have been the DIS experiments, where a large momentum is transferred from a lepton (generally an electron/muon, but DIS experiments with neutrino beams have also been performed) to a stuck quark or gluon, giving it enough energy to break away from the rest of the hadron (as is schematically drawn in figure 1). Great descriptions of DIS can be found in many textbooks or review articles (for example see [11] or [12]). A brief discussion is given here with the salient information for this thesis.

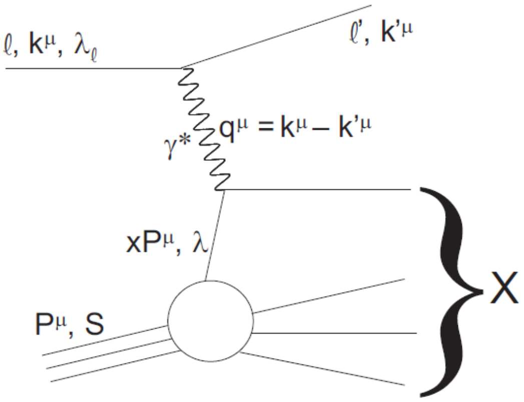

Figure 1: Deep inelastic scattering schematic (figure 1.2 in [1]).

By measuring cross sections of lepton on hadron targets, access can be gained to structure functions for that particular hadron. These structure functions depend on the energy exchange between the lepton and struck parton (Q^2) and the momentum fraction of the total hadron momentum (P)

carried by the struck quark (x). These variables are generally defined as:

$$Q^2 \equiv -\, q^2 \tag{1}$$

$$x \equiv \frac{Q^2}{2P \cdot q} \tag{2}$$

where q is the 4-momentum transferred from the lepton to the quark (it can be measured from the difference between the initial and final state lepton).

The $F_1(x, Q^2)$ and $F_2(x, Q^2)$ structure functions are frame invariant and dimensionless and can be written as:

$$F_2(x, Q^2) = 2xF_1(x, Q^2) = x \sum_f e_f^2 \left(q_f(x) + \bar{q}_f(x)\right) \tag{3}$$

where f is the flavor of the quark being summed over, e_f^2 is the charge and $q_f(x)$ is the momentum distribution for a quark of flavor f inside the hadron. These momentum distributions, called parton distribution functions (PDF), are exactly what is needed to be able to make predictions in hard scattering processes. Similarly to the definition of quark PDFs, gluon PDFs can be defined, although they are not directly accessible to DIS experiments (the colorless photon does not interact directly with the chargeless gluon, needing an intermediate quark resulting in processes that are suppressed by α_s).

A set of simple relations can be obtained by integrating over the momentum fractions of the partons inside a proton:

$$\int_0^1 x \left(\sum_f \left(q_f(x) + \bar{q}_f(x)\right) + g(x) \right) dx = 1 \tag{4}$$

$$\int_0^1 \left(u(x) - \bar{u}(x)\right) dx = 2 \tag{5}$$

$$\int_0^1 \left(d(x) - \bar{d}(x)\right) dx = 1 \tag{6}$$

$$\int_0^1 \left(q_h(x) - \bar{q_h}(x)\right) dx = 0 \tag{7}$$

where q_h is representative for all the other quarks besides u and d. The first equation (4) states that all of the momentum of the proton can be found by summing up all the fractional momenta of the partons. The last three equations are just an indication of the *uud* valence quark structure of the proton.

A representative set of the world data for the structure function F_2^p for the proton can be seen in figure 2.

The proton PDFs can be extracted from this data for a particular combination of (x, Q^2). Using the DGLAP ([13–15]) set of equations one can relate PDFs at a particular Q^2 to PDFs at any different Q'^2 scale. These equations make use of perturbativly calculable splitting functions (that give information on how the gluon splits into a quark anti-quark or gluon pair, or how a quark radiates a gluon). This process is called evolution and is a consequence of the pQCD framework.

Evolution allows for another type of analysis to be done with the DIS data. A so-called *global analysis* can be performed on the data by constraining a PDF functional form using most of the world available data at the same time (even though this data may be at largely different values of x and Q^2). An example of one such fit is presented in figure 3. The NNLO in the figure stands for Next to Next to Leading Order, which is the precision in α_s at which the perturbative calculations were made (in this case all Feynman diagrams that contain at most two QCD vertices have been taken into account).

A simple extension for the DIS experiments is to measure not only the scattering electron but also some hadrons in the final state (see part b. of figure 4). This is called semi inclusive deep inelastic scattering (SIDIS) and it can provide information regarding the flavor of the struck quark (for example finding a kaon in the final state gives information about the strange quark distribution in the original hadron). However, these measurements have to take into account the probability that a particular struck quark (or gluon) will produce a particular hadron in the final state. These probabilities are called fragmentation functions (FFs) and they are mainly obtained from electron positron scattering. As such, an additional experimental uncertainty has to be taken into account when determining PDFs. A thorough description of SIDIS experiments can be found in [16].

A final experimental technique used in the determination of PDF is scattering between two hadrons (see part c. of figure 4). An added complication here is that both of the participants in the hard scattering process are partons. These experimental results produce information not only of one PDF but a convolution between the PDFs of the participants in the hard scattering process. The particles measured in this case are all from the final state

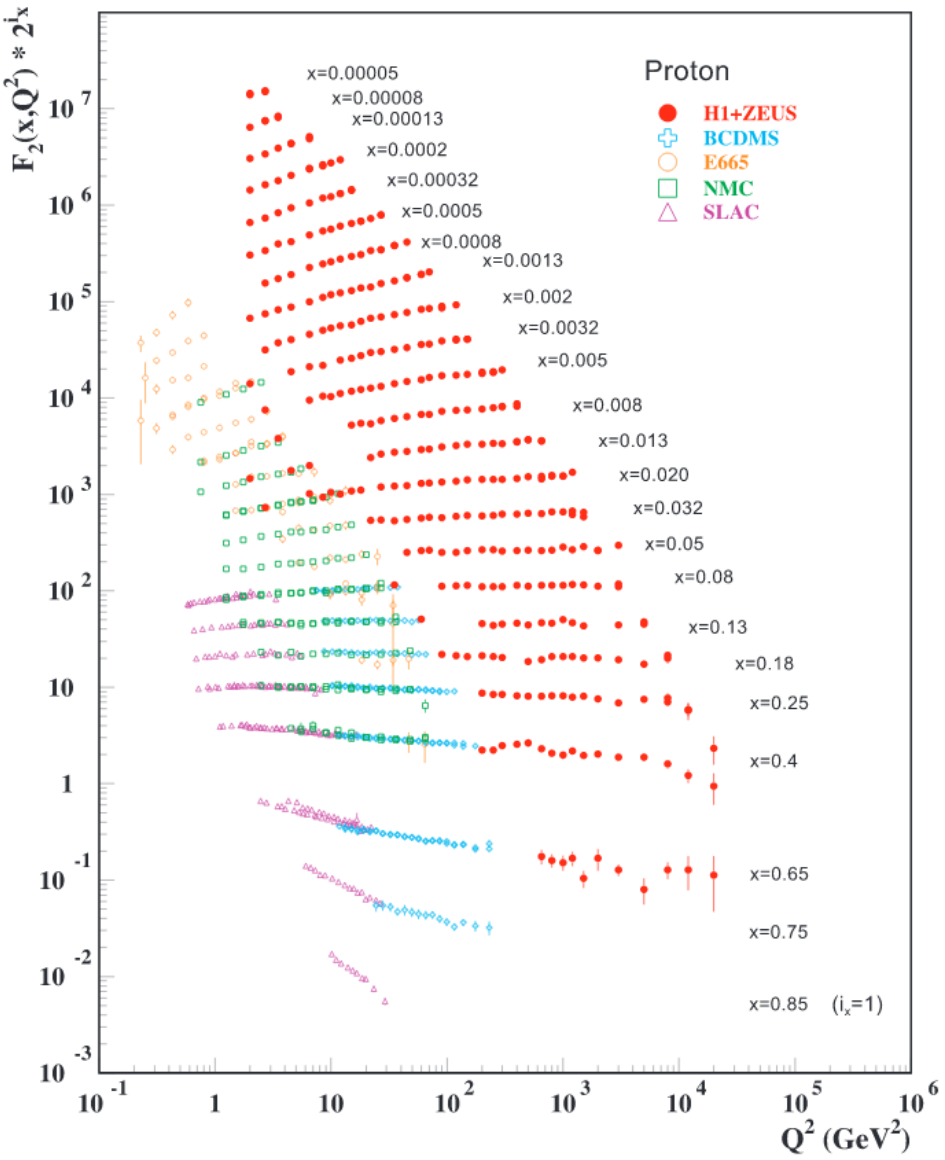

Figure 2: Representative sample of world F_2^p structure function data for the proton. [2].

(bringing with them FFs and their uncertainties). Furthermore, the momentum fraction x and the scale Q^2 are unknown. It is common practice to use

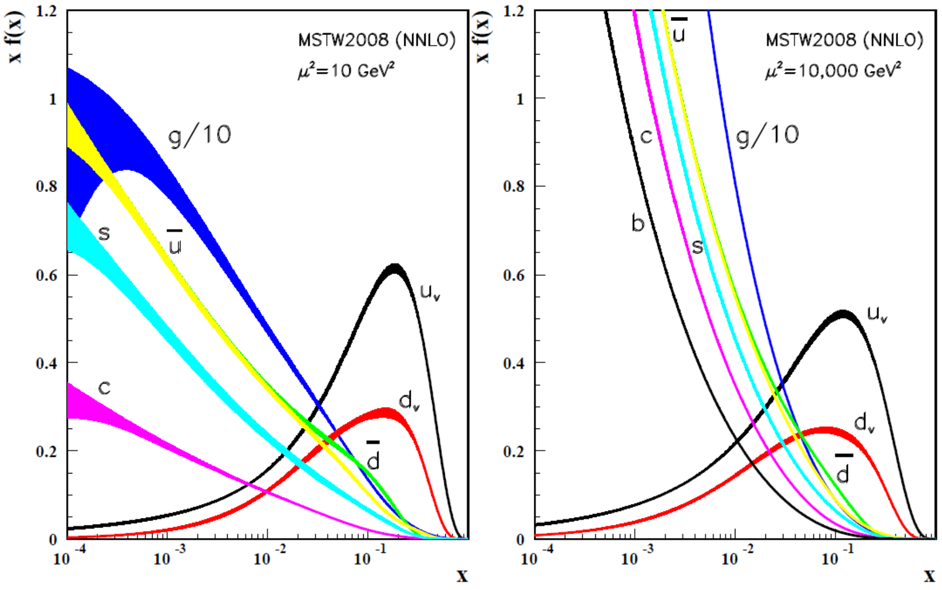

Figure 3: MSTW NNLO PDFs from global fit at Q^2 of 10 GeV (left) and 10000 GeV (right). [2].

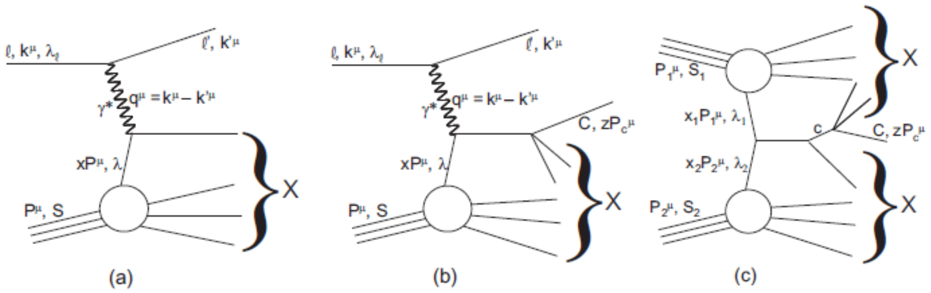

(a) (b) (c)

Figure 4: Three types of experiments used to determine the internal structure of the proton: a) DIS b) semi inclusive DIS c) hadron hadron scattering (figure 1.2 in [1]).

the transverse momentum of the final state measured object (hadron, lepton, photon or jet) as the scale of the interaction. However, one big advantage of the having hadron hadron collisions is the direct coupling of a gluon from one hadron to a quark or gluon from the other hadron, making this type of experiment ideal for measurements of gluon PDFs.

1.2.1 Polarized PDFs

In addition to having a measurements on the momentum distributions of partons inside hadrons, information on the spin contributions of these partons to the particular hadron can be obtained. This can be achieved by simply polarizing the lepton beam and target (most (SI)DIS experiments are fixed target experiments). By summing over the polarization states one can easily obtain the unpolarized PDFs as discussed so far. Besides the unpolarized structure functions (F_1 and F_2) discussed until now, by taking the helicities of the beam and target into account one gets access to polarized structure functions g_1 and g_2. While the unpolarized structure functions are sums of the quark and anti-quark momentum distributions (3), the polarized structure functions g_1 can be written as:

$$g_1 = \frac{1}{2}\sum_q e_q^2 \left(q^+(x) - q^-(x)\right) = \frac{1}{2}\sum_q e_q^2 \Delta q(x). \tag{8}$$

Again, the e_q is the charge of a quark (the sum is over both quarks and anti-quarks). $q^+(x)$ is the number density for a quark/anti-quark that has the spin oriented in the same direction as the spin of the hadron (opposite direction for $q^-(x)$). Equation 8 shows that in fact g_1 is the helicity difference between quark density numbers. The structure function g_2 relates to transverse spin orientation of partons inside a longitudinally polarized nucleon and is beyond the scope of this thesis.

Access to the polarized PDFs generally can be obtained through measurements of asymmetries between cross sections for specific processes when the beam and target polarizations are aligned or anti aligned. By relating these initial beam and target polarizations to the polarizations of the virtual photon being absorbed (in DIS and SIDIS measurements) and the polarization of the parton inside the nucleon that is being investigated one can show that an asymmetry of the type:

$$A(x, Q^2) = \frac{\sigma^+ - \sigma^-}{\sigma^+ + \sigma^-} \tag{9}$$

where σ^- is the measured cross section for events when the parton was antiparallel to the nucleon spin, is in fact ([17]):

$$A(x, Q^2) = \frac{g_1(x, Q^2)}{F_1(x, Q^2)}. \tag{10}$$

With an appropriate parametrization of F_1 (that can be obtained with from a global fit of world unpolarized data), the structure function g_1 can be obtained.

Using this basic experimental technique, the EMC collaboration reported in 1989 [3] that the spin contribution of quarks ($\Delta\Sigma$) to the proton spin was

$$\Delta\Sigma = 0.120 \pm 0.094 \text{ (stat)} \pm 0.138 \text{ (syst)} \tag{11}$$

clearly disagreeing with the current theoretical predictions (see figure 5). At the time, this disagreement was dubbed the *spin crisis*, triggering a flurry of theoretical and experimental work in the field.

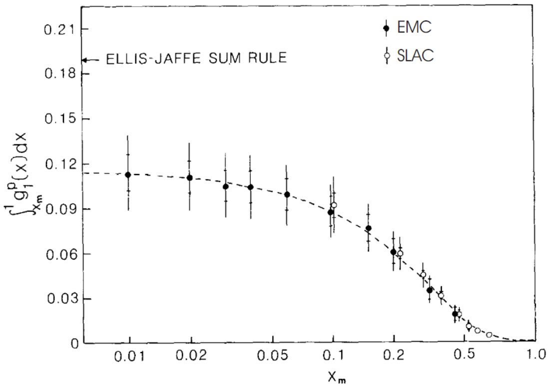

Figure 5: The integral of the g_1 structure function as a function of x ranges from the EMC 1989 experiment ([3]) together with a prediction level needed for the Ellis-Jaffe sum rule.

The theoretical prediction belonged to John Ellis and Robert Jaffe [18] and attempted to decompose the spin of the proton (and neutron) into contributions coming from quarks alone. Since then a series of experiments have confirmed and refined the EMC measurements. The current measurements put the contributions of quarks to the spin of the proton at about 30%. In parallel to the experimental effort, a large amount of theoretical work has been put in to fully decompose the spin of the proton in contributions coming from quarks, gluons, and their respective angular momenta:

$$S^p = \frac{1}{2} = \frac{1}{2}\Delta\Sigma + L_q + \Delta G + L_g \tag{12}$$

where the spin is in units of angular momenta ($\hbar = 1.05457 \times 10^{-34}\ m^2 kg/s$), $\Delta\Sigma$ is the contribution of the spin 1/2 quarks, ΔG is the contribution from gluons and L_q (L_g) are the orbital angular momentum components coming from the quarks(gluons).

A fully gauge invariant way to separate these components has eluded the community for a long time, however recent developments by Hatta and collaborators [19] seem to provide the answer. A nice review of the current theoretical status of spin decomposition can be found in [20].

Similar to global analyses performed for the unpolarized PDFs, the world data from polarized DIS, SIDIS and proton proton scattering has been used to obtain polarized PDFs (see figure 6 for an example together with two different uncertainty calculation methods presented in the hashed and solid bands).

As one would expect, from the extensive measurements done with DIS experiments, the $\sum_f \Delta q + \Delta\bar{q} = \Delta\Sigma$ are quite well constrained, while the rest of the PDFs require more data to decrease the uncertainty in these fits. Comparing the polarized PDFs with their unpolarized counter-parts one can see a large difference in the constraints. Overall, all the polarized PDFs would benefit from additional data, however obtaining data at low x and high Q^2 is experimentally challenging.

1.3 Anti-quark polarized distribution functions

The main focus of this measurement is the investigation of anti-quark polarized parton distribution functions by making use of the parity violating nature of the W production in proton proton scattering. From figure 6, it can be seen that overall the uncertainty in the anti-quark polarization is the dominant component in the quark + anti-quark polarzied PDFs at the top of the figure. The fits presented contain only data from DIS and SIDIS measurements, with the latter being the ones that give any constraints on the anti-quark polarized PDFs. However, as mentioned before, these mea-

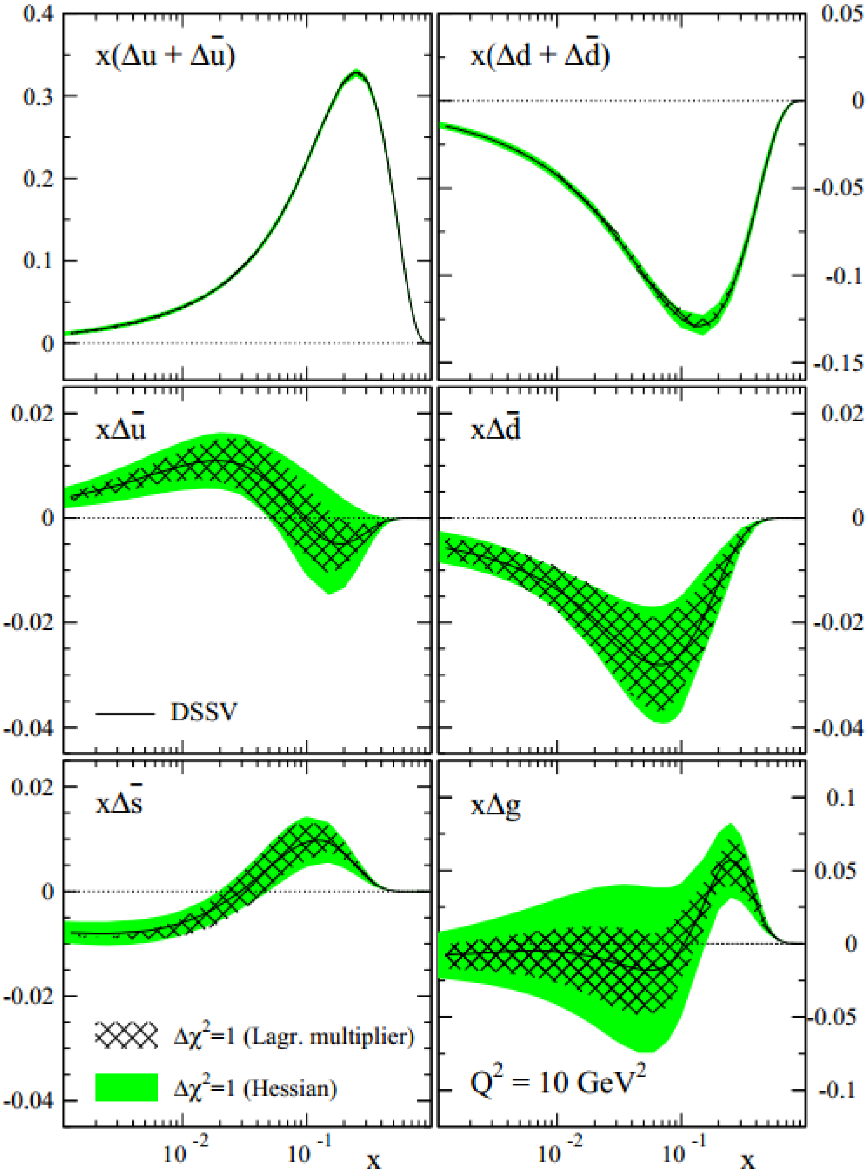

Figure 6: The current world knowledge on polarized PDFs aggregated with the use of the DSSV global analysis [4].

surements have to carry with them the uncertainties from poorly known fragmentation functions[1].

An approach that circumvents the fragmentation problem altogether, is to access the polarized quark and anti-quark distributions through W boson production and subsequent decay into leptons in longitudinally polarized proton proton collisions.

1.3.1 W boson production and decay

Using the factorization theorem, the W boson production cross section in a proton proton collision at leading order can be written as:

$$\sigma(pp \to WX) = \int dx_1 dx_2 \sum_{a,b} q_a(x_1, Q^2)\bar{q}_b(x_2, Q^2)\hat{\sigma}(ab \to W) \tag{13}$$

where x_1 and x_2 are the momentum fractions of quarks a and b, $q_a(x, Q^2)$ is the PDF for the quark of flavor a and $\hat{\sigma}(ab \to W)$ is the cross section for the two quarks to produce a W boson. Because of the large W mass the scale of the process $Q^2 = M_W^2$.

The cross section of the two quarks producing a W boson is:

$$\hat{\sigma}(ab \to W) = 2\pi |V_{ab}|^2 \frac{G_F}{\sqrt{2}} M_W^2 \delta(s - M_W^2) \tag{14}$$

where $|V_{ab}|^2$ is the Cabbibo-Kobayashi-Maskawa (CKM) matrix element for quarks a and b, G_F is the Fermi constant and s is the center of mass energy of the process $s = (p_a + p_b)^2$.

Introducing the rapidity of the W(y_W):

$$y_W = \frac{1}{2} \ln \left(\frac{E_W + P_W}{E_W - P_W} \right) = \frac{1}{2} \ln \left(\frac{x_1}{x_2} \right) \tag{15}$$

together with the previous equations one can obtain a differential cross section for the W$^+$ (at leading order):

$$\begin{aligned} \frac{d\sigma}{dy_W} = K \frac{\sqrt{2}\pi G_F}{3} x_1 x_2 [\cos^2 \theta_C \left(u(x_1)\bar{d}(x_2) + \bar{d}(x_1)u(x_2) \right) + \\ \sin^2 \theta_C \left(u(x_1)\bar{s}(x_2) + \bar{s}(x_1)u(x_2) \right)] \end{aligned} \tag{16}$$

---

[1] Experimental measurements are being done to get a better handle on these uncertainties. For example see the proceedings in [21] or thesis in [22].

where K is a factor that includes first order QCD corrections and θ_C is the Cabbibo angle. A similar equation can be obtained for the W^- differential cross section by taking the hermitian conjugate of equation 16. Note that the second term in equation 16 is suppressed by a factor of approximately 18 due to the Cabbibo angle and can be ignored for a first order approximation.

At PHENIX the decay channel that is used for the W measurement is the lepton channel. A forward measurement is done through the W→ μ decay channel, while the measurement for this thesis is performed in the PHENIX central arm with the W→e channel. The W→ $q\bar{q'}$ decay channels will be buried under a large QCD background (for example pp→jets). Out of all the W decays approximately 10% are through the electron channel studied in this thesis.

Switching the focus from production to decay the following paragraphs will show how the quark and anti-quark polarized PDFs can be accessed from a decay electron asymmetry.

Figure 7: Tracking the momentum and helicity for the W production and subsequent decay [5].

Because of the parity violating nature of the W coupling there are a couple of conclusions that can be drawn when the W was produced in a polarized proton proton collision (like in the case of this thesis). Because of the V − A structure the W will only be formed from a left handed quark (u or d) and right handed anti-quark ($\bar{d}$ or $\bar{u}$). As can be seen in figure 7 the longitudinal momentum of the W will always be in the direction of the quark momentum (as it is expected that the quark will most likely be a valence quark with a higher fractional momentum). Because the W is a spin 1 particle and the quark is left handed the W will also be left handed (meaning that it will be polarized antiparallel to it's momentum). Again because of the parity violating nature of the coupling, the W^+(W^-) will couple in its decay with right handed (left handed) positrons (electrons). Taking the example of the

W^+, because it is left handed, the polarization of the positron necessarily must be opposite to the direction of the W momentum. Moreover, since the positron has to be right handed, it means that it will preferentially decay in the direction opposite to the W^+ momentum. A similar argument can be made for the decay of the electron in the W^- case, where the decay would happen prefferentially in the same direction as the W^- momentum.

This statement can be written mathematically as a differential cross section in terms of the W rapidity and lepton scattering angle θ_l:

$$\left(\frac{d^2\sigma}{dy_W d\cos\theta_l}\right)_{W^+} \sim u(x_1)\bar{d}(x_2)(1-\cos\theta_l)^2 + \bar{d}(x_1)u(x_2)(1+\cos\theta_l)^2 \quad (17)$$

$$\left(\frac{d^2\sigma}{dy_W d\cos\theta_l}\right)_{W^-} \sim d(x_1)\bar{u}(x_2)(1+\cos\theta_l)^2 + \bar{u}(x_1)d(x_2)(1-\cos\theta_l)^2 \quad (18)$$

However, because of the detector configuration, the rapidity of the W cannot be measured since the neutrino momentum cannot be determined. Several studies have been performed by theoretical groups that showed that a direct relation can be made between longitudinal momentum fraction $< x_{1,2} >$ of the partons, and the decay lepton rapidity y_l (for reference see [23] and references within). The study in [23] used the Monte Carlo software CHE (Collisions at High Energy). By accessing the kinematics of all the particles, including the decay electron and the W boson, and taking into account QCD corrections coming from $q\bar{q}' \to Wg$ and $qg \to Wq'$ a high degree of correlation was found between the lepton rapidity and longitudinal momentum fractions of the interacting quarks. An approximate relation can be written as:

$$\langle x_1 \rangle = \frac{M_W}{\sqrt{s}} e^{y_l/2} \text{ and } \langle x_2 \rangle = \frac{M_W}{\sqrt{s}} e^{-y_l/2}. \quad (19)$$

1.3.2 Parity violating single spin asymmetries

By taking into account all the possibilities that a W^+ can be produced from a longitudinally polarized proton proton collision an asymmetry can be obtained that will give access to polarized parton PDFs. Generally two types of asymmetries can be defined:

$$A_L = \frac{\sigma_+ - \sigma_-}{\sigma_+ + \sigma_-} \tag{20}$$

$$A_{LL} = \frac{(\sigma_{++} + \sigma_{--}) - (\sigma_{-+} + \sigma_{+-})}{(\sigma_{++} + \sigma_{--}) + (\sigma_{-+} + \sigma_{+-})} \tag{21}$$

for a single polarized beam a single spin asymmetry (20), and for two polarized beams (21) a double spin asymmetry. [2]The σ_+ indicates the condition of the beam in a collision (in a two polarized beam condition, the polarizations of the second proton are summed over), with the $+$ being positive proton helicity and $-$ being negative proton helicity. In the case of the double spin asymmetry the term σ_{++} represents the polarization state of the two colliding proton bunches. These spin separated cross sections can be written in terms of the efficiencies, number of recorded events (N_{++} for example), and luminosities (L_{++}):

$$A_L = \frac{N_+/(L_+\epsilon_+) - N_-/(L_-\epsilon_-)}{N_+/(L_+\epsilon_+) + N_-/(L_-\epsilon_-)} \tag{22}$$

$$A_{LL} = \frac{(\frac{N_{++}}{L_{++}\epsilon_{++}} + \frac{N_{--}}{L_{--}\epsilon_{--}}) - (\frac{N_{-+}}{L_{-+}\epsilon_{-+}} + \frac{N_{+-}}{L_{+-}\epsilon_{+-}})}{(\frac{N_{++}}{L_{++}\epsilon_{++}} + \frac{N_{--}}{L_{--}\epsilon_{--}}) + (\frac{N_{-+}}{L_{-+}\epsilon_{-+}} + \frac{N_{+-}}{L_{+-}\epsilon_{+-}})} \tag{23}$$

where the term ϵ_{+-} includes the reconstruction, bias and acceptance factors to record an event during a $+\ -$ collision. As discussed in subsection 2.1.1 the alternating spin patterns in the beams allow for these detector efficiencies to be the same for different spin pattern collisions, and can be safely canceled out. The differences in the luminosities for each bunch still need to be taken into account as discussed in 3.1.4. The N_{-+} terms are the number of recorded events and are referred to as spin separated yields in this thesis.

Knowing that the spin separated cross sections and that the overall cross section can be written as $\sigma_0 = \sigma_{++} + \sigma_{-+} + \sigma_{+-} + \sigma_{--}$, one can rewrite the asymmetry equations to obtain the spin separated yields in polarized

---

[2] Since the two asymmetries give similar information and the single spin asymmetry provides higher statistical accuracy only the single spin asymmetry has been calculated in this thesis.

collisions as a function of single (A_L) and double spin (A_{LL}) asymmetries:

$$\begin{aligned}
\sigma_{++} =& \frac{N_{++}}{L_{++}} = \sigma_0(1 + A_L(P_1 + P_2) + A_{LL}P_1P_2) \\
\sigma_{+-} =& \frac{N_{+-}}{L_{+-}} = \sigma_0(1 + A_L(P_1 - P_2) - A_{LL}P_1P_2) \\
\sigma_{-+} =& \frac{N_{-+}}{L_{-+}} = \sigma_0(1 - A_L(P_1 - P_2) - A_{LL}P_1P_2) \\
\sigma_{--} =& \frac{N_{--}}{L_{--}} = \sigma_0(1 - A_L(P_1 + P_2) + A_{LL}P_1P_2)
\end{aligned} \tag{24}$$

All the possibilities to produce a W$^+$ from a polarized proton beam are presented in figure 8. Since for this analysis the single spin asymmetry is the variable of interest, only one of the protons is shown as polarized. The top panel of figure 8 has the quark coming from the polarized proton (case a) and the bottom has the anti-quark (case b). Taking equations 17 and 18 (for the decay direction of the lepton) and following case a), the asymmetry probes the u quark polarized PDF:

$$A_L^{e^+} = \frac{u_+^-(x_1)\bar{d}(x_2)(1-\cos\theta_l)^2 - u_-^-(x_1)\bar{d}(x_2)(1-\cos\theta_l)^2}{u_+^-(x_1)\bar{d}(x_2)(1-\cos\theta_l)^2 + u_-^-(x_1)\bar{d}(x_2)(1-\cos\theta_l)^2} = -\frac{\Delta u(x_1)}{u(x_1)}. \tag{25}$$

Similarly for case b), the probed PDF belongs to the $\bar{d}$:

$$A_L^{e^+} = \frac{\bar{d}_-^+(x_1)u(x_2)(1+\cos\theta_l)^2 - \bar{d}_+^+(x_1)u(x_2)(1+\cos\theta_l)^2}{\bar{d}_-^+(x_1)u(x_2)(1+\cos\theta_l)^2 + \bar{d}_+^+(x_1)u(x_2)(1+\cos\theta_l)^2} = \frac{\Delta\bar{d}(x_1)}{\bar{d}(x_1)}. \tag{26}$$

However, since one cannot know for certain if the quark or anti-quark came from the polarized proton, the asymmetry probes a convolution of the two cases above:

$$A_L^{e^+} = \frac{\Delta\bar{d}(x_1)u(x_2)(1+\cos\theta_l)^2 - \Delta u(x_1)\bar{d}(x_2)(1-\cos\theta_l)^2}{\bar{d}(x_1)u(x_2)(1+\cos\theta_l)^2 + u(x_1)\bar{d}(x_2)(1-\cos\theta_l)^2}. \tag{27}$$

For e$^-$ one just needs to interchange u and d in equation 27 and carefully attend to the lepton decay direction:

$$A_L^{e^-} = \frac{\Delta\bar{u}(x_1)d(x_2)(1-\cos\theta_l)^2 - \Delta d(x_1)\bar{u}(x_2)(1+\cos\theta_l)^2}{\bar{u}(x_1)d(x_2)(1-\cos\theta_l)^2 + d(x_1)\bar{u}(x_2)(1+\cos\theta_l)^2}. \tag{28}$$

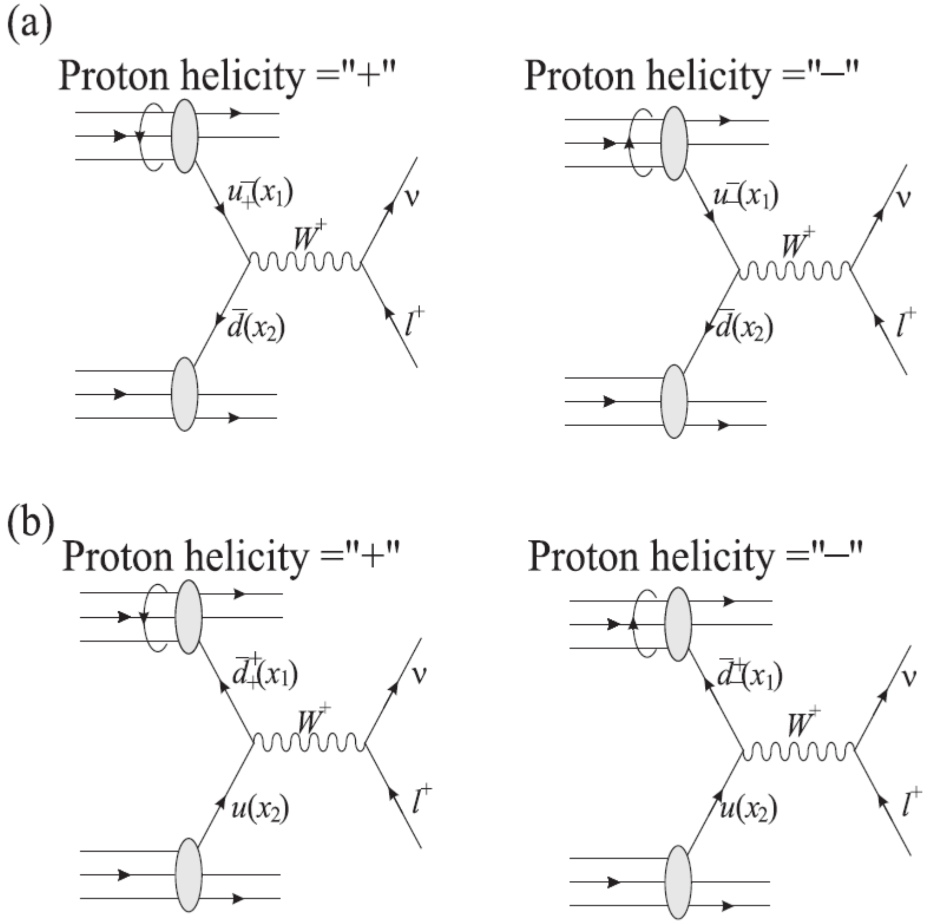

Figure 8: W^+ production in polarized proton proton collisions [6].

1.4 W Jacobian peak

As seen previously, the differential W cross section can be written with respect to the lepton decay angle (θ_l) as:

$$\frac{d\sigma_{W^\pm}}{d\cos\theta_l} \sim (1 \mp \cos\theta_l)^2. \tag{29}$$

Considering that at leading order the transverse momentum of the electron is $p_T = M_W/2\sin\theta_l$, a differential cross section with respect to p_T^2 can be calculated:

$$\begin{aligned}
\frac{d\sigma_{W^\pm}}{dp_T^2} =& \frac{d\cos\theta_l}{dp_T^2}\frac{d\sigma_{W^\pm}}{d\cos\theta_l} \\
=& \frac{1}{2}\frac{4}{M_W^2}\frac{1}{\sqrt{1-4p_T^2/M_W^2}}\frac{d\sigma_{W^\pm}}{d\cos\theta_l} \\
\sim& \frac{2}{M_W^2}\frac{(1\mp\cos\theta_l)^2}{\sqrt{1-4p_T^2/M_W^2}} \\
\sim& \frac{2}{M_W^2}\frac{1+\cos\theta_l^2\mp 2\cos\theta_l}{\sqrt{1-4p_T^2/M_W^2}} \\
\sim& \frac{2}{M_W^2}\left(\frac{1+1+4p_T^2/M_W^2}{\sqrt{1-4p_T^2/M_W^2}}\mp 2\right) \\
\sim& \frac{4}{M_W^2}\frac{1+2p_T^2/M_W^2}{\sqrt{1-4p_T^2/M_W^2}}.
\end{aligned} \tag{30}$$

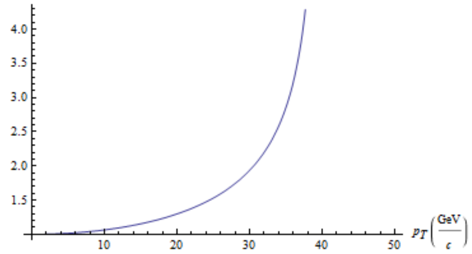

Figure 9: Shape for electrons p_T spectrum coming from W decays.

Equation 30 has a pole at $p_T = M_W/2$ (referred to as a Jacobian peak), which leads the decay electron/positron p_T spectrum to have a specific shape as can be seen in figure 9. The extra constant term was dropped in the last line as it is insignificant compared to the divergence. This divergent behavior of the differential cross section makes sense, as one would expect that the decay of the W boson into two leptons, while at rest, should happen with the vast majority of electrons having transverse momentum of approximately half the W mass. However, in practice this shape will be smeared because of the resolution of the detectors measuring the decay electrons (see figure 60 for an example of a smeared Jacobian).

2 RHIC and PHENIX

2.1 The Relativistic Hadron Ion Collider

The Relativistic Heavy Ion Collider is the largest of several accelerators located in Brookhaven National Laboratory. Its main purpose is to deliver high intensity beam collisions for two experiments: the Pioneering High Energy Nuclear Interactions eXperiment (PHENIX) and the Solenoidal Tracker At RHIC (STAR). It can deliver several species of ion beams: protons, deuterons, copper, gold or uranium. Unlike all the other species of ions, proton beams have an added specificity, in that they are polarized. The data presented in this thesis was obtained from proton proton collisions at $\sqrt{s} =$ 500 and 510 GeV at the RHIC facility.

The process to obtain polarized proton beams starts with the Optically-Pumped Polarized H- Ion Source (OPPIS)[24]. A source of hydrogen atoms provides a 2.8 $\sim$ 3.0 keV beam, which is converted with the use of a optically pumped Rb vapor cell through a Sona transition, into electron-polarized hydrogen atoms. The next step in the process involves using the Sona-transition (hyperfine interaction) to transfer the polarization from the electron to the proton. Using a He gaseous cell the hydrogen atoms are ionized. The final beam from the OPPIS has approximately 87% polarization.

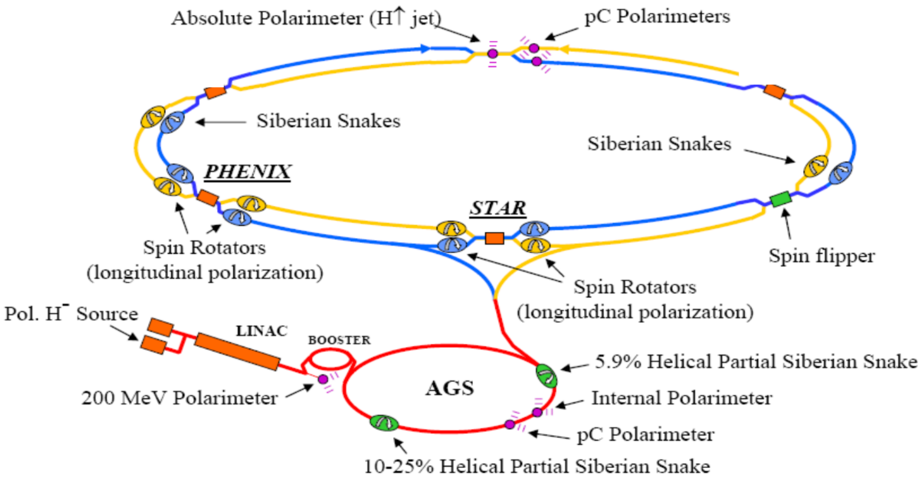

Figure 10: The RHIC accelerator complex and polarimetry locations.

The full RHIC accelerator complex can be seen in figure 10. A detailed description of the accelerator complex and RHIC operations can be found in [25] and references within. For the purposes of this thesis a short description will be given.

The polarized beam from the OPPIS is picked up by the LINAC that delivers it, accelerated to 200MeV, to the Booster. Here the beams are further accelerated to ∼2GeV but with special care to maintain the polarization. Further on, the Alternating Gradient Synchrotron (AGS) gets the 2GeV beam and injects bunches of approximately 10^9 protons into RHIC with ∼25GeV. These bunches are then further accelerated to 250(255 in Run 2012)GeV. The instantaneous luminosity is increased through squeezing (decreasing the transverse cross section of the beam), in the RHIC rings. RHIC has 120 fillable bunches, numbered from 0 to 119. The last 9 bunches in each beam are left empty to enable clean dumping of the beam (these bunches are called the 'abort gap'). Furthermore, a set of 2 bunches are left empty in each beam corresponding to bunches 38-39 for the blue beam and 78-79 for the yellow beam. A set of 109 filled bunches in each beam is called a fill. Normally, fills are maintained in collision for approximately 8 hours before being dumped and the RHIC rings filled again. The beam gets used up as time progresses through the fill with the number of protons in the beams slowly decaying from collisions and from loss as the beam passes through the ring. Furthermore, the polarization has been shown to have a decay during the fill of approximately 2% per hour. The 8 hour value was determined by taking into account the accelerator performance in filling the rings, the number of collisions delivered to the experiments and the polarization decay in a fill. The increase in collisions from getting a new fill is generally greater than the number of collisions lost from the downtime related to filling the rings. At each interaction point a bunch from one beam collides with a bunch from the other beam (called a crossing). For PHENIX the blue beam bunch 0 collides with the yellow beam bunch 0 (called crossing 0 in this analysis), lining up the abort gaps in the two beams and providing the maximum number of collisions. After the ring has been filled and the beam has been stabilized the experiments are allowed to ramp up detectors and take data. PHENIX takes data in ∼1 hour chunks (called runs).

Since these beams are polarized, special care has to be taken in order to maintain the bunch polarization. In both the AGS and RHIC rings, Siberian Snakes[26] are used to avoid spin depolarizing resonances. They are helical magnets that rotate the spin of the bunch vertically by 180°. The depolarizing resonances are small *kicks* from the left(right) that tilt the spin direction of the bunch to the right(left). As it passes through the snake, the vertical flip of the spin transforms this left(right) kick into a right(left) kick, which as the beam is accelerated further in the ring is canceled out by the original left(right) kick. The RHIC ring contains two Siberian Snake so that overall the effect on the spin direction for the experiments is canceled. This setup provides stable vertically polarized beams for the experiments.

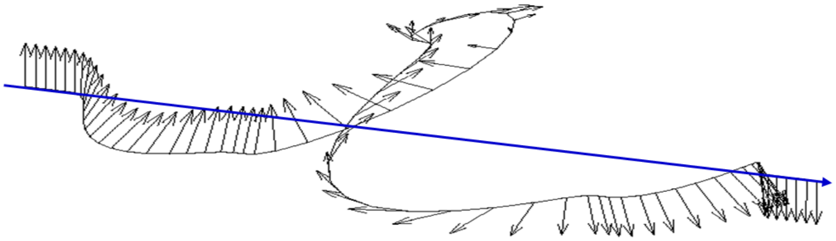

Figure 11: The position coordinates and spin direction of a proton beam as it passes through a Siberian Snake.

The path through one of these snakes can be seen in figure 11. As it can be seen, the snakes affect not only the polarization direction but also the path of the beam. An ideally calibrated snake will reposition the beam at the output at the same (x,y) coordinates as it was received at the input.

Besides the two full snakes each experiment has one half snake before and one half snake after the interaction point called Spin Rotators. Their purpose is to rotate the beam polarization from vertically polarized to longitudinally polarized (the spin direction is same/opposite as the beam momentum) or radially polarized (the spin direction is perpendicular to the beam momentum butt in the horizontal direction). The data presented in this thesis was obtained from longitudinally polarized collisions. The fine tuning of the Spin Rotator magnet currents is performed by the Collider Accelerator Department at RHIC with feedback and spin direction measurements done by each individual experiment. For this thesis, significant work has been done in this respect (please find the detailed method and analysis results in Appendix B).

2.1.1 Polarimetry

In addition to the components described so far, that are needed to develop and maintain polarization, a vital component of the RHIC accelerator complex is the capability to measure and monitor the polarization throughout the acceleration and collision process. To achieve this, RHIC has a dedicated interaction point at 12 o'clock (as can be seen at the top of figure 10). Here, two types of polarimeter measurements are done. The first is a highly accurate, poor statistics measurement with a hydrogen gas jet (HJet - detailed description can be found in [27]). This polarimeter works by injecting a polarized hydrogen gas in the beam pipe where it scatters after collisions with protons in the beam. The remaining gas is then measured upon exit from the beam pipe with a Breit-Rabi polarimeter. The polarized protons from the HJet scatter at nearly perpendicular angles, with respect to the beam axis, where they are measured using silicon detectors. These detectors allow for the measurement of a left-right asymmetry for either the beam or the target, and since the HJet polarization is known from the Breit-Rabi polarimeter, an absolute measurement of the beam polarization can be performed. The main uncertainty for this measurement is due to the formation of molecular hydrogen which can dilute the asymmetry. This uncertainty has been estimated in previous RHIC runs to $< 2\%$.

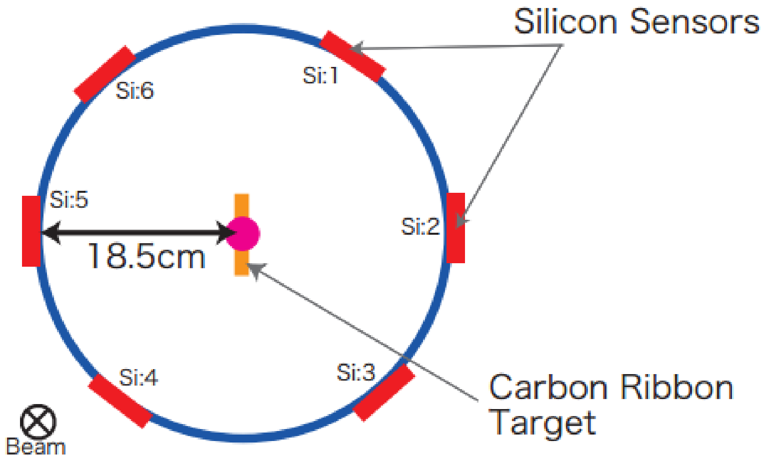

Figure 12: Silicon Detector placement with respect to the target and beam for the proton Carbon polarimeter.

However since the interactions between the target gas and the beam give a low rate (∼ 30 kHz [28]), many fills worth of data would be required to get to a polarization uncertainty of ∼5%. The second type of polarimeter compensates this through a high rate (∼ 20 million events per second) measurement of elastic proton carbon scattering (pC)[29]. This high rate is achieved by scanning the beam with a thin carbon sheet (width of approximately 20nm) multiple times during the fill. The scattered carbon is then detected by another set of silicon strip pixel detectors. The arrangement of the detectors can be seen in figure 12. The detectors in the direction perpendicular to the targets are sufficient to determine the left-right asymmetry, with the other 2 sets used for systematic uncertainty corrections. The asymmetry gives a relative measurement of the beam polarization, which are then scaled by the absolute HJet measurement. Besides the polarization measurement these polarimeters provide a profile of the polarization of the beam in both horizontal and vertical directions by performing vertical and horizontal scans. The profile is then used in determining the final polarization values for each beam and each fill.

In order to minimize systematic uncertainties, CAD provides different polarization patterns for each beam. For 2011 and 2012 the configurations that were used can be seen in figure 13. All of the beam bunches are filled by repeating the pattern in the figure regardless if the bunch is filled or not (even the abort gap and the bunches at 38, 39 positions are taken into account).

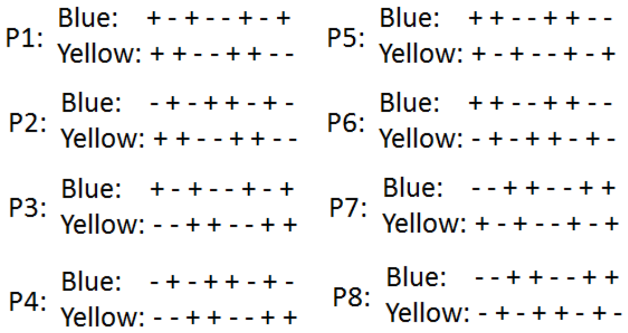

P1: Blue: + - + - - + - +
Yellow: + + - - + + - -

P2: Blue: - + - + + - + -
Yellow: + + - - + + - -

P3: Blue: + - + - - + - +
Yellow: - - + + - - + +

P4: Blue: - + - + + - + -
Yellow: - - + + - - + +

P5: Blue: + + - - + + - -
Yellow: + - + - - + - +

P6: Blue: + + - - + + - -
Yellow: - + - + + - + -

P7: Blue: - - + + - - + +
Yellow: + - + - - + - +

P8: Blue: - - + + - - + +
Yellow: - + - + + - + -

Figure 13: The eight spin patterns available for the blue and yellow beams during the 2011 and 2012 data taking.

As can be seen, the permutations take care of anomalies coming from even/odd crossing (by always having one beam reversing patter after the first 4 crossings), blue/yellow beam differences (by having patterns switched between yellow and blue beams e.g. P1-4 vs P5-8) or positive/negative polarized bunches (by reversing the polarization for crossings e.g. P2 vs P3).

2.1.2 Accelerator performance

The accelerator performance is rated on two criteria: the number of collisions provided to the experiments and the quality of these collisions. The first criterion can be quantified using luminosity which can be generally defined as the number of events divided by the inelastic cross section for the collision species. In 2011 the accelerator achieved an instantaneous luminosity of $\sim 1.6\ 10^{-32}\ \mathrm{cm}^{-2}\mathrm{s}^{-1}$. Directly related to the number of collisions is also the number of ions in the ring (intensity), which for 2011 was $1.8\ 10^{11}$ protons for 109 bunches[30]. Similarly for 2012, the instantaneous luminosity reached $\sim 2.0\ 10^{-32}\ \mathrm{cm}^{-2}\mathrm{s}^{-1}$[31] with a peak intensity of $6.2\ 10^{11}$ protons in the ring for 109 bunches.

For this analysis the detectors used for the measuremnt also need to be taken into account for the calculation of the accelerator performance. A description of the integrated luminosity is given in section 3.1.3. The results for 2011 and 2012 can be seen in table 1.

Secondly, the quality of the beam is primarily determined by the amount of polarization the experiments receive. A detailed description of how the luminosity averaged polarizations were obtained can be found in section 3.1.5.

Overall, the accelerator performance, as far as this analysis is concerned, is determined by the quantity that directly links to the statistical uncertainty of the single spin asymmetry to be measured. This uncertainty is inversely proportional to the polarization delivered (P) and directly proportional to the square root of the integrated luminosity. Thus we can define a figure of merit (FOM) as in equation 31

$$FOM = P^2 \int L dt \tag{31}$$

Table 1 gives this FOM for 2011 and 2012.

Year	Average polarization	Integrated Luminosity [$pb^{-}1$]	FOM [$pb^{-}1$]
2011	0.50	16.0	4.0
2012	0.56	23.7	7.4

Table 1: Table of the achieved FOM in 2011 and 2012.

2.2 The PHENIX Detector

One of the two major detectors at RHIC, PHENIX [32], was designed to have excellent detection capabilities for leptons, photons and hadrons. The data acquisition system is capable to take data in both high multiplicity events during heavy ion collisions and high event rate during proton proton collisions. Special triggers are used for rare events. As can be seen from figure 14 there are two major sections for PHENIX, the central arms (dedicated to measuring electrons, photons or hadrons) and muon arms (dedicated to measuring muons and hadrons). Additionally there are two sets of global detectors at very high pseudorapidity[3] used for luminosity measurements and triggering.

The PHENIX coordinate system is centered at in the middle of the beam pipe with the z axis running parallel to the beam direction and the y coordinate going up into the vertical direction.

All of the detector systems in PHENIX are well described in different papers (see table 2 for specific references). In this thesis only descriptions of the relevant parts for this analysis are presented. This analysis uses the central arm detectors exclusively which will be detailed in the subsections below. A list of the detector systems used can be found in table 2, together with the η and ϕ coverage.

2.2.1 Global detectors

The main global detector in PHENIX, the Beam Beam Counter (BBC), is located at approximately 144 cm from the interaction vertex around the beam pipe. Each BBC consists of 64 quartz crystals that produce Čherenkov radiation which is then picked up by photomultiplier tubes. Its main purpose

---

[3] Pseudorapidity is defined using the angle θ with respect to the beam axis as:

$$\eta = -\ln\left(\tan\,\frac{\theta}{2}\right) \tag{32}$$

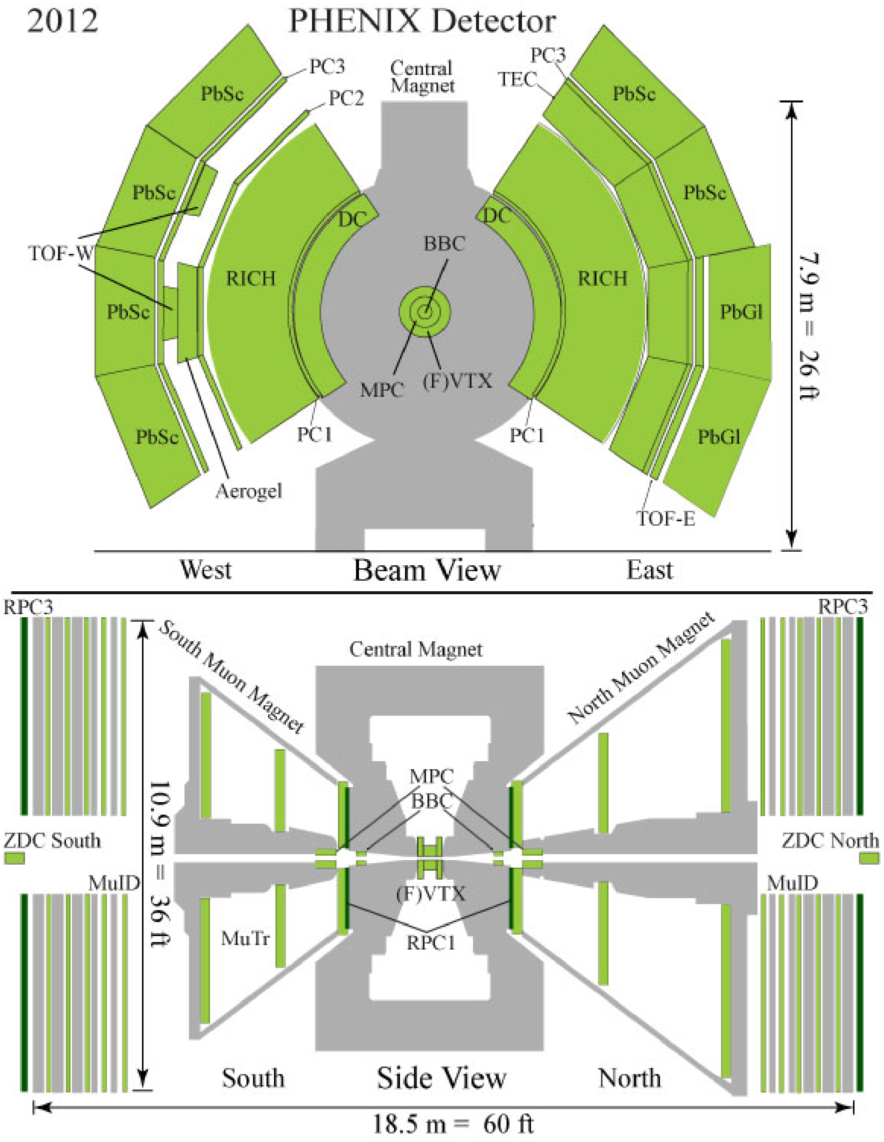

Figure 14: The PHENIX detector configuration during the 2012 data taking period. During the 2011 data taking the Forward Silicon Vertex detector was not yet installed. The top panel shows a cross section in the (x,y) plane of the central arms, while the bottom panel shows a cross section of the muon arms in the (x,z) coordinates.

Detector Name	η	$\Delta\phi$
BBC [33]	$3.1 < \|\eta\| < 3.9$	2π
ZDC [33]	$6 < \|\eta\|$	2π
EMCal [34]	$-0.35 < \eta < 0.35$	2x$\pi/2$
DC/PC [35]	$-0.35 < \eta < 0.35$	2x$\pi/2$

Table 2: Table of the PHENIX detector systems used in this analysis together with references and η and ϕ coverage.

is to determine the interaction time and location along the z axis. The time of the interaction is used by the triggering system to limit the time window in which events are accepted for recording.

The second set of global detectors are the Zero Degree Calorimeters (ZDC). They sit at approximately 18 meters from the interaction point and are behind the DX dipole magnets which separate the blue and yellow beams into their individual beam pipes. They are hadronic calorimeters that measure neutral particles at very high pseudorapidities (forward particles). It is formed out of three Tungsten layers, each with a interaction length λ_I of 1.7. Between the first and second module a Shower Max Detector (SMD) can be found. It consists of 7 vertical and 8 horizontal scintillator strips that give the x and y positions respectively. Since most of the photon showers are fully contained in the first sector the SMD should in principle detect only neutron positions in the ZDC.

For this analysis the BBC weas used for the relative luminosity calculation (as is described in subsection 3.1.4) and the integrated luminosity calculation (as is described in subsection 3.1.3). The ZDC was exclusively used in the Local Polarimetry analysis (as described in appendix B).

2.2.2 Electromagnetic calorimeter (EMCal)

For this analysis, the main detector is the PHENIX EMCal. It determines the energy and hit position of electromagnetic showers from photons and electrons. The EMCal is comprised of six Lead-Scintillator (PbSc) sectors and two Lead-Glass (PbGl) sectors. Each sector spans an area of $\Delta\phi = 22.5^o$. Each of the PbSc sectors has 36×72 towers. Each of these towers has a dimension of $5.5\times5.5\text{cm}^2$ and 66 sampling cells composed of 1.5 mm lead and 4 mm scintillator tiles. This gives each tower 18 radiation lengths [4] (X_0), or 0.85 λ_I. By comparison, the PbGl sectors have a higher granularity with 48×96 towers per sector, each of these towers being $4.0\times4.0cm^2$. It is made up of a homogenous lead glass Čherenkov radiator corresponding to 14.4 X_0 (or 1.1 λ_I). For both types of calorimeter a set of 2×2 towers is summed together and read out through one ASIC chip. The information from 36 ASIC chips [34] (6×6) is read out by one Front-end Electronics Module (FEM). ‘ The energy resolution for the calorimeters was measured with test beam data and was determined to be:

$$\frac{\sigma_E}{E} = 2.1\% \oplus \frac{8.1\%}{\sqrt{E}} \quad \text{for PbSc} \tag{33}$$

$$\frac{\sigma_E}{E} = 0.8\% \oplus \frac{5.9\%}{\sqrt{E}} \quad \text{for PbGl} \tag{34}$$

Each year the calorimeter sectors are carefully calibrated for each individual collision species.

2.2.3 Triggering

The whole PHENIX triggering system is described elsewhere[36], however a short description of the trigger used in this analysis is given below. Because the rareness of the events that are of interest, a trigger was used in the PHENIX Local Level 1 triggering system (LVL1) to record all events that have a high probability to contain a W decay. This trigger is called the ERT4×4 and is defined as a high energy deposit trigger in the EMCal. Using the 2×2 sum energy information from the FEMs the LVL1 system calculates overlapping sums for 2×2 groups (4×4 towers, see figure 15) and compares them to a set threshold. If the sum in any of the 4×4 group of towers is larger than the threshold a signal is sent to the Data Acquisition (DAQ) system to record the event. For the data that is used in this analysis a trigger threshold of ∼5.6 GeV was used. This trigger operated at ∼100 Hz for the 2011 and 2012 data taking periods.

The grouping into 4×4 towers with overlapping sums is required to increase the efficiency of the trigger. In the case where a particle hits the center of an EMCal tower it deposits ∼80% of its energy in that tower and the rest

---

[4] A radiation length is the mean distance traveled by an electron after which it remains with only $1/e$ of its initial energy. The energy loss occurs through interaction with the material through the bremsstrahlung mechanism.

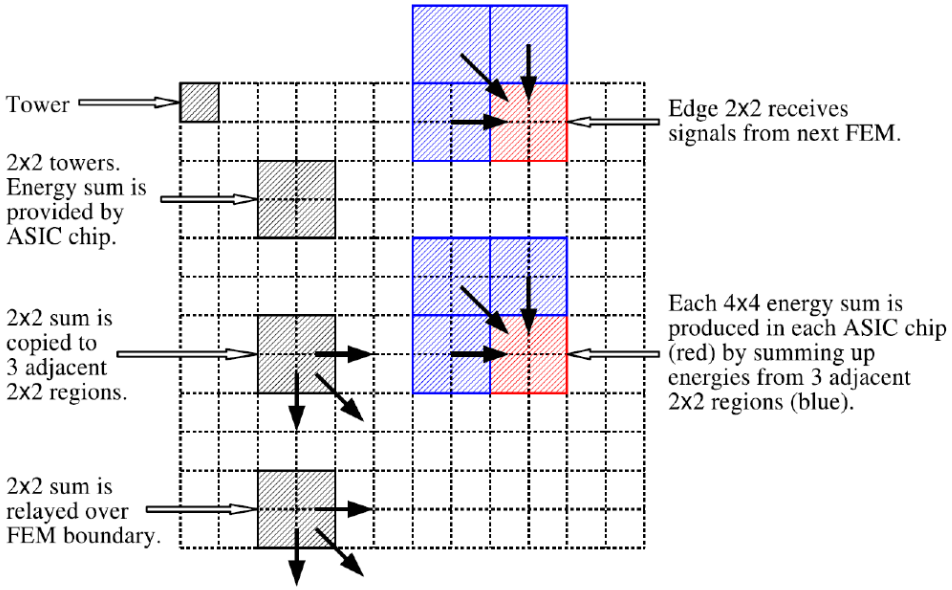

Figure 15: The PHENIX ERT triggering system sketch (figure 2.22 in [7]).

in neighboring towers. However, a particle hitting the corner of a tower deposits only ∼20% of it's energy in that tower. The case where a particle showers at the edge of a 2×2 tower group is taken into account through the use of the overlapping sum. The edges of each sector are summed up with the connecting edges from neighboring sectors. The efficiency for the ERT trigger was studied for this thesis and the results can be seen in section 3.2.3.

A second trigger was used for the calculation of the relative and integrated luminosities. As mentioned before, the BBC is the main global detector for PHENIX. As such, it provides the minimum requirement for the DAQ system to register a collision as an event(MinBias). By having at least one tube fired in both the BBCs, the collision vertex can be determined (through a timing measurement) and a trigger decision can be sent further on to the DAQ. There are three types of triggers based on this minimum requirement: a) a no vertex trigger accepting any coincidence between the BBCs, b) a normal trigger accepting events that have a z vertex only between ± 30 cm from the PHENIX origin and c) a narrow vertex accepting events that have a z vertex only between ± 10 cm from the PHENIX origin.

2.2.4 Tracking

The PHENIX central arm tracking system [35] consists of Drift Chambers (DCs) and Pad Chambers (PCs). They reconstruct charged particle tracks using their bending in the central arm magnetic field.

2.2.4.1 Central Arm Magnets The central arm magnet [37] produces a uniform magnetic field with $\int B \cdot dl$=1.15 Tm parallel to the beam. This field dies off sufficiently at a distance $R >$200 cm for proper DC operations. This is done by using two pairs of concentric copper coils which can be operated independently to provide different field configurations near the interaction point. For the data that is analyzed in this thesis the coils were operated such that the largest possible field strength was available to separate the high momentum electrons. The stability of the magnetic field was monitored (with a set of fixed Hall probes) throughout the data taking process and no changes were seen at the level of 0.1%.

2.2.4.2 Drift Chambers and Pad Chambers The DCs (labeled DC in figure 14 are multi-wire chambers filled with equal mixture of Argon and Ethane, located between 2.02 and 2.46 m radially from beam pipe, separated into two arms. Each arm consists of 20 sectors, each of those covering 4.5° in azimuth. The most important information obtained from the DC is the $r - \phi$ coordinates of a track provided by two sets of wires that run parallel to the beam (called X_1 and X_2 planes). Each wire provides a resolution in $r - \phi$ of $\sim$165μm and an efficiency better than 99%. The resolution for high energy tracks (as are used in this analysis) was determined to be 1.4 mrad (more details can be seen in appendix 3.2.2).

The PCs[38] are a set of multi-wire proportional chambers with cathode readout that provide the z coordinate and thus are essential to the pattern recognition in the PHENIX tracking system. Each cathode is segmented into an array of pixels each with a cell area of 8.4×8.4 mm^2. Out of the three PCs present in PHENIX, this analysis makes use of the set present on the outside of the DCs in the r direction (PC1) (see figure 14). The z position resolution for PC1 was determined to be 1.7 mm.

Since the PHENIX tracking detectors sit outside of the magnetic field as described above, a special technique is required to determine the momentum of tracks. A sketch of this can be seen in figure 16. Because there is only residual magnetic field, tracks in the DC region are nearly straight (full line

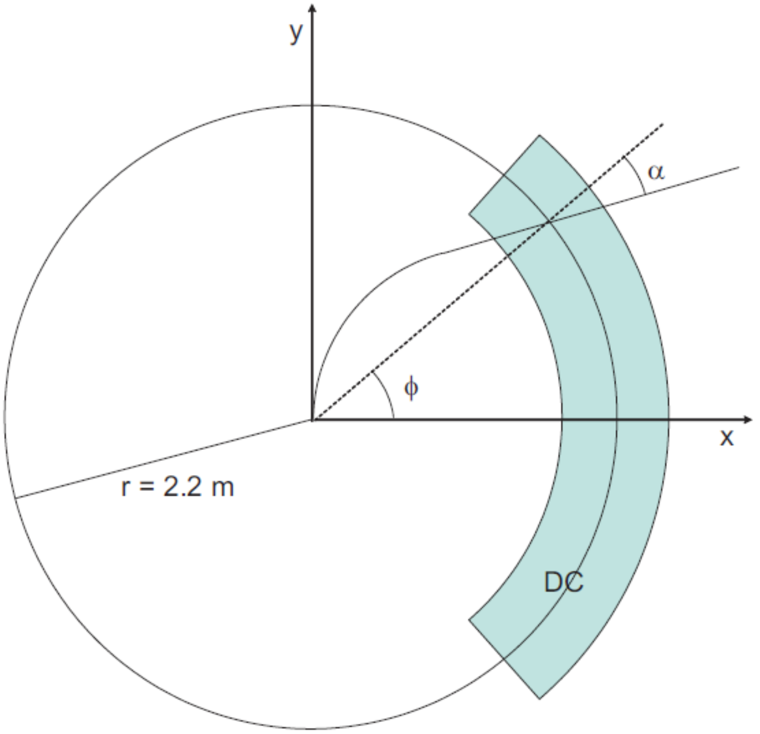

Figure 16: A sketch of the DC α determination technique (figure 3.7 in [1]).

in figure 16). A second line (vector) is determined by connecting the track vector at the mid point of the DC with the vertex point. The angle between these two lines gives a quantity called α which is inversely proportional with momentum (p) as:

$$p_T \sim \frac{92\ [\mathrm{GeV}]}{\alpha\ [\mathrm{mrad}]} \tag{35}$$

With the z information provided by the PC1, the full momentum of the track can be determined.

3 Data Analysis

As described in the introduction section 1.3.2, the quantity of interest in this analysis is the single spin asymmetry from electron/positron candidates, that can be written as:

$$A_L = \frac{1}{P_B} \frac{\frac{N^+}{L^+} - \frac{N^-}{L^-}}{\frac{N^+}{L^+} + \frac{N^-}{L^-}}, \tag{36}$$

for each beam in RHIC. P_B is the polarization of that particular beam, $N^{\pm}$ is the yield when the helicity of that beam was positive or negative respectively, and $L^{\pm}$ is a luminosity normalization factor for those respective helicity configurations. Because of the rarity of the events that are being looked at (out of $\sim 3.7 \cdot 10^7$ ERT triggered collisions for the whole 2012 run, one spin pattern gets at most 30 signal events), it is unfeasible to calculate an asymmetry as a function for each fill in RHIC. What is done in this analysis is to use the whole data set and collect events for each spin pattern and use equation 36 to calculate an asymmetry for the overall yields.

This chapter is structured as follows: a general overview of the collected data together with the detector configurations for 2011 and 2012 is followed by a characterization of the polarization conditions in the two runs. Further on a detailed description of detector quality assurance cross checks performed and data reduction is given. Although not required for this result, a general integrated luminosity calculation is presented. Next, the relative luminosity factors present in equation 36 are determined. Finally the analysis cuts, background estimation and asymmetry calculation are presented.

3.1 2011 and 2012 runs

3.1.1 Beam energies

In 2011, the beam energy was identical to the first measurement in 2009 of the electron/positron asymmetry from W decays with $\sqrt{s} = 500$ GeV [39]. However starting with 2012 the energy was increased by 5 GeV per beam in an effort to avoid depolarizing resonances and maintain a high level of beam polarization for a longer period of time during a fill. The increase to $\sqrt{s} = 510$ GeV has a minimal effect on the the asymmetry results. This lead to the possibility to combine the data from 2011 and 2012 into on single measurement.

3.1.2 PHENIX detector configuration

Because of the flexibility to open up the PHENIX detector after every run, improvements and upgrades are done almost every year to be able to extend the measurement capability of the detector. Between the measurement in 2009 and the data collected in 2011 and 2012 the Hadron Blind Detector (HBD) was taken out of PHENIX and replaced with a Silicon Vertex Detector (VTX). The VTX covers the whole acceptance in front of the central arms, where this measurement was done. The new material together with the support and electronics resulted in an increase in the radiation length by a factor of 3 (from X/X_0 =3.3% to X/X_0 =13.5%). This new detector configuration led to a series of studies and development of different analysis cuts to tackle the extensive background from conversions (see 3.3.2.7 for more details). The VTX detector was commissioned in 2011 and as such the information that it could have provided did not span the whole data set.

In 2012, the forward vertex tracker (FVTX) was added to PHENIX. It covers an area between $20 < |z| < 39$ cm. For this analysis events are accepted that are in $|z| < 30$ cm from the nominal PHENIX origin, so the added material from the FVTX provided even further increase in conversion background. However, the analysis procedure determined for 2011 was deemed robust enough to tackle this increase. The FVTX was designed to detect muon tracks that can then be closely measured with the PHENIX muon arms. Together with the VTX it can determine the collision vertex, however, the calibrations were not performed in time for this analysis.

3.1.3 Integrated Luminosity

Generally, luminosity can be defined as:

$$L = \frac{events}{\sigma_{inelastic}^{pp \to X} \cdot \epsilon_{eff}} \tag{37}$$

where $\sigma_{inelastic}^{pp \to X}$ is the inelastic cross section in proton proton collisions, and ϵ_{eff} is the efficiency with which a particular detector will see a signal in any given collision. Because the quantity of interest is an asymmetry (as can be seen from equation 36), the inelastic cross section and efficiency cancel out and just the number of events seen by the detector (in this case the EMCal) for each spin pattern is important.

Since the inelastic cross section for the EMCal is unknown, for this analysis, luminosity was calculated using the BBC as a proxy:

$$L = \frac{events}{\sigma_{BBC}} \cdot rejection \tag{38}$$

Where the different components are:

- σ_{BBC} is the BBC minimum bias cross-section (taken to be 32.5 mb^{-1} as was determined in the 2009 vernier scan)
- *events* is the number of events that triggered the ERT 4×4 trigger and had a BBC vertex that was within ± 30 cm
- *rejection* is calculated by dividing the number of BBC MinBias triggered events (within $z_{BBC} < 30$cm) in a PHENIX run by the number of BBC MinBias events that also had the ERT trigger fired

All the runs that were available in the official PHENIX data production were used. The results for 2011 and 2012 were 16.7 pb^{-1} and 23.7 pb^{-1}, respectively.

3.1.4 Relative luminosity

Since each bunch in RHIC is filled independently, one cannot assume that the luminosity delivered by each pattern is the same. This means that filling bunches with different spin directions can result in a bias being introduced in the final result. For this reason a measurement of the relative difference between the spin dependent luminosities ($L^{\pm}$) is done (called relative luminosity). The relative luminosity has been calculated using a scaler from the BBC which fires when there is a collision that satisfies $|z_{BBC}| < 30$ cm for the entire 2011/2012 data taking period, resulting in an average over the whole run (for example in 2012 each spin pattern had $\sim 3 \cdot 10^9$ MinBias events in the $|z_{BBC}| < 30$ region).

Run	BY:+ +	BY:− +	BY:+ −	BY:− −
2011	1.000	1.001	0.990	0.985
2012	1.000	1.013	0.996	0.996

Table 3: Table with relative luminosity values from 2011 and 2012.

Table 3 shows the counts from the scaler as a function of different spin patterns: the first column is for the Blue beam having positive helicity +

and Yellow beam having positive helicity +, the second is for Blue − Yellow + and so on. Since the asymmetry measurement requires only the relative luminosity difference between different spin patterns, the number of MinBias triggers for the ++ pattern was used as a reference and each pattern's MinBias trigger count was divided by it. The results are then used in the asymmetry calculation detailed in 3.3.5. The systematic uncertainty from the relative luminosity calculation has been determined and is much smaller than the statistical uncertainty in this measurement.

3.1.5 Beam polarziation

As mentioned above, the asymmetry is calculated for the whole data set at once. Since the polarization values of each beam fluctuate with each new fill in RHIC a method was employed to determine the average of the blue/yellow beam polarization. This is achieved by using a luminosity weighted procedure. Counting the 4×4 ERT triggered events (N_{run}), in a 30 cm vertex cut, the average polarization for each beam can be calculated as:

$$\bar{P} = \frac{\sum_{runs} P_{run} \cdot N_{run}}{\sum_{runs} N_{run}} \tag{39}$$

Each RHIC fill (and by extension all the PHENIX runs from that fill), has an officially released value for beam polarization given by the RHIC polarimetry group[40] and a related uncertainty. The uncertainty is given by the usual uncertainty propagation:

$$\Delta\bar{P} = \sqrt{\left(\sum_{runs} \frac{\partial \bar{P}}{\partial P_{run}} \Delta P_{run}\right)^2 + \sum_{runs} \left(\frac{\partial \bar{P}}{\partial N_{run}} \Delta N_{run}\right)^2} \tag{40}$$

$$\Delta\bar{P} = \frac{1}{\sum_i N_i} \cdot \sqrt{\sum_i (N_i \Delta P_i)^2 + \sum_i \left(\frac{\sum_j N_j \cdot (P_i - P_j)}{\sum_j N_j} \Delta N_i\right)^2} \tag{41}$$

The uncertainty was obtained by taking the maximum of the uncertainties determined through regular uncertainty propagation for each beam. The mean values and uncertainties used in the analysis are presented in table 4.

	Run 2011	Run 2012
Blue Beam	0.509 ± 0.056	0.550 ± 0.046
Yellow Beam	0.500 ± 0.056	0.570 ± 0.046

Table 4: Table of luminosity weighted polarization value used in this analysis.

3.2 Data reduction and quality assurance

There are several reasons why a PHENIX run should not be analyzed. The most important case is when one of the detectors involved in the measurements was not on, had a problem with the voltages provided or data collection electronics. This would make that particular detector provide corrupt information and either not detect particles that actually hit it or creates fake signals in the data. A second reason would be that the trigger used to collect the events was not functioning as designed and gave too many/few triggers per minimum bias event. This will increase the likelihood of having background or fake events in the final result, and although cross checks and cuts are performed on the events in the analysis it is undesirable to keep these runs. Finally, since all of the information will eventually be used to calculate an asymmetry the spin pattern information that exists for each crossing has to be accurate. It can happen that the information received from the Collider-Accelerator Department is inaccurate or that it gets corrupted during processing it into the PHENIX databases.

These three cases are going to be discussed in the following pages with plots and comments on runs that were taken out of the analysis.

3.2.1 EMCal quality assurance

The EMCal contains 24768 towers that, as in any detector, can be dead (it returns no energy deposits all the time), hot (it returns energy deposits even though there was no hit in the actual detector) or cannot be calibrated due to lack of statistics. A tower is noisy (or hot) due to noise in the electronics collecting the signal from the towers. Towers like these lead to fake signals or bad reconstructions of cluster energies in the EMCal software. To clean up the data the towers that fall in any of these three categories are excluded from the reconstruction and analysis.

3.2.1.1 Calibration Before the hits in the EMCal are passed through the clustering algorithm to determine the energy deposited by each particle, a calibration for each tower has to be performed. The first step of the calibration is to determine the hit frequency for each tower and outliers are marked as either hot or dead. These towers are not calibrated and not used in the clustering procedure by adding them to a warnmap. Simply put, the rest of the calibration is an iterative procedure, in which at each step a large amount of runs is analyzed to determine a neutral pion invariant mass peak. The peak for an uncalibrated tower will be away from the nominal π^0 mass and so for each tower a scale factor is determined to correct it. These scale factors are then taken into account in next pass over for the clustering algorithm. This procedure is iterated until the scale factors converge to 1. Even through the iterative procedure some towers cannot be calibrated. For the 2011 calibration 167 (0.67% of the total towers) towers were left uncalibrated, while in 2012 that number was only 105(0.42% of the total towers). In both runs 1840 towers that are on the edge of the EMCal sectors were considered as uncalibrated and excluded in the clustering algorithm.

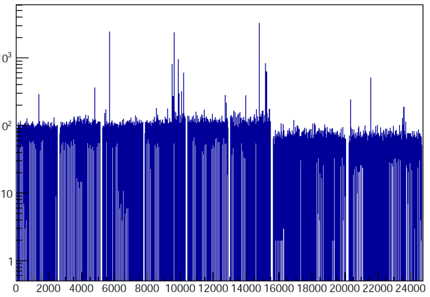

Figure 17: Number of hits as a function of tower ID number for 2011 data.

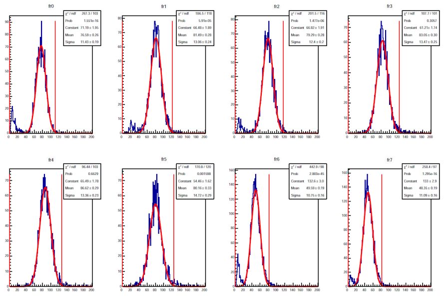

Figure 18: Histogram of number of channels as a function of fire rate for 2011 data.

3.2.1.2 Analysis Warnmap All the clusters that are found to be dead, hot or uncalibrated during the initial calibration procedure are not used in the clustering algorithm. Additionally, an independent warnmap for clusters that have energies larger than 8 GeV is determined before performing the analysis. Figures 17, 18, 19, 20, show the number of hits per channel and the frequency of a particular number of hits in each sector of the EMCal.

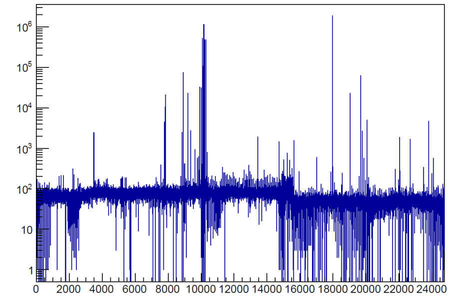

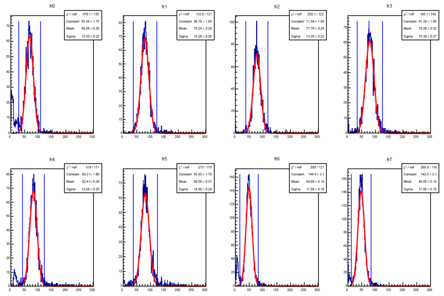

Figure 19: Number of hits as a function of tower ID number for 2012 data.

Figure 20: Number of channels as a function of fire rate for 2012 data.

For the towers with an ID number higher than 15552, the number of hits per tower is smaller due to the higher segmentation of the PbGl EMCal sectors.

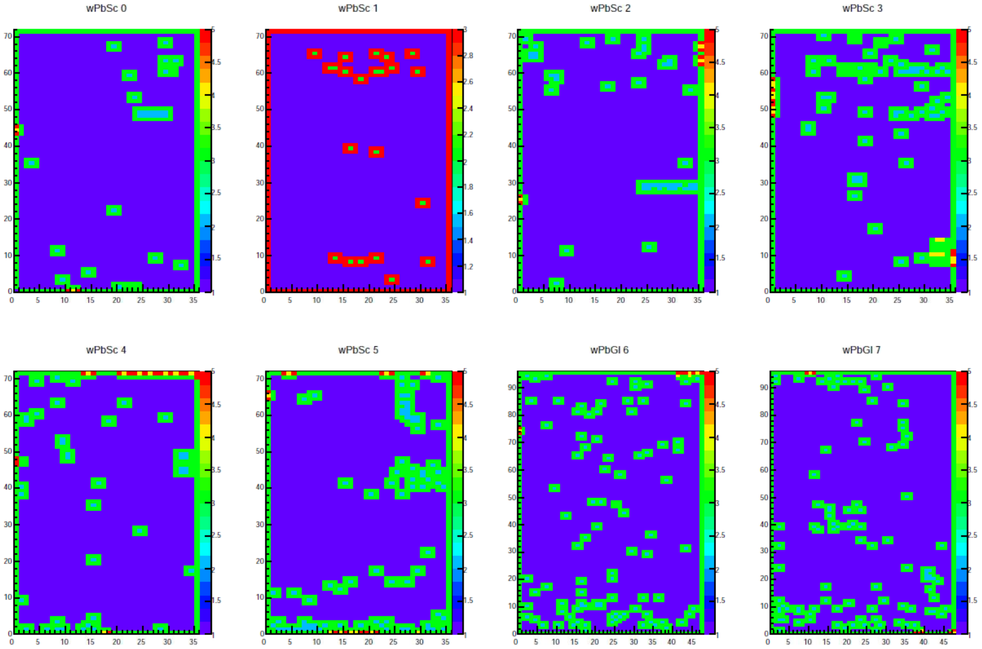

Figure 21: Final warn channel map for the EMCal in 2011. Blue represents good towers, all other colors represent towers that were excluded from the analysis.

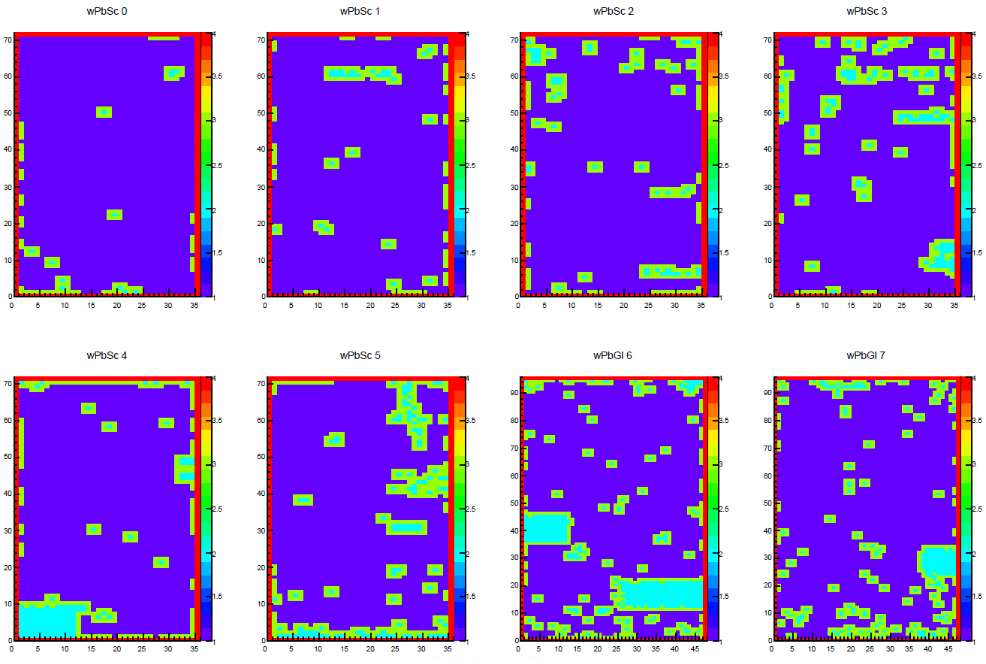

Figure 22: Final warn channel map for the EMCal in 2012. Blue represents good towers, all other colors represent towers that were excluded from the analysis.

The hit frequency distributions were fit with a Gaussian distribution and it was decided that a channel that had a value more 3σ above the mean of the distribution would be deemed hot.

The 8 towers around a hot channel, that was deemed hot, are also masked off for the analysis. This is because clusters centered in towers that neighbor hot towers will have a bias in the reconstructed energy. Additionally, since the calibration of towers on the edge of each EMCal sector cannot be well performed, there is an one channel edge that is excluded from the analysis in each sector.

Figures 21 and 22 show the result of the masking on the EMCal. Colors different from blue (value 1 on the z axis) represent excluded towers (each other color represents some problem with the tower).

3.2.1.3 Excluded runs Another test that was performed on the data was to count the number of clusters in the EMCal for each run. This number

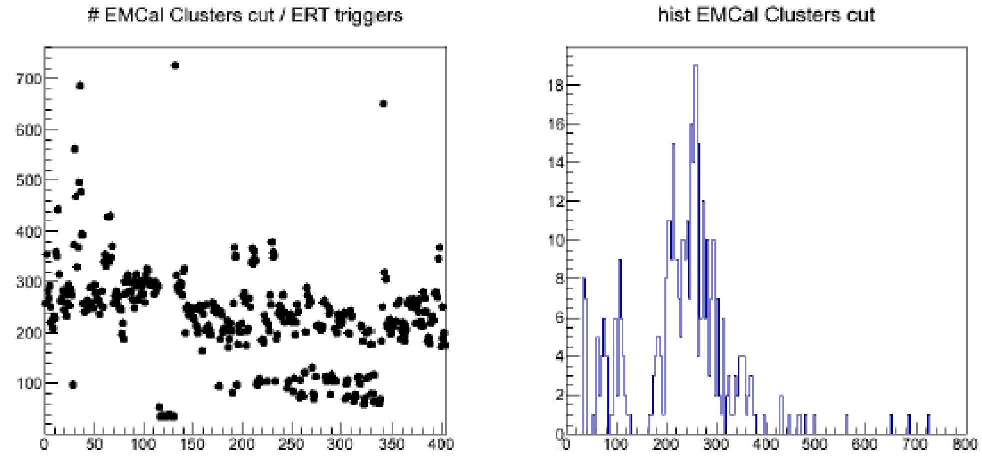

Figure 23: Left Panel: reconstructed EMC clusters (with basic cuts) divided by ERT trigger count as a function of run index, before run exclusion, for 2011 data. Right panel, histogram of the left panel.

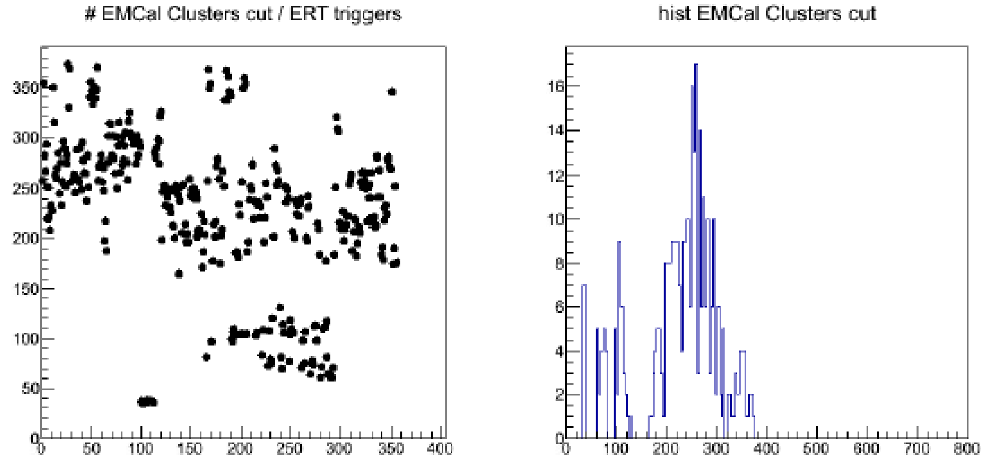

Figure 24: Left Panel: reconstructed EMC clusters (with basic cuts) divided by ERT trigger count as a function of run index, after run exclusion, for 2011 data. Right panel, histogram of the left panel.

alone will fluctuate depending on the integrated luminosity accumulated in the run, but if divided by the 4×4 ERT trigger, it will give an indication regarding the state of the detector. If the number of clusters is lower than the average it may be an indication that either the EMCal did not register enough clusters (maybe because of some problems with the detector or electronics) or that the trigger was firing too often (the second possibility is checked by looking at the number of reconstructed tracks in the DC, see below). In this analysis the runs where the EMCal reports higher number of clusters than the average are of particular interest. In these cases, it is more likely that clusters will be associated with tracks from the DC/PC system and end up in the final spectrum as background.

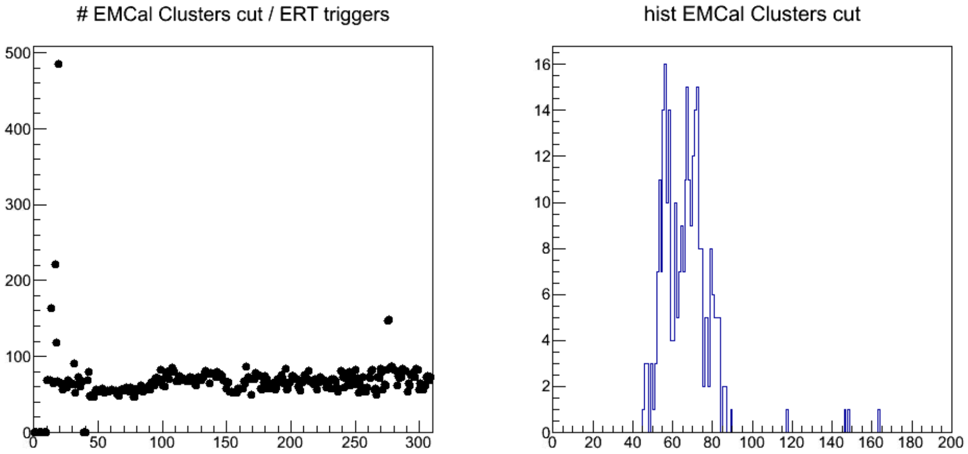

Figure 25: Left Panel: reconstructed EMC clusters (with basic cuts) divided by ERT trigger count as a function of run index, before run exclusion, for 2012 data. Right panel: histogram of the left panel.

Figures 23 and 25 show the number of reconstructed clusters with basic cuts ($|z_{rec}| < 30$, DC matching) divided by the number of ERT triggers in a run as a function of run index (what number in the data set this particular chunk of data is) before the quality assurance had been performed. Runs that showed a significant difference from the mean of the distribution were investigated on a case by case basis. The hardware status was checked through monitoring plots PHENIX keeps for each run. Furthermore, the data taking logbook entries related to that run number were checked for any anomalies. Most of the runs that had higher than normal cluster rates were found to

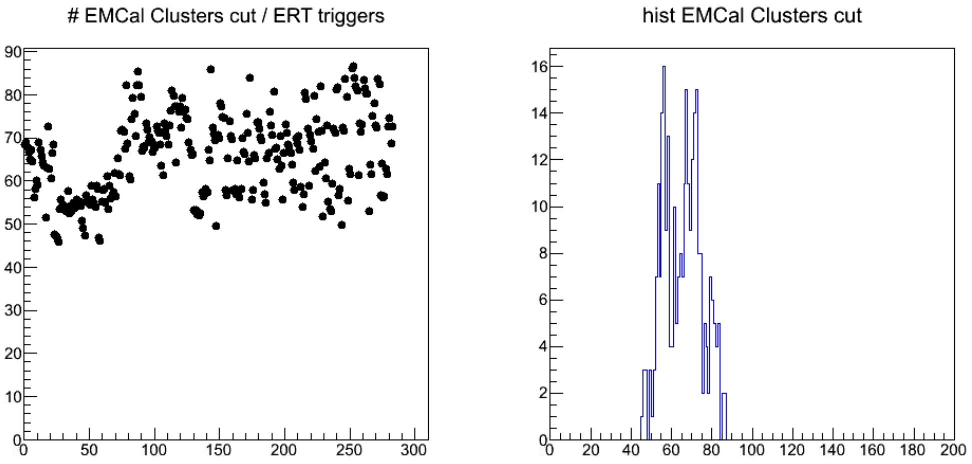

Figure 26: Left Panel: reconstructed EMC clusters (with basic cuts) divided by ERT trigger count as a function of run index, after run exclusion, for 2012 data. Right panel: histogram of the left panel.

have electronics or hardware problems leading to them being dropped from the analysis. Figures 24 and 26 show the number of clusters divided by number of ERT triggers after runs were excluded. In figure 25 it can be seen that in the 2012 data there were run periods (index <15 and around index 40) that did not have any EMC cluster information. Through the investigation, it was discovered that the central arm detectors were not included in the data taking stream for those runs. These runs were excluded as well as can be seen in figure 26.

3.2.2 DC/PC quality assurance

The quality assurance for the DC/PC system is done with magnetic field off runs. These runs are performed regularly (about once every week) during normal data taking operations, or after one of the PHENIX arms is moved for maintenance. Data is collected with the whole detector and calibrations are performed using the straight tracks (i.e. tracks that are straight from the collisions point) that go through the DC/PC tracking system.

The calibration consists in determining the offset that the DC/PC system has with respect to the collision point (a detailed explanation of the beam offset calibration procedure can be found in appendix C). These offsets are then used in the PHENIX track reconstruction software as the collision point for track fitting.

3.2.2.1 Pair tracks The regions close to the anode wires in the DC are prone to creating *ghost tracks* because of left-right ambiguity within ± 2mm distance from the anode wires. Tracks that are reconstructed in these regions should be excluded. To properly identify these regions one can look at the number of hits as a function of ϕ in pair tracks. Pair tracks are defined as two tracks that have opposite sign of α and are within 0.01 in ϕ. The results of this analysis can be see in figures 27 and 28 for the two DC arms.

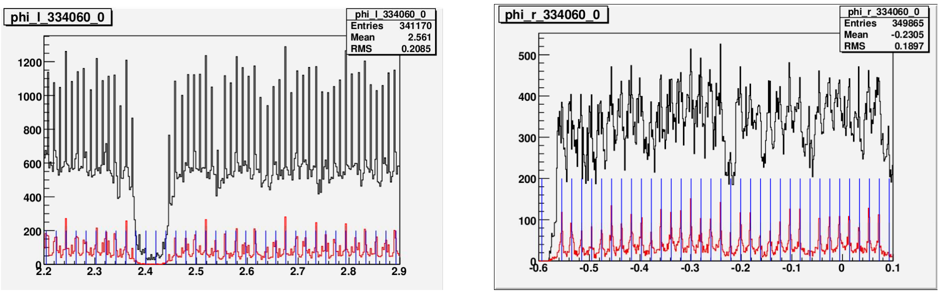

Figure 27: EAST arm

Figure 28: WEST arm.

Figure 29: All DC reconstructed tracks (black) and pair tracks(red) as a function of ϕ. The blue lines are calculated anode wire positions from equations 42 and 43.

The blue lines in the figures 27 and 28 are the anode wire positions calculated using the equations determined in previous PHENIX analyses:

$$\text{East: DC board \#} = \frac{3.725 - \phi_{DC} + 0.00895cos(\phi_{DC} + 0.716)}{0.0196} \tag{42}$$

$$\text{West: DC board \#} = \frac{0.570 + \phi_{DC} - 0.0174cos(\phi_{DC} + 0.973)}{0.0198} \tag{43}$$

Using the relations in the equations 42 and 43 a variable was created for each track by taking the decimal values for each track's ϕ coordinate (dcboard). A cut was implemented to remove these problem regions. The anode wire regions can be found in the regions : $0.05 <$ dcboard < 0.90 for the west arm, $0.1 <$ dcboard < 0.95 for the east arm.

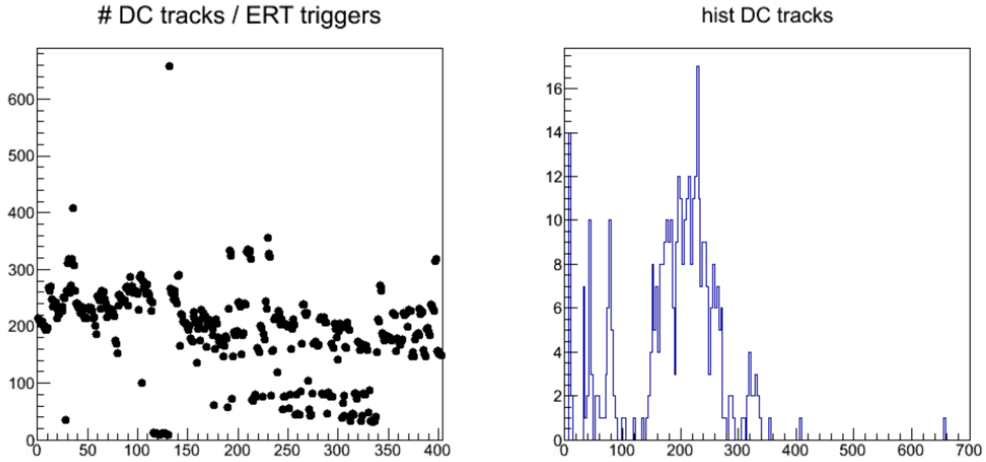

Figure 30: Left Panel: reconstructed DC tracks divided by ERT trigger count as a function of run index, before run exclusion, for 2011 data. Right panel: histogram of the left panel.

3.2.2.2 Excluded runs Similarly to what was described in the case of the EMCal, the DC/PC tracking system can be checked by looking at the number of reconstructed tracks divided by the 4×4 ERT triggers for each run. Figures 30 and 32 show the number of clusters divided by the ERT triggers in a run, before run exclusion for the 2011 and 2012 data respectively. Figures 31 and 33 show the situation after run exclusion. Note that the runs that

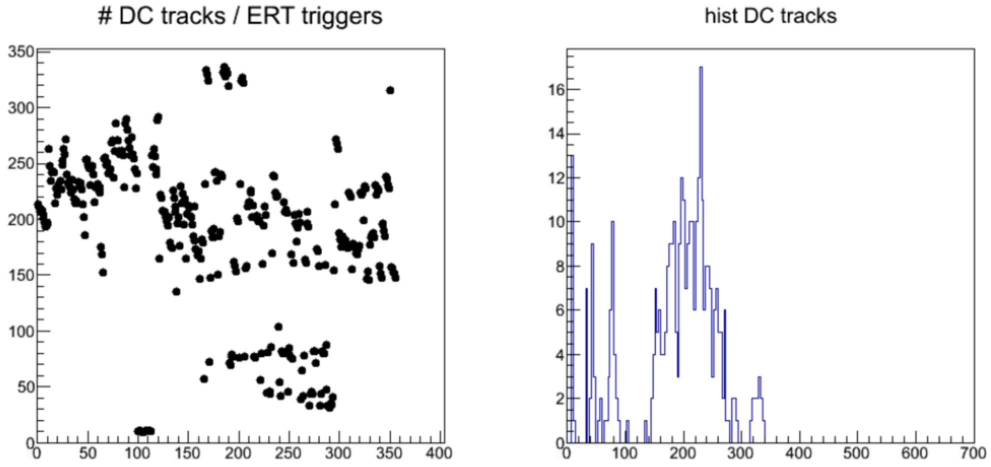

Figure 31: Left Panel: reconstructed DC tracks divided by ERT trigger count as a function of run index, after run exclusion, for 2011 data. Right panel: histogram of the left panel.

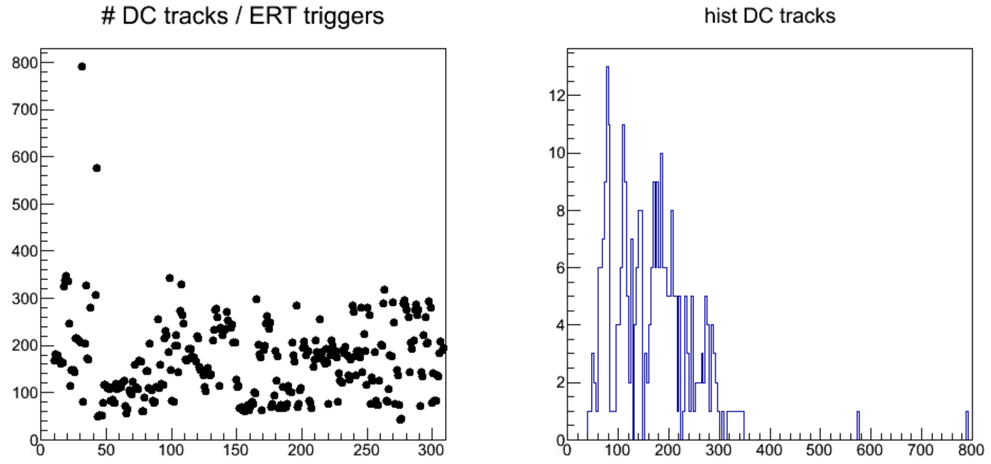

Figure 32: Left Panel: reconstructed DC tracks divided by ERT trigger count as a function of run index, before run exclusion, for 2012 data. Right panel: histogram of the left panel.

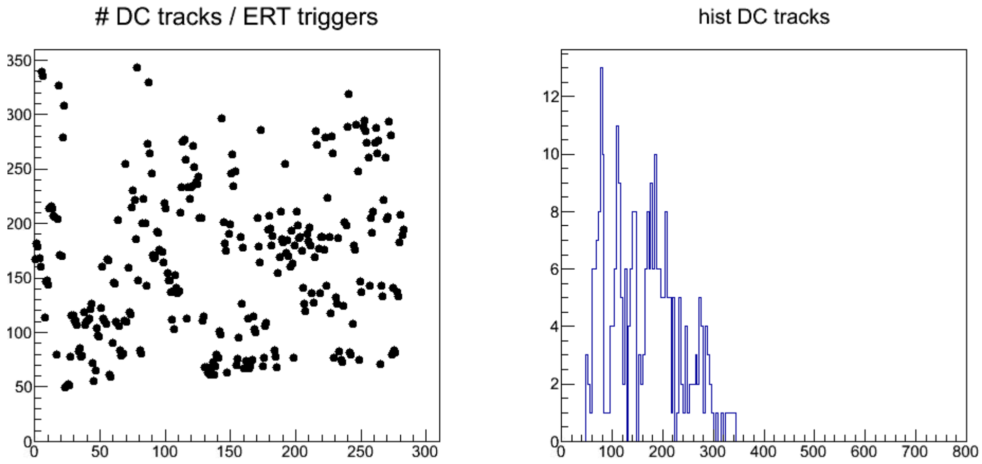

Figure 33: Left Panel: reconstructed DC tracks divided by ERT trigger count as a function of run index, after run exclusion, for 2012 data. Right panel: histogram of the left panel.

cause most concern (the ones that seem to provide large number of tracks than the average) are removed through the quality assurance process.

A total of 27 were removed from a total of 404 runs for the 2011 data set. For the 2012 data, the EMCal and DC quality assurance removed 30 runs out of a total of 309.

3.2.3 Trigger quality assurance

The trigger performance was check for consistency throughout the data taking period by analyzing the trigger rate (number of events per second) from the PHENIX database. However, in order to be fully confident in the data, the trigger efficiency was also calculated.

The method used for this trigger efficiency calculation was developed by Kensuke Okada[41] for a previous PHENIX analysis. It provides a way to use triggered data to get the efficiency in an unbiased way. A simple example is an away side study: since PHENIX has two arms, events with triggers in one arm can be identified and all the clusters in the opposite arm can be analyzed and considered as not containing any bias.

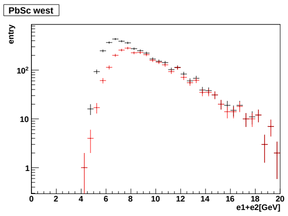

Figure 34: PbSc west 2011 data

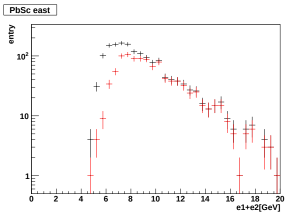

Figure 35: PbSc east 2011 data

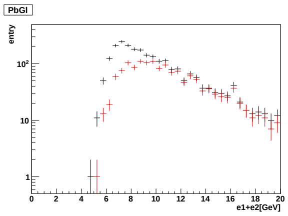

Figure 36: PbGl 2011 data

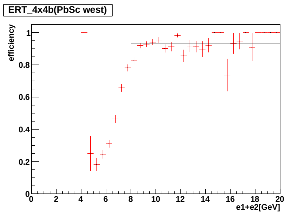

Figure 37: PbSc west, ERT4×4

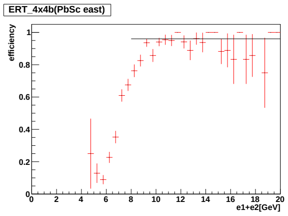

Figure 38: PbSc east

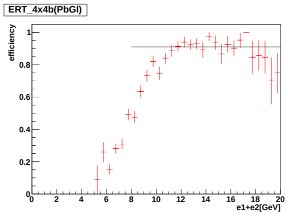

Figure 39: PbGl

By identifying the location of clusters that fired the 4×4 trigger an analysis can be performed on the clusters that were at least two sectors away from the trigger sector. By using standard photon cuts developed in PHENIX an invariant mass was calculated for photons that were 25 cm or less apart. This last requirement was used to ensure that the two photons would fall into the same 4×4 trigger tile. Neutral pions were identified by selecting on

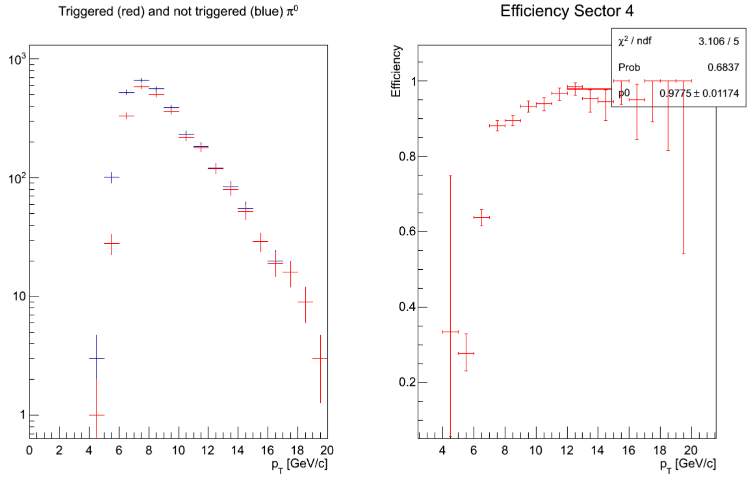

Figure 40: Left: Spectrum for π^0s with an ERT4×4 trigger (red) and all π^0s in each sector for EMCal Sector 4. Right: Efficiency calculated as the fraction of π^0s with an ERT4×4 trigger to the total number of π^0s for sector 4.

the invariant mass of the two photons to be within 0.03 GeV of 0.137 GeV[5]. The efficiency was obtained by dividing the number of π^0s that had fired the trigger by the total number of π^0s.

From the 2011 data statistics were not sufficient when this study was completed (during the data taking period) so the trigger efficiency was calculated for PbSc (east and west) and PbGl separately (as can be seen in figures 34 through 39). In 2012 the study was done with the full dataset so a sector by sector analysis was completed (as can be seen in figure 40 for one sector). The rest of the sectors show similar results and the figures can be found in appendix E The results show that the trigger is fully efficient by 10 GeV for both PbSc and PbGl.

3.2.4 Spin information quality assurance

The spin pattern information of the two beams is collected by PHENIX and stored in the spin database. Before the analysis retrieves this information

---

[5] The difference from the actual π^0 mass is a standard procedure in PHENIX to take care of smearing from the detector.

checks need to be performed to ensure this data is correct. Both the data from 2011 and 2012 have been through a series of cross checks consisting of:

- Confirm the data exists in the database for a particular run number.
- Polarization values and patterns are consistent with the officially released values from C-AD and the RHIC polarimetry group.
- The spin patterns are consistent for both beams throughout a fill. Once RHIC has been filled, under normal running conditions, there is no change in the spin pattern for all the runs taken by PHENIX in that fill.

The spin database quality assurance removed 23 runs from the 2011 data, leading to a total of 50 runs ($\sim$12% of the total number of runs). Similarly for the 2012 dataset 20 runs had corrupted information in the spin database leading to a total of 50 removed runs ($\sim$16% of the runs).

3.3 Measurement of single spin asymmetries

As described in subsection 2.2 on the PHENIX detector, the lack of 2π coverage in ϕ leads to some different choices regarding the identification of W decays compared to other hadron detectors. Generally, a missing energy method is employed, whereas the transverse momentum of all particles is measured and events are selected where there is a significant imbalance coming from the escaped neutrino. However, for this analysis the method that lead to the original W boson discovery is used. By measuring the transverse momentum (p_T) of the charged leptons (electron/positron) in the PHENIX central arms, an excess over the QCD background should appear peaked at $\sim$40 GeV (half of the W mass). After several cuts designed to remove as much background as possible the region between 30 and 50 GeV is used for an asymmetry calculation. The background fraction in this region is estimated through several methods and used as a dilution to get the final asymmetry.

The following subsections contain details regarding each step of this procedure. However, first a closer look at what kind of events could mimic signal but are in fact background is in order.

3.3.1 Backgrounds

As specified before the signal needed for this measurement is constituted of electrons and positrons ($e^{\pm}$) coming from W decays. These decays produce a specific p_T spectrum with a Jacobian peak shape (see figure 42 or 41 for the shape of the green curve). Most of the signal is situated at p_T between 30 and 50 GeV (which is designated as the signal region).

As specified before the signal needed for this measurement is constituted of electrons and positrons ($e^{\pm}$) coming from W decays. These decays produce a specific p_T spectrum with a Jacobian peak shape (see figure 42 or 41 for the shape of the green curve). Most of the signal is situated at p_T between 30 and 50 GeV (which is designated as the signal region).

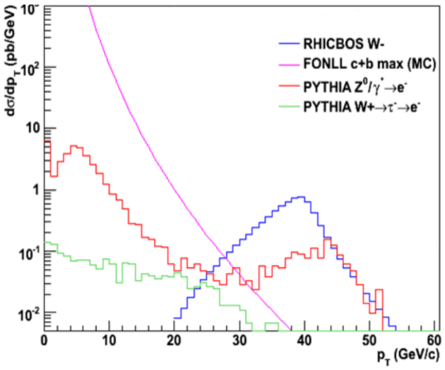

Figure 41: Signal and background contributions to electron p_T spectrum.

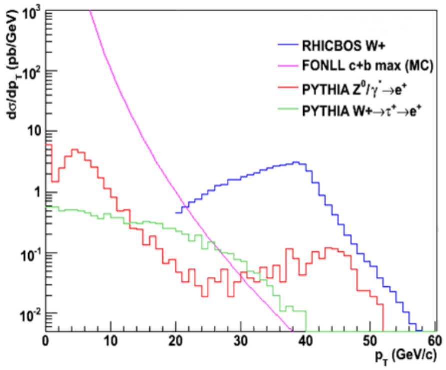

Figure 42: Signal and background contributions to positron p_T spectrum.

However there are other processes that contribute to electrons/positrons yield (background):

- Photon conversions: these conversions, produced specifically at the end of the magnetic field will have a tracking signature that looks like a high momentum track because of the lack of bending in the magnetic field. Furthermore, the increase in tracks in the DC/PC will increase the likelihood that a cluster in the EMCal will be able to be matched.

- Cosmic rays: this type of background affects primarily the EMCal where large energy deposits will trigger the data acquisition and be saved as a possible W event. Combining this with the possibility to match this cluster with a track in the DC/PC, gives another sources of possible background.

- Accidental matching between the EMCal and DC/PC: besides the two cases discussed above, there is always the possibility that one cluster in the EMCal that fired the trigger will find a match in the DC/PC system and pass some of the cuts.
- Z $\rightarrow e^{+} + e^{-}$ decays: The first of the irreducible background and the one with the largest contribution in the signal region, the Z decay electron/positron cannot be distinguished from W decay electrons/positrons.
- Drell-Yan processes: in this process, similar to what process that is being investigated, two quarks annihilate, but instead of producing a W they produce a virtual photon that will then decay into a pair of leptons.
- W $\rightarrow \tau + X \rightarrow e + X'$ decays: since this process produces a high energetic electron as the final product, it cannot be distinguished from the actual signal.
- heavy quark decays: similar to the previous three cases the electrons that come from these types of decays are indistinguishable, with the current experimental setup, from actual W events.

The last four items are irreducible background and cannot be identified because of limited ϕ coverage and inability to tag τs or heavy quarks. To increase the signal to background ratio in the 30 to 50 GeV region several cuts are applied to the data. Figures 41 and 42 show the most important background contributions from simulation (obtained from [42]). It can be seen that the largest contribution to in the 30 to 50 GeV region (where the signal is maximized) is from Z/γ decays, with a smaller contribution from c/b decays.

Unlike the signal that is being investigated the background is not expected to show any measureable asymmetry.

3.3.2 Analysis cuts

A list of the cuts used in this analysis are presented below:

- Offline cluster cut of 8 GeV and warnmap exclusion

- DC matching
- reconstructed z vertex < ±30 cm
- Removal of events with tracks near DC anode wires
- Removal of events with tracks that have α_{DC} within ± 0.001 rad
- Relative isolation variable smaller than 10%

As explained in the triggering section(2.2.3) because of the rarity of the process that is being investigated the data had a special trigger as a high energy deposit in the EMCal. The data in this thesis is a subset of events that had this particular trigger. The following paragraphs will give a detailed description of the cuts above that remove background events.

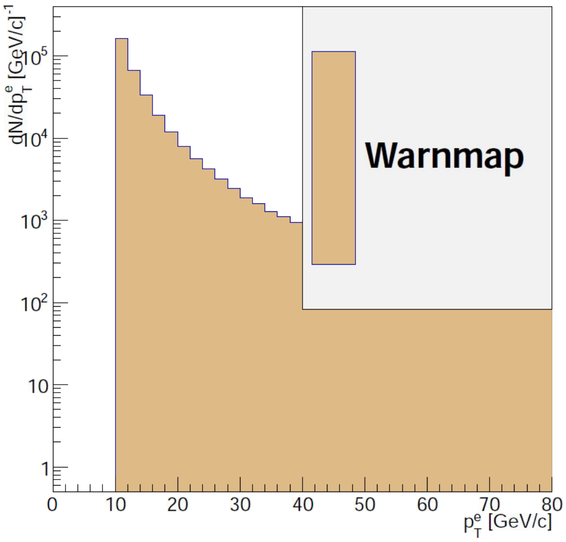

Figure 43: p_T spectrum for electron candidates after applying the 8GeV cluster requirement and warnmap for 2012 data.

3.3.2.1 EMCal cluster selection

The analysis is performed by looping over all the clusters in an event that had a 4×4 ERT trigger associated with it. As a first cut, clusters that have an energy than is lower that 8 GeV are removed. Although the desired data is predominantly in the 30 to 50 GeV region, the region between 10 and 20 GeV is used as a background control region. Furthermore, clusters that are centered on towers that are in the warnmap (as described in 3.2.1) are also dropped as they have a high probability to contain bad information. The rest of the clusters are considered signal candidates and go through the rest of the analysis. Figure 43 shows the p_T spectrum for electron candidates after applying these requirements.

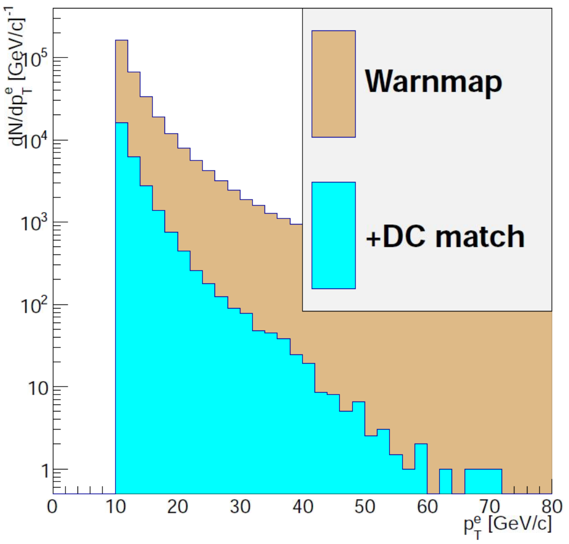

Figure 44: p_T spectrum for electron candidates after matching to the DC (in light blue) for 2012 data.

3.3.2.2 DC matching For each candidate cluster, a match is attempted with tracks reconstructed from the DC/PC. The tracks have to have enough points in the both regions of the DC (both X_1 and X_2) and a matching hit in PC1. Furthermore, only tracks that have at least a 3 GeV momentum are considered[6]. If there are any tracks that meet the requirements, the one with highest momentum that has a projection on the EMCal that is smaller than 0.02 radians in ϕ is selected for the match. Figure 44 shows the effect on the p_T spectrum for electron candidates with the additional DC matching requirement.

---

[6] Although the DC/PC has excellent momentum resolution for tracks below 1 GeV tracks, this resolution degrades quickly with higher momentum tracks. The 3 GeV momentum requirement is there to remove low momentum tracks from consideration and decrease accidental matches.

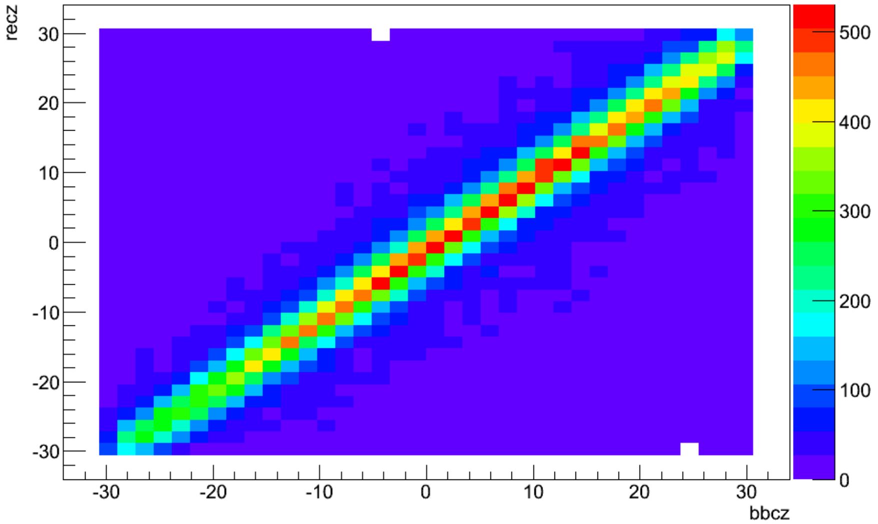

Figure 45: The reconstructed z vertex from the EMCal/DC extrapolation vs the BBC z vertex for 2011 data.

3.3.2.3 Reconstructed Z Vertex Although, as described in the detector section, the BBC usually provides a vertex position for most analyses in PHENIX, the resolution it provided was not good enough for this case. The drop in resolution for the BBC is directly related to multiple collisions, when the BBC just provides an average z vertex between all the vertexes happening in that beam crossing. Instead, the position information from the EMCal (each cluster has x,y,z information) and from the DC/PC associated track (DC provides x,y and PC the z coordinate) is used to extrapolate back to the collision point providing a reconstructed z vertex.

As a cross check the z_{rec} from the EMCal/DC system is plotted against the z_{BBC} obtained from the BBC. Figure 45 shows a very good correlation between the two variables.

The equation used for this reconstruction is:

$$z_{rec} = z_{PC} - \frac{z_{PC} - z_{EMCal}}{r_{DC} - \sqrt{x^2_{EMCal} + y^2_{EMCal}}} \cdot r_{DC} \tag{44}$$

where $r_{DC} = 220$ cm is the radius at the midpoint of the DC (the radius at which the $(\phi,\ \theta)$ are returned).

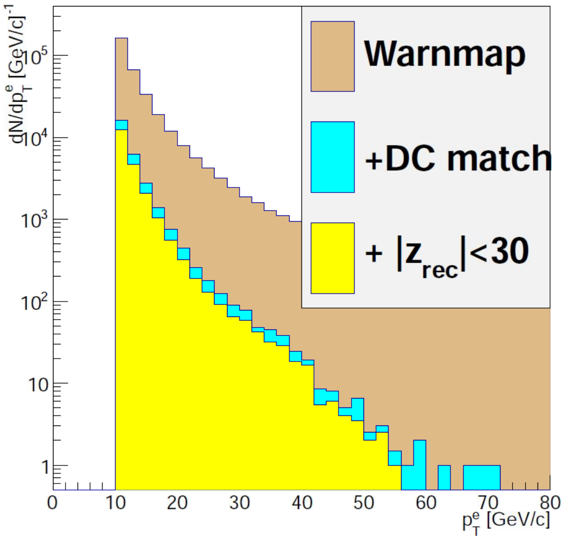

Figure 46: p_T spectrum for electron candidates in a ±30 cm reconstructed z vertex (in light yellow) for 2012 data.

In order to ensure proper coverage for both the EMCal and DC/PC a reconstructed z vertex of $|z_{rec}| < 30$ cm was imposed on candidates (approximately 70% of the collisions happen withing ±30 cm). Figure 46 shows the effect on the p_T spectrum for electron candidates with the additional z_{rec} requirement.

3.3.2.4 DC anode wires As explained in section 3.2.2 the region around DC anode wires are not reliable for track reconstruction as it has a high chance of creating *ghost* tracks. To remove these areas a cut was developed and implemented in the analysis. Figure 47 shows the effect on the p_T spectrum for electron candidates with the anode wires removed on top of the previous cuts.

3.3.2.5 DC resolution and charge disambiguation The sign of the charge for the electron candidates is established by the DC through the measurement of α_{DC}. The resolution for this variable was determined by determining the width of the α_{DC} distribution for field off runs after the correction from the beam shift has been applied. Figure 48 shows the α_{DC} distribution

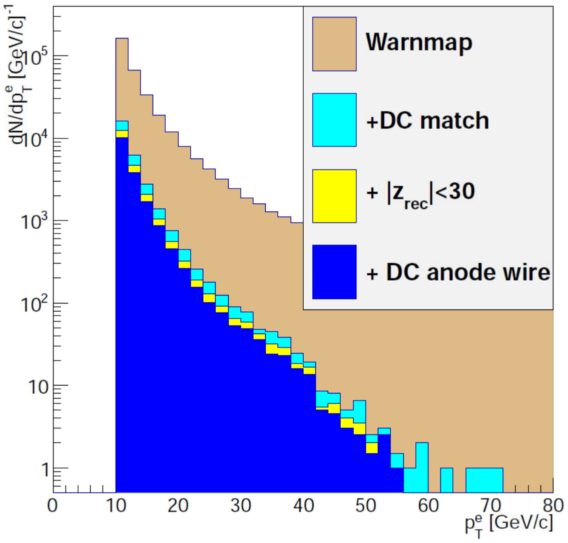

Figure 47: p_T spectrum for electron candidates with anode wire regions removed (in dark blue) for 2012 data.

for one field off run. In order to remove small momentum tracks (that degrade the resolution due to multiple scattering), for this study only tracks that have a match in the EMCal are used. The histogram was fit with a double Gaussian (one for the actual tracks and one for the remaining low energy tracks) and the third parameter (p2) gives the resolution: 1.4 mrad.

With the α_{DC} resolution on hand and knowing that the relation between α_{DC} and momentum is approximately 92 [GeV]$/\alpha \approx p$ an estimate of the charge contamination can be made. Figure 49 shows this estimation. Two Gaussian distributions are plotted taking into consideration the correct fraction of W$^+$ to W$^-$ (a factor of 4 was chosen). The mean of the distribution is $\alpha_{DC} = 2.3$ mrad (which corresponds to a 40 GeV track) and the width of the distribution is the resolution determined above. Because of the resolution of the DC there will be tracks that have a misidentified charge. By removing regions around 0 mrad, this charge misidentification can be minimized. Figure 49 shows 3 scenarios for small α_{DC} removal with the percentages of remaining tracks with the correct charge after small $\alpha_D C$ removal.

By cutting out $abs(\alpha) < 0.001$ rad, there is a contamination of 0.3% for

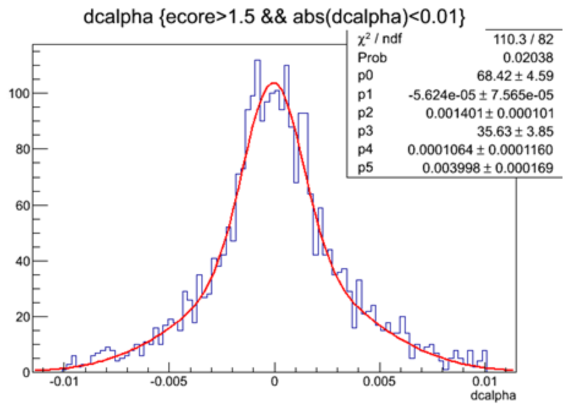

Figure 48: The α_{DC} distribution together with a double Gaussian fit.

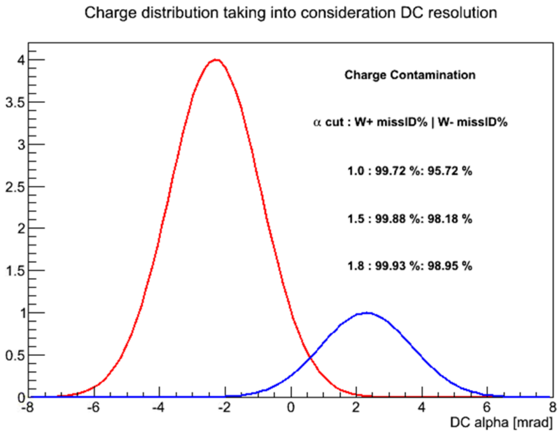

Figure 49: Charge misdentification study with percentages of remaining tracks that are misidentified after small α_{DC} removal.

the positive charges and 4.3% for the negative charges. Figure 50 shows the effect on the p_T spectrum for electron candidates with small α_{DC} removed as discussed in above.

3.3.2.6 Relative isolation cut The relative isolation cut is the largest discriminator of background in this analysis. It is defined by taking the sum of all the EMCal energy deposits (except the candidate energy) and DC

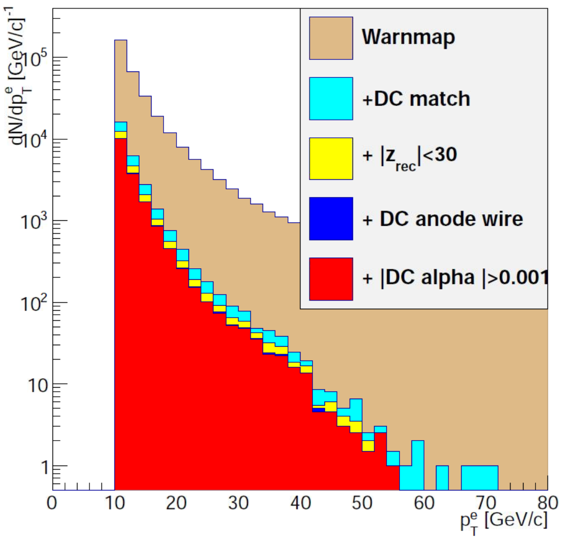

Figure 50: p_T spectrum for electron candidates with the small α_{DC} removed (in red) for 2012 data.

momenta in a cone of radius $R = \sqrt{\Delta\phi^2 + \Delta\eta^2} = 0.4$ around the candidate. Dividing the sum by the energy of the candidate gives the relative isolation cut variable.

The cone size and cut level for the relative isolation cut was determined through a study on the 2011 dataset. The data was analyzed and the relative isolation cut variable was calculated at 12 radii (from 0.05 to 0.60 in increments of 0.05). For each of these calculations p_T spectra were generated for relative isolation cut levels ranging between 0.01 to 0.5. 0.5 cut level means that the cone around the candidate contains half or less of the energy of the candidate. For each spectrum the background and signal fractions were determined with the use of a power law functional form (α/p_T^β), for the background, and the use of a jacobian peak shape for the signal[7] (see 3.3.4 for simulation details).

---

[7] Even though later during the course of the analysis it was established that the power law is not a good descriptor for the background shape, the low statistics of the 2011 dataset make the estimate for this study sufficient.

To determine the optimal cut level a standard significance was used:

$$S = \frac{\text{signal}}{\sqrt{\text{signal+background}}} \tag{45}$$

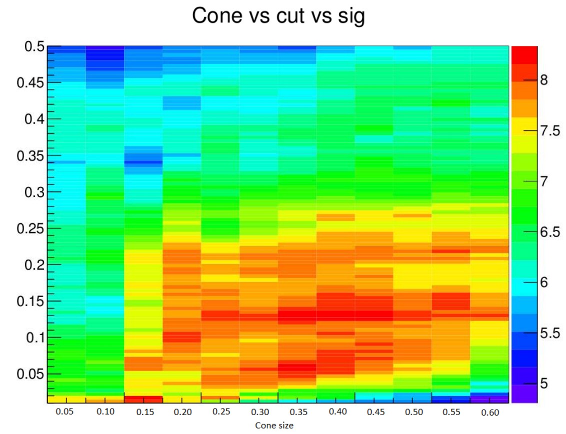

Figure 51: Significance as a function of cone size (x axis) and isolation cut (y axis) for multiple cone sizes.

The results of this study can be seen in figures 51, 52 and 53. Figure 51 shows the significance as a function of cone size (on the x axis) and as a function of relative isolation cut (on the y axis). Although there is no large difference between cone sizes around 0.4, it does contain the largest significance as defined above. Moreover, studies done in previous analyses resulted in the use of an identical cone size. The limited η range available to PHENIX makes it difficult to argue for any larger cone size.

Figure 52 shows the signal yield in red and estimated background yield in blue for a fixed cone size of 0.4. It can be seen that after a relative isolation cut of approximately 10% the signal counts remain approximately stable while the background fraction increasing more and more. Figure 53 gives the the significance calculated for each isolation cut level. As expected very small relative isolation cut reduces not only the background but also the signal, thus decreasing the overall significance. There is no clear maximum significance in the plateau around 10%. However since signal fraction decreases for lower values, 10% was chosen as the most aggressive cut that still preserves most of the signal.

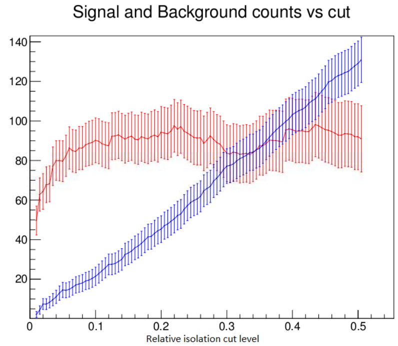

Figure 52: Signal (red) and background estimation (blue) for a cone size of 0.4 and different relative isolation cuts.

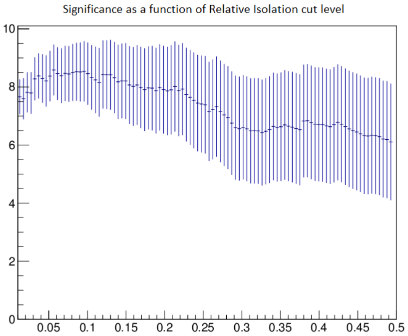

Figure 53: Significance as a function of relative isolation cut (for a cone size of 0.4).

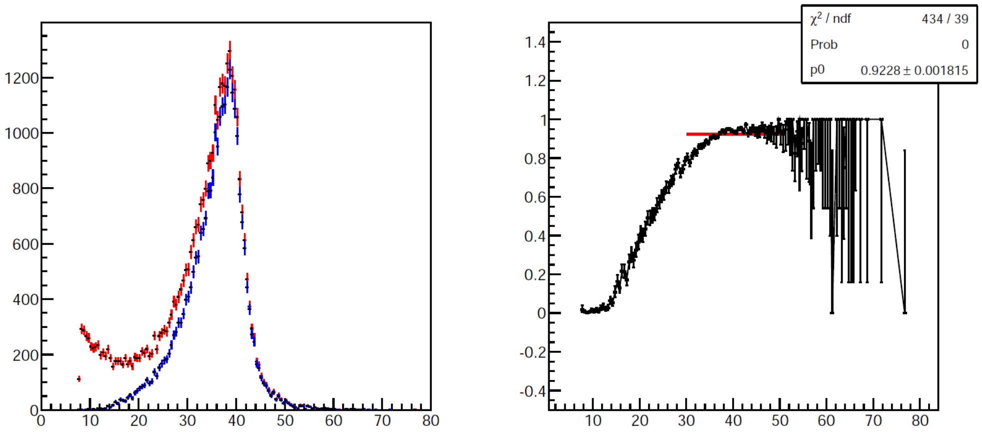

Figure 54: Left panel: simulated Jacobian peak without relative isolation cut (red) and with relative isolation cut (blue) for negative charges. Right panel: ratio of spectrum with isolation cut to spectrum without the isolation cut together with constant fit.

Using the simulation setup that is described in more detail in 3.3.4 W events are generated in PYTHIA and then passed through a realistic detector simulator (GEANT). These events are then passed through the same reconstruction and analysis chain as the real data. The resulting decay electron

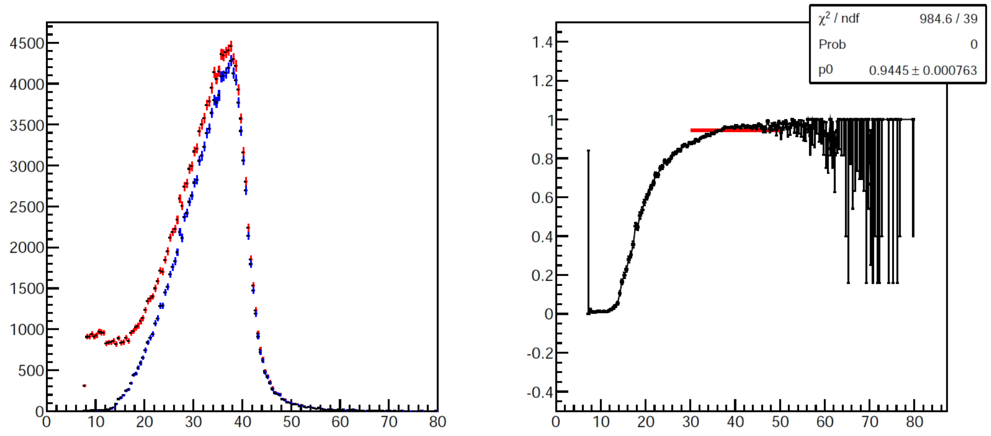

Figure 55: Left panel: simulated Jacobian peak without relative isolation cut (red) and with relative isolation cut (blue) for positive charges. Right panel: ratio of spectrum with isolation cut to spectrum without the isolation cut together with constant fit.

spectrum can be seen in figure 60 for W^+ and W^- respectively. Because the Z decay electrons are the largest contribution to the signal, this decay channel is simulated as well and resulting PYTHIA cross section weighted spectrum can be seen in figure 61. The effect of the relative isolation cut on these signal events, for the selected cone size and cut level, can be seen in figures 55 and 54 for the positive and negative charged particles respectively. The left panel of each figure shows the p_T spectrum before isolation cut (in red) and after the cut (in blue). The right panel of the figures shows the result of dividing each histogram with an isolation cut by the histogram without any isolation cut together with a constant fit in the region that is considered signal in this analysis (30 to 50 GeV). These plots clearly show that the isolation cut has only a marginal effect on the signal with ∼94% and ∼92% of the signal remaining the sample after the cut for the positive and negative charges, respectively.

Figure 56 shows the effect on the p_T spectrum for electron candidates with the relative isolation cut applied on top of previous cuts. As expected the relative isolation cut removes the largest fraction of background.

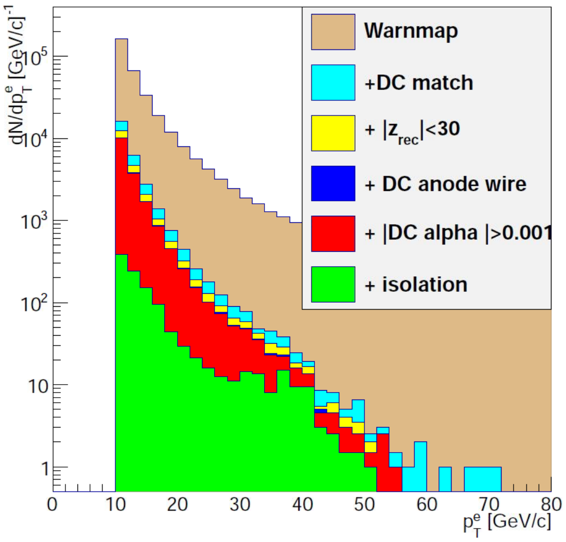

Figure 56: p_T spectrum for electron candidates with relative isolation cut applied (in green) for 2012 data.

3.3.2.7 VTX conversions After the data taking period in 2009 the Hadron Blind Detector was replaced with the Vertex Detector (VTX). This increased the radiation length in between the beam pipe and the DC approximately by a factor of 3. This implies a significant increase in the photon conversion background. In order to be able to identify these conversions two new variables are introduced to the analysis, ϕ_V and m_{ee} (this study was originally done for a previous PHENIX paper [43]).

The invariant mass of the electron-positron pair (m_{ee}) coming from a conversion will be proportional to the distance from the nominal interaction region where the conversion happens. This is because the DC reconstruction assumes that all tracks are from the interaction region and so the momentum is not reconstructed correctly for conversions.

The ϕ_V variable is basically the angle between the plane of the pair and the perpendicular plane to the direction of the magnetic field. It can show what pairs are consistent with a conversion opening up in the PHENIX magnetic field. It is defined as:

$$\phi_V = \left(\frac{p_1 \times p_2}{\|p_1 \times p_2\|} \times \frac{p_1 + p_2}{\|p_1 + p_2\|}\right) \cdot \left(\frac{(p_1 + p_2) \times B}{\|(p_1 + p_2) \times B\|}\right) \tag{46}$$

where p_1 and p_2 are the 3-momenta of the two tracks that are considered for pairing and B is the magnetic field vector. For this calculation the magnetic field strength is not as important as the direction, so it was chosen to be (0,0,1). ϕ_V takes values between 0 and π, with conversions having values close to 0.

Using simulated π^0 with photon conversions, the ϕ_V vs m_{ee} phase space is scanned for an area belonging to the VTX material and an area belonging to the support electronics.

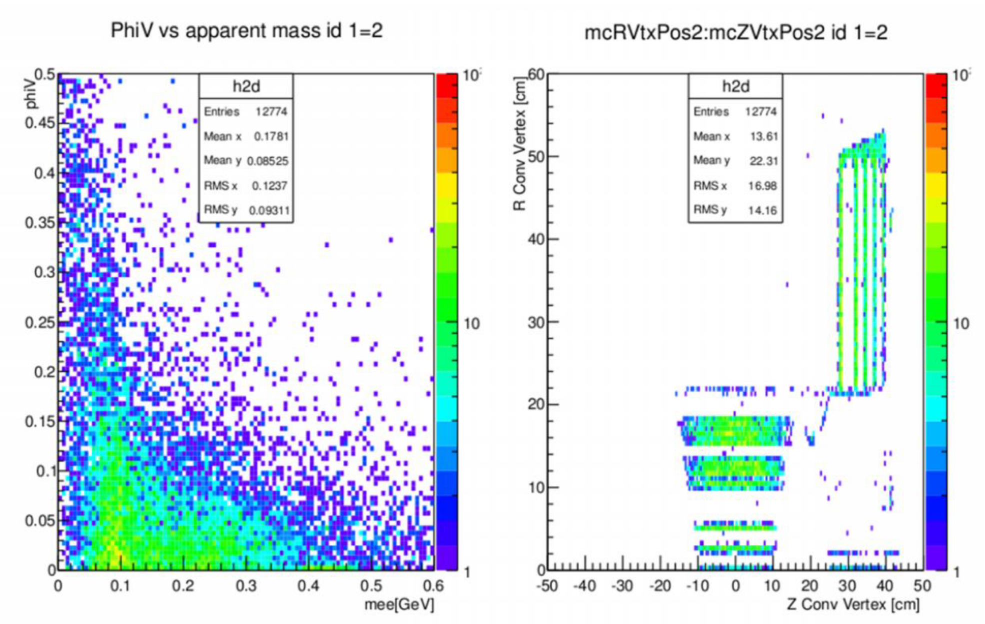

Figure 57: Small ϕ_V and m_{ee} phase space on the left hand side. Monte Carlo radius and z conversion vertex information on the right hand side.

As the only physics process turned on in the simulation, the ϕ_V vs m_{ee} phase space can be scanned to identify regions that are from conversions in the VTX layers and the VTX Big Wheels support structure. Figure 57 shows small ϕ_V and m_{ee} region (where conversions are expected) on the left hand side while the the right hand side shows the Monte Carlo radius R and z conversion vertex information. Both the VTX layers and support electronics can be seen in the right panel. Selecting on either one reveals that the region between 0.05 and 0.15 GeV for m_{ee} is mainly from conversions in the VTX material and the region between 0.15 and 0.35 GeV is from the support electronics. As expected the support electronics being further away from the collision point give a larger *invariant mass* for the pair. Applying the relative isolation cut on these simulated identified conversions results in a more than 99% removal of conversion pairs.

3.3.3 p_T spectra and yields

Using the cuts that were discussed in the previous subsection the p_T spectra for 2011 and 2012 were obtained as can be seen in figures 58 and 59 respectively. As expected in the region between 30 and 50 GeV there is a significant excess over the background.

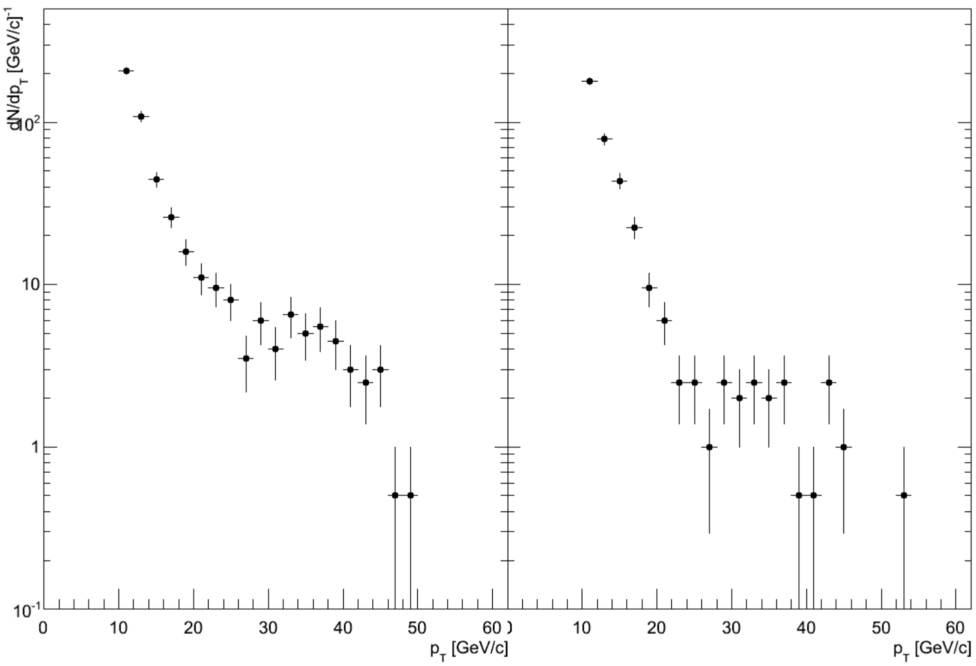

Figure 58: p_T spectra for positive (left) and negative (right) charges for 2011 data.

For the final result in this analysis, the single spin asymmetry, the spin separated counts are required. Taking the number of counts in the signal region (30 to 50 GeV) for both 2011 and 2012 each event can be separated

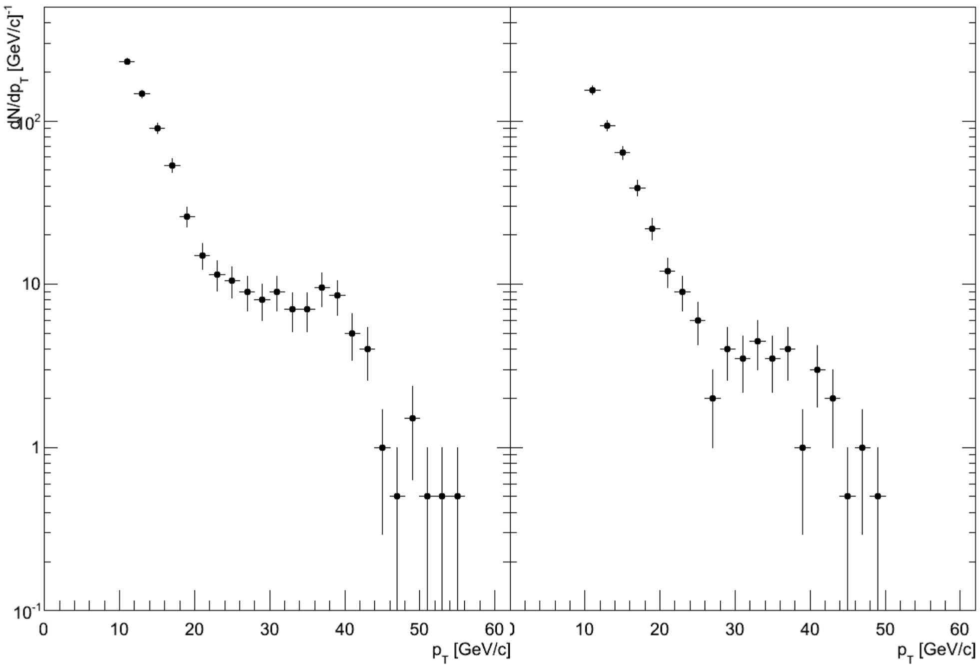

Figure 59: p_T spectra for positive (left) and negative (right) charges for 2012 data.

into one of four categories depending on the blue and yellow beam helicities for that event: ($++$ for blue beam positive helicity and yellow beam positive helicity, $-+$ for blue beam negative helicity and yellow beam positive helicity and $+-$ and $--$ for the other two combinations). Table 5 shows the yields separated by these spin crossings for the positive and negative charges for both years.

Although the background fraction is calculated in the signal region (as described below) a measurement has to be done to estimate the asymmetry of the background. Similarly to what was done for the signal region, the spin separated background yields are extracted from the data and presented in table 6 (the background region is defined between 10 and 20 GeV).

Run/Charge	BY:+ +	BY:− +	BY:+ −	BY:− −
2011/W^+	12	17	15	25
2011/W^-	8	7	7	5
2012/W^+	21	27	23	33
2012/W^-	16	15	8	8

Table 5: Spin separated yields in the 30 to 50 GeV region for 2011 and 2012 data.

Run/Charge	BY:+ +	BY:− +	BY:+ −	BY:− −
2011/W^+	193	196	205	208
2011/W^-	171	171	156	169
2012/W^+	90	93	93	104
2012/W^-	71	77	75	69

Table 6: Spin separated yields in the 10 to 20 GeV region for 2011 and 2012 data.

3.3.4 Background estimation

In order to obtain the final asymmetry value using the events in the 30 to 50 GeV region, a careful study of the background contamination of this signal region is needed. Several methods were attempted for this analysis which will be presented below. All of these methods make use the fact that the region between 10 and 20 GeV is background dominated. By characterizing this background through a functional form (as is the case for the power law and modified power law) and making use of a simulated signal shape, the entire p_T spectrum can be fit. The main descriptor for the background, Gaussian Process Regression (GPR) uses the p_T spectrum between 10 and 22 GeV to characterize the background shape and then extrapolate in the signal region. This extrapolated shape is also tested with the simulated signal shape against the entire spectrum.

3.3.4.1 Simulation To support this analysis a multistage Monte Carlo simulation chain was produced using the software structures already in place for PHENIX. There are three steps involved in this simulation:

- particle generation through the standard PYTHIA package (version 6.4.21 was used)

- detector response was simulated with the use of a GEANT-based package which has all the PHENIX central arm detectors configured
- reconstruction of the simulated detector signals through the same software chain as real data

Besides the single particle π^0 simulations used for studying the VTX conversions (discussed in 3.3.2.7), the most important simulation produced was that of the signal[8]. $W^\pm$ bosons were simulated with only the $e^\pm$ decay channels turned on. The vertex distribution was centered on the PHENIX origin (0,0,0) and with a realistic Gaussian distribution width (0.02,0.02,38.63) that was obtained from data. The analysis code used for the real data was used on the simulated events and the resulting $W^\pm$ p_T spectra can be seen in figure 60.

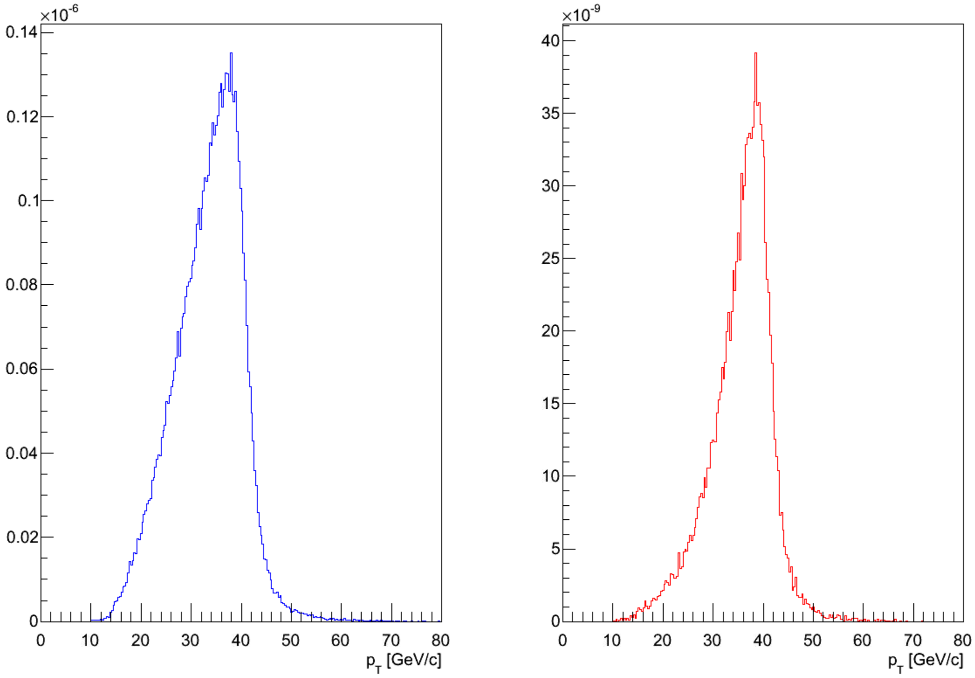

Figure 60: Simulated W p_T spectra for positive charges (left) and negative charges (right).

---

[8] Although attempts were made to simulate the entire background, the lack of an appropriate hadronic response for the PHENIX calorimeter made the resulting simulations to not agree with the data.

However, as noted before there is no real way to differentiate between decay electrons coming from Ws or $Z/\gamma*$. Since $Z/\gamma*$ are the largest contribution in the signal region, they were simulated as well and the cross section weighted p_T spectra were obtained (as can be seen in figure 61).

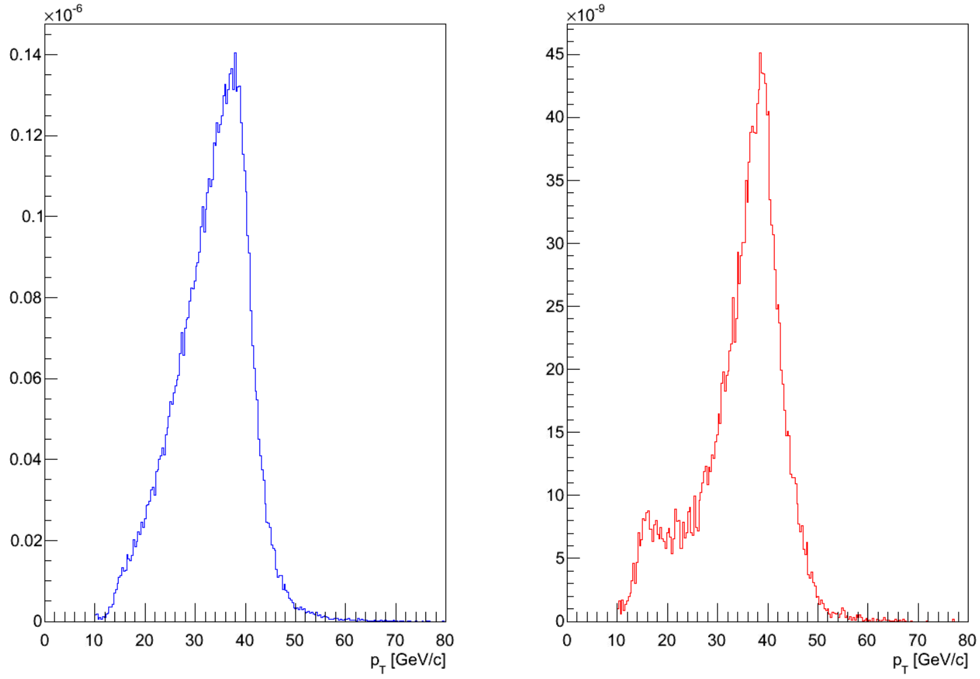

Figure 61: Simulated combined W and Z p_T spectra for positive charges (left) and negative charges (right).

This signal shape (figure 61) is used together with the background characterizations explained below for a final fit of the data in each case.

3.3.4.2 Power Law Several functional forms were attempted to characterize the background shape in both the background dominated region (10 to 20 GeV) and the signal region (where it was summed with the Jacobian peak discussed above). For the 2011 data analysis, a simple power law appeared to provide a reasonable ansatz:

$$f_p := \frac{\alpha}{p_T^{\beta}} \tag{47}$$

where α and β are parameters that can be extracted from a fit to the data.

The results of a simultaneous fit of the power law and Jacobian peak over the entire p_T spectrum can be see in figure 62 for both positive (left hand side) and negative (right hand side) charges. The fit function used was

$$F_p := \frac{\alpha}{p_T^{\beta}} + \gamma \cdot \text{Jacobian} \tag{48}$$

where Jacobian is the contents of the simulated shape at each p_T point. All throughout this thesis fits are performed using the standard ROOT analysis package with a χ^2 minimization procedure derived from the MINUIT package.

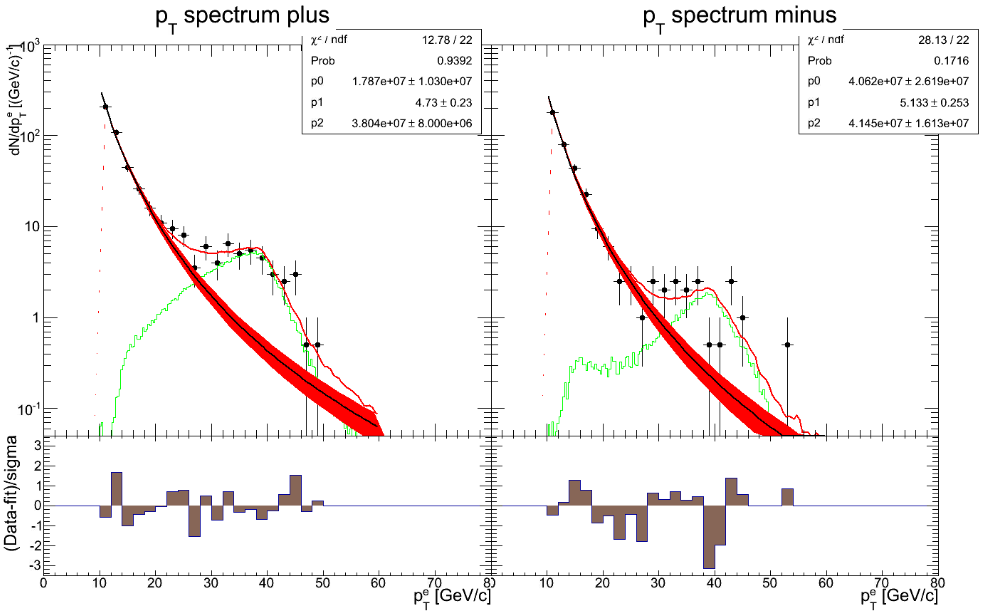

Figure 62: Power law fit together with Jacobian peak shape fit to the 2011 p_T spectra for positive charges (left) and negative charges (right).

The fit result can be seen in figure 62 with the data in black [9], the overall fit (background and signal) in red, Jacobian peak shape in green and the power law background estimate in black with a red band for the uncertainty

---

[9] The y-axis represents the number of counts in each bin divided by the width of the bin.

estimate. Below each plot is a χ distribution (difference between data and fit divided by the uncertainty on the data) showing the uncertainty scaled difference between data and fit. The starting point for the fit was varied (starting at 12 and 14 GeV) and the resulting 2 central value curves were all consistent with the initial 10 GeV fit.

However, when this method was attempted for the 2012 data it was quickly discovered that the power law was not a good descriptor for the data. As can be seen from figure 63 the different fit curves for the variation of the starting point of the fit provide very different results for both charges. The χ distribution on the bottom is for the 10 GeV fit. Not only did the background contributions have a large variation (going from 35 counts to 15 counts for the W^+ for the 10 GeV fit and 15 GeV fit), but also the fit parameters that resulted were very different (the β parameter in equation 47 was 5.2±0.4 for the 12 GeV fit and 4.0±0.2 for the 14 GeV fit).

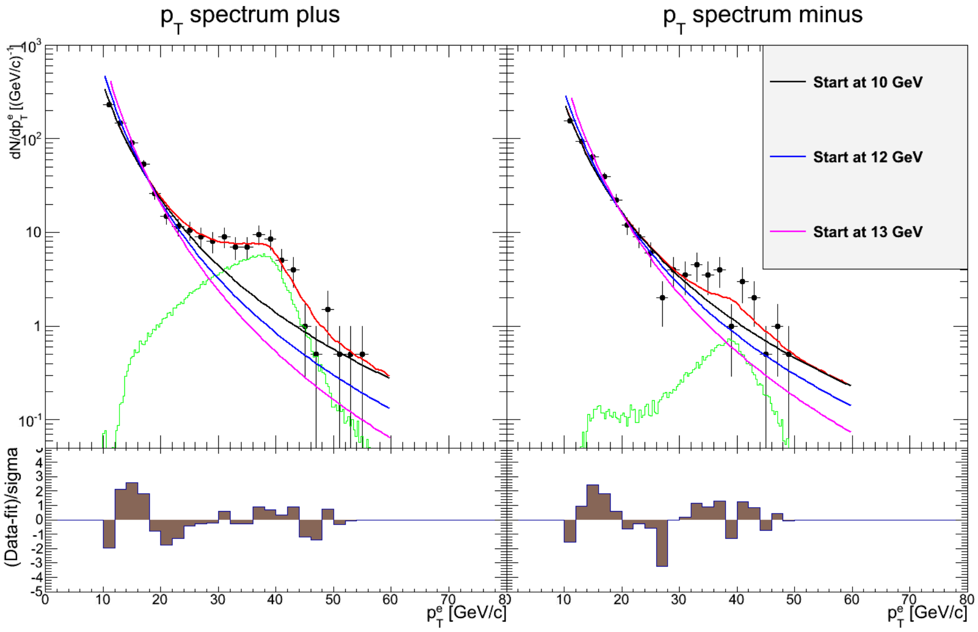

Figure 63: Power law fits together with Jacobian peak shape fit to the 2012 p_T spectra for positive charges (left) and negative charges (right) with different starting positions.

3.3.4.3 Gaussian Process Regression A new method was needed to describe the background shape. A normal regression fit can be thought of as prior knowledge over parameters (through the functional form). However, since in this case there was no apriori knowledge for this functional form, the focus was shifted to prior knowledge over functions. There are a few minimal expectations regarding a function that describes the background in this analysis:

- it should be smooth (the derivatives for these functions should not be discontinuous)
- it should be steeply falling
- and it should agree with the data

Such constraints can be imposed through the use of a Gaussian Process for Regression (GPR). A short introduction to the topic, with the necessary information for this analysis and an example will be given here (a more thorough description can be found in appendix A and the references within). Using the GPR one can select a whole class of functional forms through a kernel (or covariance) function which will give the differentiability of the functions that will be checked against the data. This kernel function usually has a set of parameters (called hyperparameters) that give it flexibility and can be determined from the input data (in this case the 10 to 22 GeV region was used because it is a background dominated region). The kernel function is a two point function that gives the degree of correlation between two points.

For this analysis the standard Radial Basis Function is employed:

$$k(x_j, x_i) = \sigma_f^2 \exp\left(-\frac{(x_i - x_j)^2}{2l^2}\right) + \sigma_i^2 \delta(x_i, x_j), \tag{49}$$

where x_i is the x coordinate for point i, σ_i is the statistical uncertainty on point i, $\delta(x_i, x_j)$ is the Kronecker delta and σ_f and l are the hyperparameters for this covariance function. σ_f gives a normalization for the covariance that will be of appropriate size compared to the uncertainties of the input points. l gives the characteristic length after which the correlation between two points decreases by ∼68%.

Besides the input points, a set of query points is determined that span the whole region of interest (by equally spacing them between the end points of the region). By calculating this kernel function for all the combinations for the input points and output points, a covariance matrix is obtained which through the mathematical description provided in A.3 can be used to uniquely determine the hyperparameters. This determination is done by minimizing the differences between the data and the predictions and by selecting the simplest model (with the smallest covariance matrix determinant).

An intuitive way to think about the GPR is that it selects functions that agree reasonably well with the data through the covariance matrix. For example given the points in figure 64, a prediction is needed in the region between -1.6 and 0.1. By using the covariance matrix to provide the correct correlation throughout the range, functions can be sampled as can be seen in figure 65.

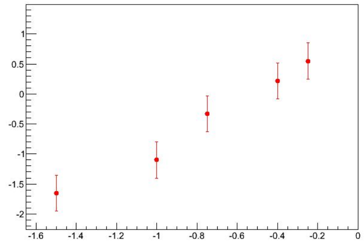

Figure 64: Example input points for GPR.

In figure 65 the red points are the input points, the black (and blue error bars) points are the GPR predictions and the green lines are functions that are sampled to agree reasonably well with the data. As can be seen most functions stay quite close to the data, but from time to time one function that has a large deviation is sampled.

By sampling over a large number of times one can obtain something like what is shown in figure 66. Again, the red points are the input data and the black line is the central value prediction of the GPR. The color histogram in the background is the result of filling each bin whenever a function that was sampled satisfies the condition $y = f(x)$ with (x,y) being the coordinates of that particular bin. As can be seen, most of the functions pass through points that are very close to the data. Not only this, but by taking slices at each x coordinate one would obtain an one dimensional Gaussian, with the mean as the prediction for that point and the width as the uncertainty.

Using this method the background shape was extracted for both positive and negative charges for the 2011 and 2012 data. Figures 67 and 68 show

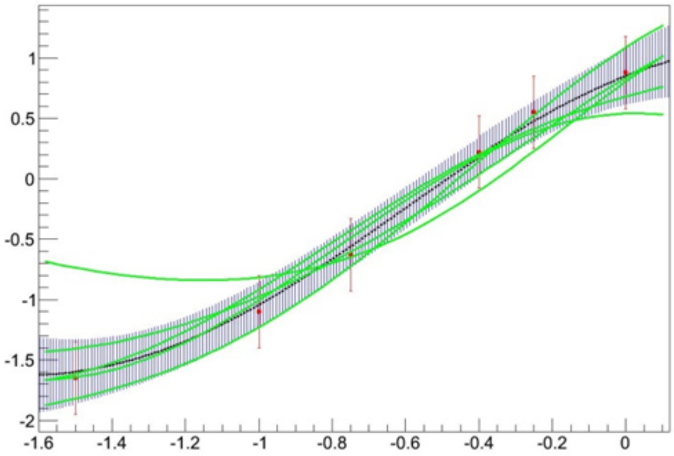

Figure 65: Sampling a few functions from data using the GPR on the example points.

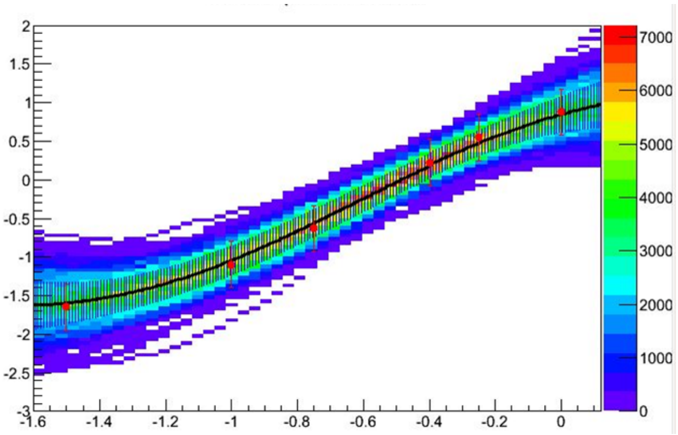

Figure 66: Sampling 50 000 functions gives a prediction at each point in x.

the result of the GPR determination in the region between 9 and 65 GeV. Although the GPR method performs very well for interpolation problems (see discussion in section 45 of [44]) special care has to be taken when using this method to extrapolate to regions that are far away from the data. In this case the extrapolation region is ∼20 units in p_T from the data (taking the midpoint between 30 and 50 GeV).

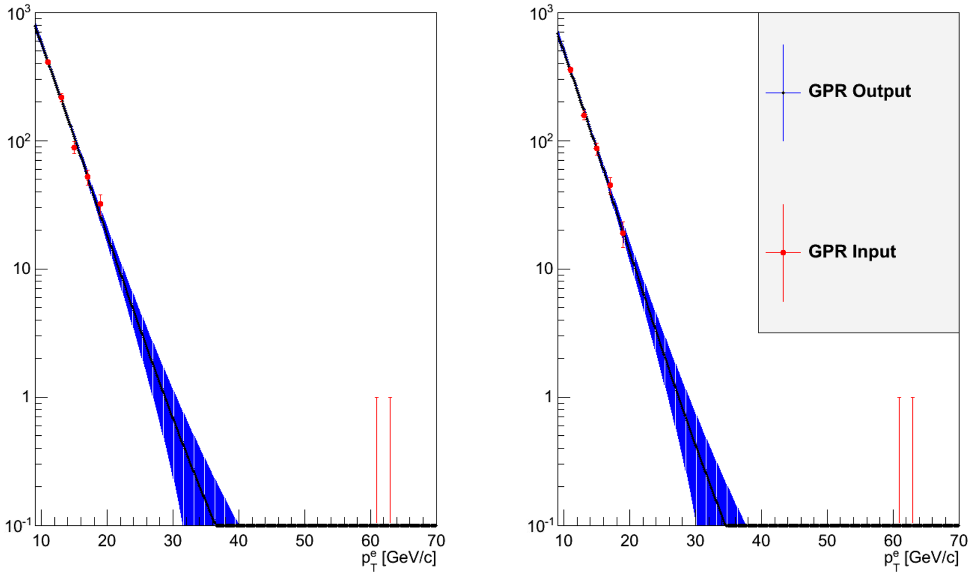

Figure 67: Background shape determination for positive (left) and negative (right) charges using the GPR for 2011 data.

A good indicator for how appropriate this method is in a particular range is the characteristic length parameter l. As specified before the characteristic length gives the distance at which the correlation between two points is smaller by ∼68% compared to the self correlation of one point. This means that this method does not identify long range patterns in data. Furthermore, if a prediction is requested at distances that are far away from available data the GPR will return a value of 0 with a set uncertainty (as can easily be calculated from the mathematical description in A.3). The characteristic length is determined from the minimization of function (equation 64) that takes into account deviations from available data and model complexity. As such, for each dataset the procedure implemented for this analysis will give out the hyperparameters that best minimize this function. The initial characteristic lengths obtained for the 2011 and 2012 data were around 30 units in p_T. Even though these distances would cover the range of interest, a more robust way to perform the analysis is to include the information at higher p_T, where there were no counts in the spectra. As can be seen from figures 67 and 68 two points were added as input for the GPR at 61 and 63 GeV

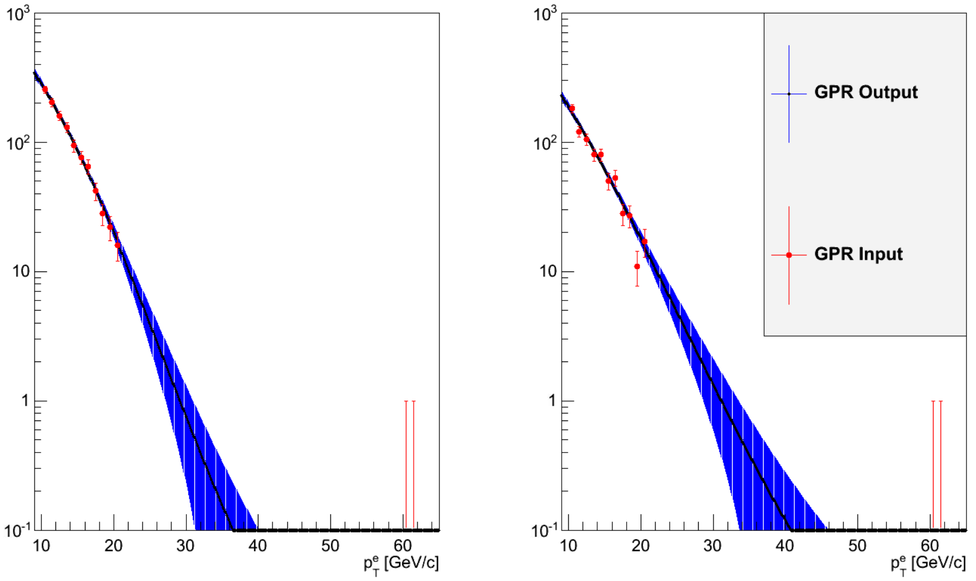

Figure 68: Background shape determination for positive (left) and negative (right) charges using the GPR for 2012 data.

with 0 counts and an uncertainty of 1. The resulting hyperparameters can be seen in table 7 together with the integral of the background contribution in the 30 to 50 GeV region for each year and each charge.

Run/Charge	σ_f	l	$\int_{30}^{50}$ GPR dp_T
2011/W^+	11.15	48.83	2.3 ± 2.2
2011/W^-	10.82	45.71	1.4 ± 1.4
2012/W^+	6.37	31.43	2.50 ± 2.5
2012/W^-	10.82	45.71	5.5 ± 4.7

Table 7: GPR hyperparameters and background contributions.

The background shape for each of case was tested against the data together with the simulated Jacobian peak. The results together with the χ distribution can be seen in figures 69 and 70 for 2011 and 2012 respectively.

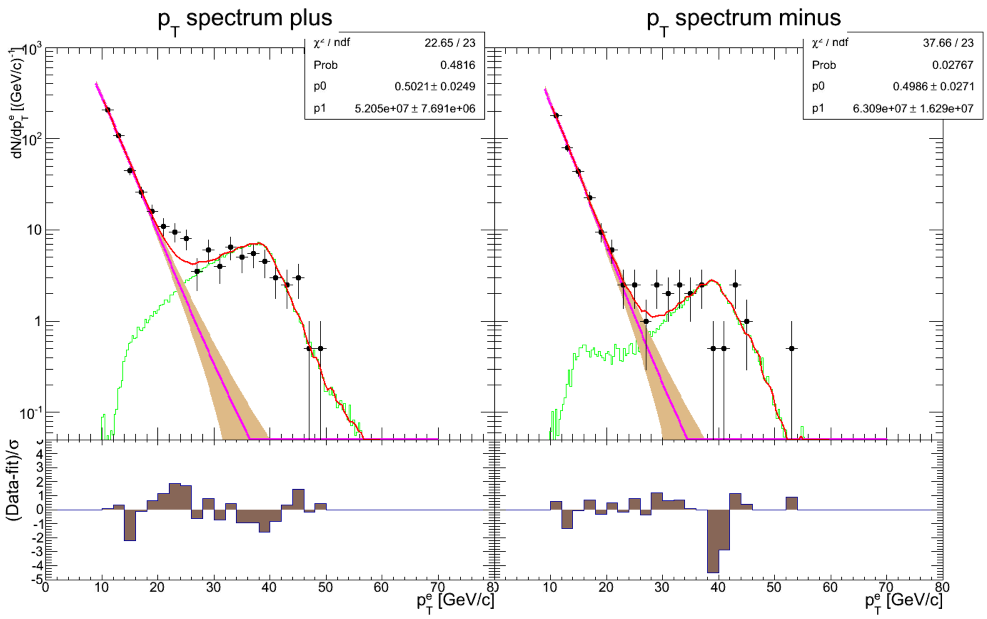

Figure 69: GPR background and simulated signal shape fit to the 2011 data. Left: positive charges, Right: negative charges.

The fits in 69 and 70 show a very good consistency of the signal and background shapes to the data as can be seen from the χ^2 value being close or smaller to 1 for all but the 2011 negative charge fit. However, for this particular fit the largest contributions to the χ^2 are the two low bins around 40 GeV, where the dominant contribution is from signal events.

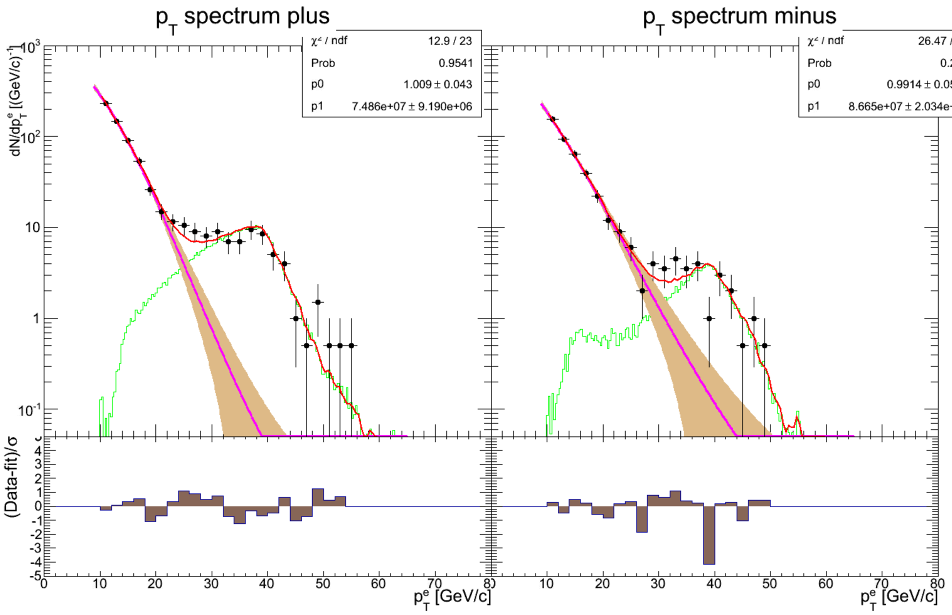

Figure 70: GPR background and simulated signal shape fit to the 2012 data. Left: positive charges, Right: negative charges.

3.3.4.4 Gaussian Process Regression cross checks Two cross checks have been performed on the GPR background estimation method. The first cross check consists of producing fake data by sampling a known background shape and signal. In this way the background contamination in the 30 to 50 GeV region is known beforehand and can be directly compared to the GPR estimate. Using the ROOT functionality to sample a certain number of events from a known shape, fake background events were randomly selected from a power law shape (the red points in the left panel of figure 71).

Using the simulated Jacobian shape signal events are sampled (the crosses in the left panel of figure 71). Adding these two histograms together gives the fake data as can be seen in the right panel of figure 71. Using the same methodology as was described above (selecting the data between 10 and 22 GeV as the input for the GPR and making predictions all the way to 55 GeV) gives a background estimate that can directly be compared to the input. Since the sampling of the background is done randomly, a series of 1000 samples were taken and processed. For each sample the GPR estimated number of counts are subtracted from the known background and plotted in the

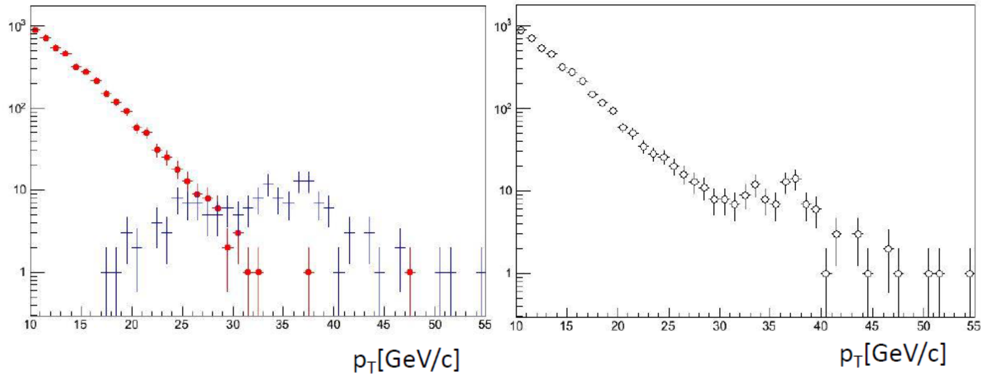

Figure 71: Left: fake background (red) and signal randomly extracted from known distributions. Right: the sum of the two histograms on the left.

left panel of figure 72. The uncertainty of each point is the uncertainty from the GPR estimate. As expected, the values fluctuate statistically around 0.

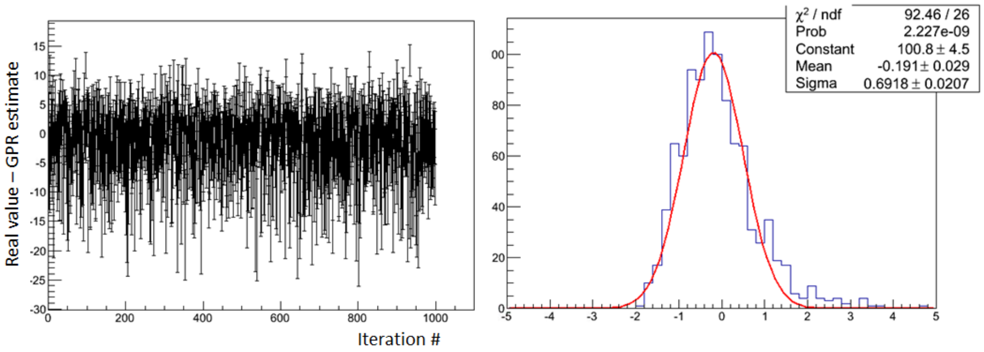

Figure 72: Left:For each iteration of the study the difference between the actual background value and the GPR result. Right: Uncertainty scaled distribution for the difference between actual background value and the GPR result together with Gaussian fit.

If this was truly a statistical fluctuation, putting the deviations from the actual background scaled by the uncertainty given by the GPR into a histogram should give a Gaussian distribution with a mean of 0 and a σ of 1. This test can be seen in the right panel of figure 72. The resulting fit with a Gaussian function shows that this distribution has a mean at -0.19 and a σ of 0.7. This indicates that the uncertainties from the GPR are in fact overestimated. While the mean is not at 0, the overestimation of the uncertainty covers for this systematic effect.

A second, more classical, cross check was performed by using a functional form to describe the background. Through trial and error, a modified power law function (as in equation 50) was obtained that was consistent with the data for 2011 and 2012. Furthermore, this modified power law produced consistent results when varying the starting position of the fit.

$$f_{Sp} := \frac{1}{p_T^{\alpha+\beta\cdot\log p_T}} \tag{50}$$

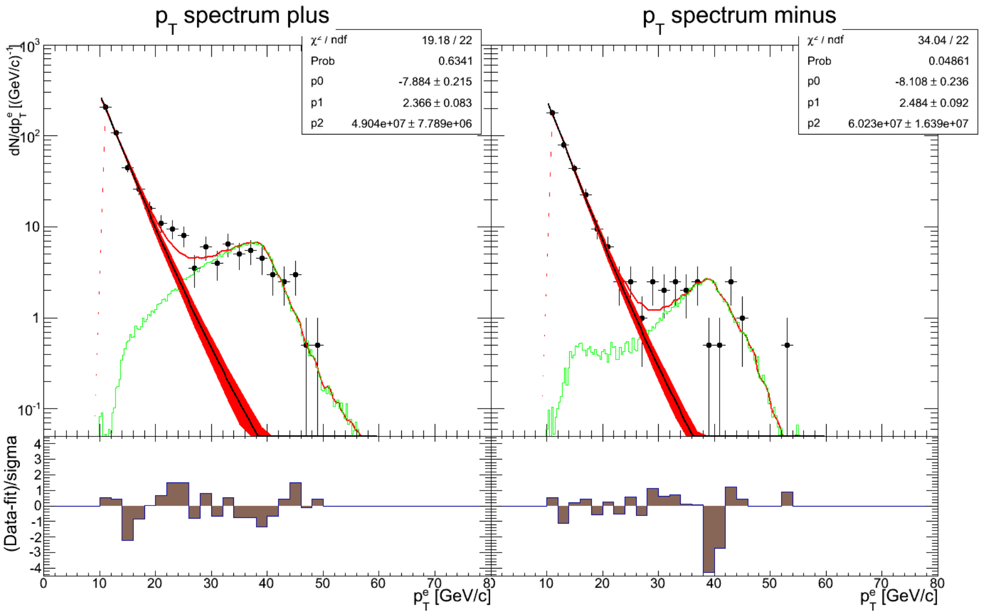

Figure 73: Modified power law function fit together with simulated Jacobian peak for positive (left) and negative (right) charges in 2011 data.

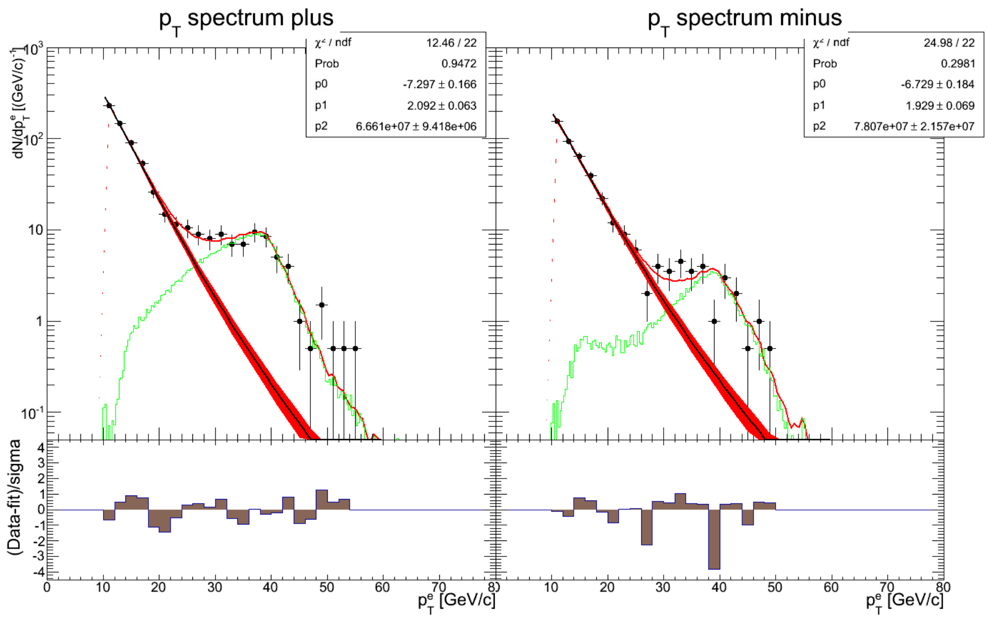

Figure 74: Modified power law function fit together with simulated Jacobian peak for positive (left) and negative (right) charges in 2012 data.

The fit together with the simulated signal shape and χ distribution can be seen in figures 73 74 for the 2011 and 2012 data respectively. The fit variation for starting the fit at different points (10 GeV for the band, 12 and 14 GeV for the cross checks) can be seen for the 2012 data in figure 75.

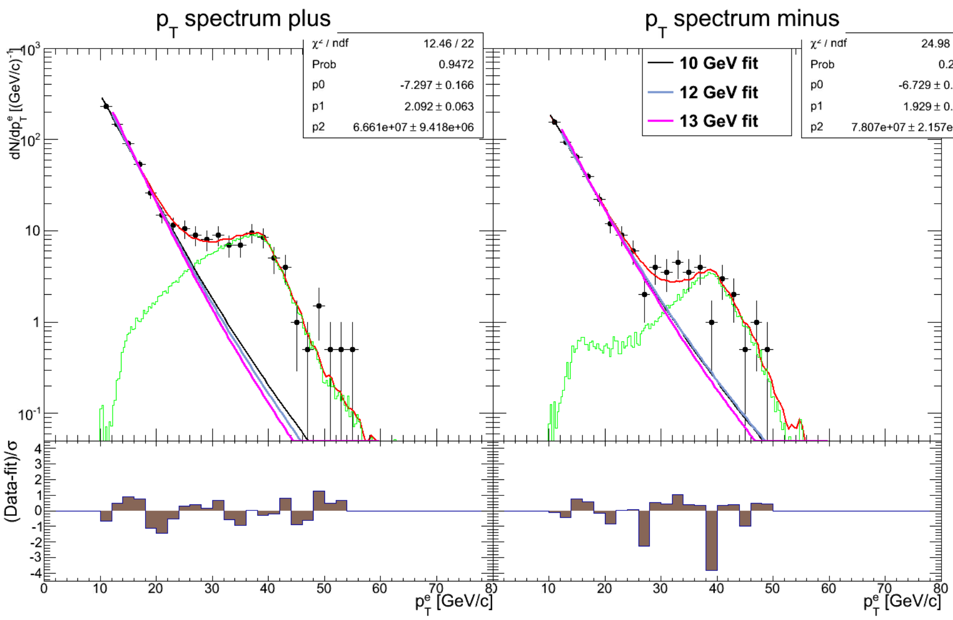

Figure 75: Modified power law function fit to 2012 data with different starting points.

The fit parameters from equation 50 together with background contribution estimated in the region between 30 and 50 GeV from the modified power law can be found in table 8.

Run/Charge	α	β	$\int_{30}^{50}$ mPwrL dp_T
2011/W^+	-7.88 ± 0.22	2.37 ± 0.08	1.7 ± 1.2
2011/W^-	-8.11 ± 0.24	2.48 ± 0.09	1.01 ± 0.85
2012/W^+	-7.23 ± 0.16	2.09 ± 0.06	7.2 ± 1.3
2012/W^-	-6.73 ± 0.18	1.93 ± 0.07	7.7 ± 1.3

Table 8: Modified power law fit parameters and background contributions.

A comparison was done between the two background estimation methods (GPR and modified power law fit) and the result can be seen in figure 76 and 77 for the 2011 and 2012 data respectively. The overlapping uncertainty bands of these two methods show good agreement. Even though the agreement is reasonable, a systematic uncertainty was obtained from the difference

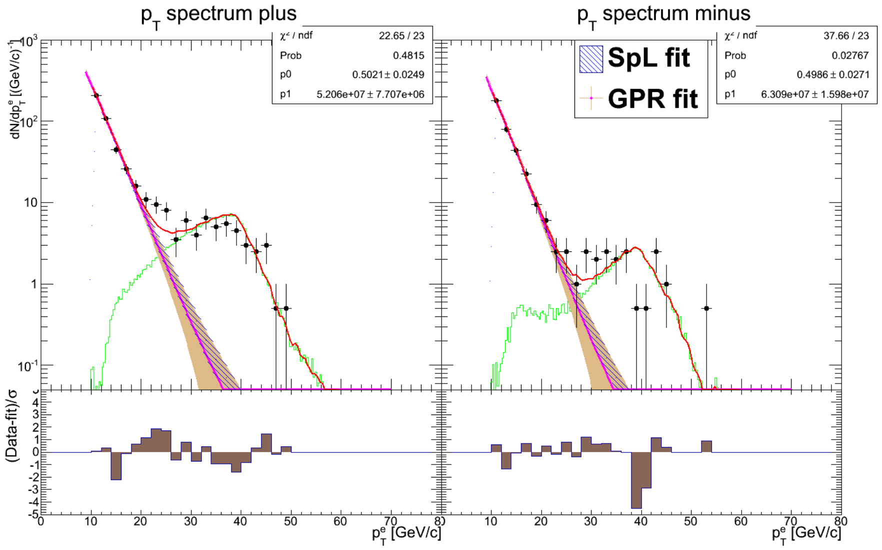

Figure 76: Comparison of GPR and modified power law background shapes for positive (left) and negative (right) charges in 2011 data.

between the central values for background estimation coming from these two methods, as explained in 3.3.5.2.

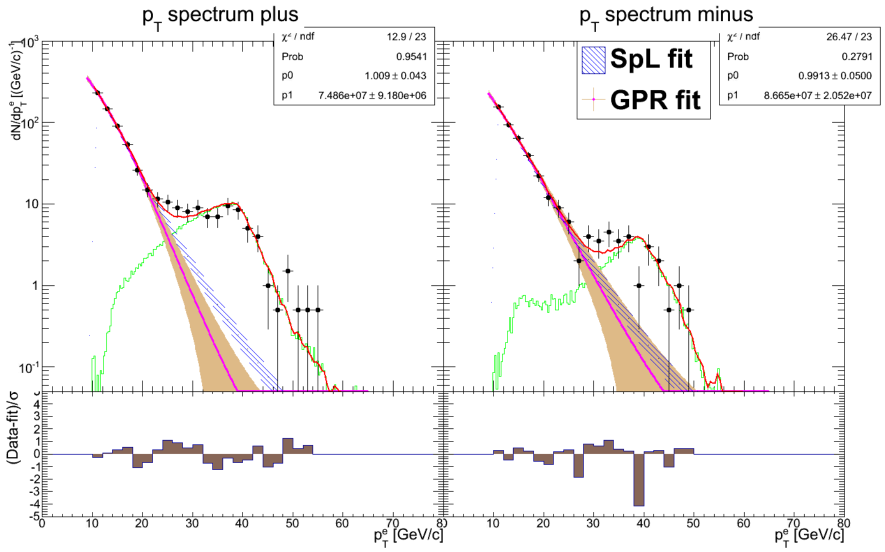

Figure 77: Comparison of GPR and modified power law background shapes for positive (left) and negative (right) charges in 2012 data.

3.3.5 Asymmetry Calculations

At this point all the necessary components needed to calculate the single spin asymmetry are on hand. By taking the yields that were presented in table 5, the polarization values from table 4 and with the relative luminosity numbers in table 3 the asymmetry values can be calculated using equations 22 and 23. For each W charge the single spin asymmetries can be calculated independently for each beam (since for single spin asymmetries the polarization values of the other beam are averaged by taking the sum). The double spin asymmetries, as the name implies, takes the polarization of both beams into account and as such there is only one value for each W charge.

From table 10 it can be seen that all the background asymmetries are consistent with 0. This means that the background does not bring any asymmetry contamination, but only dilutes the signal asymmetry. An explanation of how the background fraction is taken into account is given in 3.3.5.2.

3.3.5.1 Maximum likelihood A_L Since the spin separated counts are quite low (in table 5 the lowest number of counts is the 2011 W^- $--$ pattern at 5 counts) a better way to properly estimate the asymmetries and

	Signal		
Run/Charge	$A_{L,blue}$	$A_{L,yellow}$	A_{LL}
2011 W^+	-0.40 ± 0.23	-0.36 ± 0.24	0.24 ± 0.47
2011 W^-	0.22 ± 0.38	0.21 ± 0.38	-0.14 ± 0.75
2012 W^+	-0.27 ± 0.18	-0.18 ± 0.17	0.13 ± 0.31
2012 W^-	0.07 ± 0.27	0.55 ± 0.24	0.08 ± 0.47

Table 9: Asymmetry values for the signal region for 2011 and 2012 data.

	Background		
Run/Charge	$A_{L,blue}$	$A_{L,yellow}$	A_{LL}
2011 W^+	-0.017 ± 0.069	-0.072 ± 0.070	0.01 ± 0.13
2011 W^-	-0.041 ± 0.076	0.037 ± 0.077	0.08 ± 0.15
2012 W^+	-0.049 ± 0.055	-0.030 ± 0.053	0.047 ± 0.096
2012 W^-	-0.069 ± 0.066	0.035 ± 0.064	-0.04 ± 0.12

Table 10: Asymmetry values for the background region for 2011 and 2012 data.

uncertainties is to take into account Poissonian statistics. Using the spin separated cross sections from equation 24 a maximum likelihood function can be obtained as in equation 51.

$$\mathcal{L} = \mathbb{P}(\sigma_{++}, N_{++}) \cdot \mathbb{P}(\sigma_{-+}, N_{-+}) \cdot \mathbb{P}(\sigma_{+-}, N_{+-}) \cdot \mathbb{P}(\sigma_{--}, N_{--}) \tag{51}$$

where $\mathbb{P}(\sigma_{++}, N_{++})$ is the Poisson distribution with mean σ_{++} and N_{++} number of events.

Through these spin separated cross sections and the equations in 24 the single spin asymmetry A_L, double spin asymmetry A_{LL} and overall cross section can be obtained. As an example, equation 52 (the cross section when the blue beam has positive helicity and the yellow beam has negative helicity) contains σ_0 as the overall cross section (a parameter that is not of interest in this analysis), $P_{1,2}$ is the polarization of the blue or yellow beam respectively, and the A_L and A_{LL} are the two quantities of interest (single and double spin asymmetries). In each of the other 3 equations the A_L and A_{LL} are the same quantity, making it possible that by scanning a phase space for A_L, A_{LL} and σ_0 one can find the maximum probability for these parameters.

$$\sigma_{+-} = \frac{N_{+-}}{L_{+-}} = \sigma_0(1 + A_L(P_1 - P_2) - A_{LL}P_1P_2) \tag{52}$$

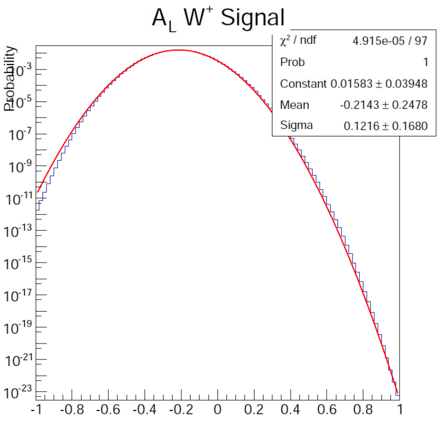

Figure 78: 2012 W^+ Signal single spin asymmetry.

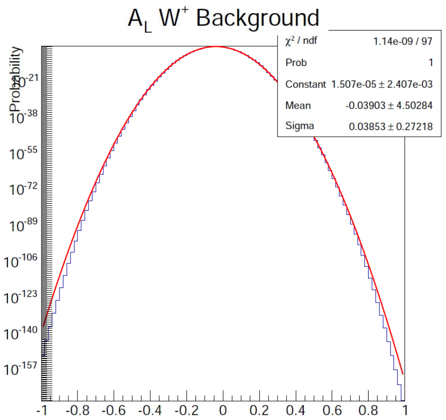

Figure 79: 2012 W^+ Background single spin asymmetry.

Figures 78 and 79 show the 1 dimensional projections of the 2012 W^+ maximum likelihood phase space scan for the single spin asymmetries in the case of the signal region and background region respectively. The rest of the figures for the 2012 W^- and the 2011 data can be found in appendix D. For each asymmetry the phase space scan projection was fit with a Gaussian and the mean of the distribution was selected as the central value while the width was used as the uncertainty of that asymmetry.

A summary of the results can be found in figures 80 and 81 for the 2011 and 2012 data respectively. The black points correspond to the asymmetry values that can be found in tables 9 and 10 while the red points correspond to the maximum likelihood calculated values. The single spin asymmetries for the signal region can be found in table 11.

Run	W^+	W^-
2011	-0.36 ± 0.16	0.19 ± 0.24
2012	-0.21 ± 0.12	0.29 ± 0.18

Table 11: Single spin asymmetry values for the signal region using the Maximum Likelihood calculation method.

3.3.5.2 Background dilution factor As mentioned before the fact that the background has no measurable asymmetry means that it only dilutes the

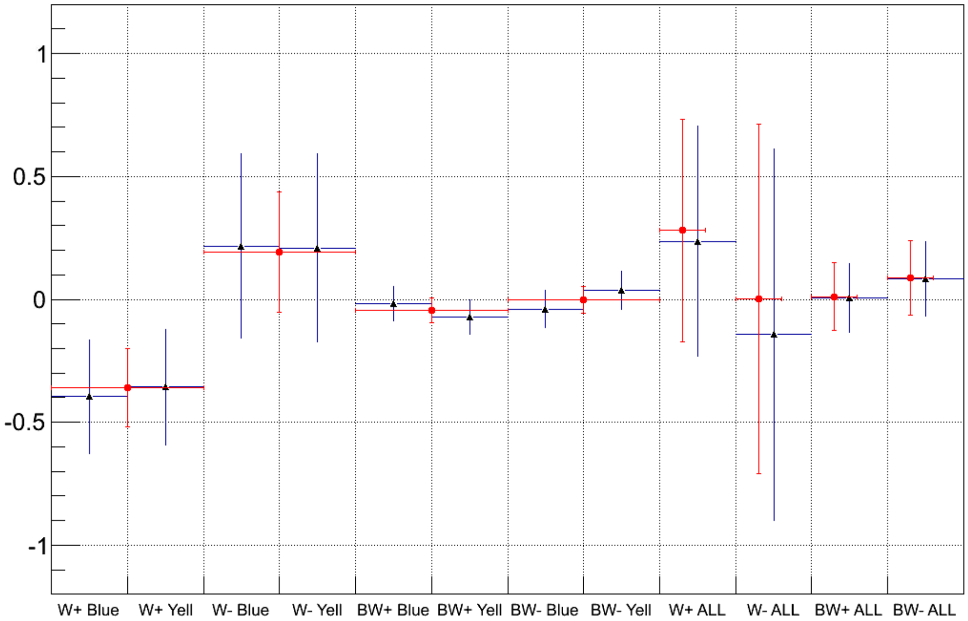

Figure 80: Single and double spin asymmetries for W$^{\pm}$ single and background regions for 2011 data. Blue shows classical asymmetry calculation values while red shows the Maximum Likelihood values.

asymmetry when present in the signal region. For example if the signal region contained 100 signal counts with asymmetry of 1 and 100 signal counts with asymmetry of 0, the calculated asymmetry would come out as 0.5. The final asymmetry values are calculated using equations 53 and 54 (putting the 1/2 dilution factor in these equations would make the example asymmetry go to the actual value of 1).

$$A_{L,f} = \frac{1}{\beta_{\pm}} A_{L,old} \tag{53}$$

$$\Delta A_{L,new} = A_{L,new} \cdot \sqrt{\left(\frac{\Delta\beta}{\beta}\right)^2 + \left(\frac{\Delta A_{L,old}}{A_{L,old}}\right)^2} \tag{54}$$

where $A_{L,old}$ are the values presented in table 11. The results for the final single spin asymmetries are presented in table 12.

Using the background estimation from the modified power law (table 8) and performing all the calculations again, a systematic was obtained from

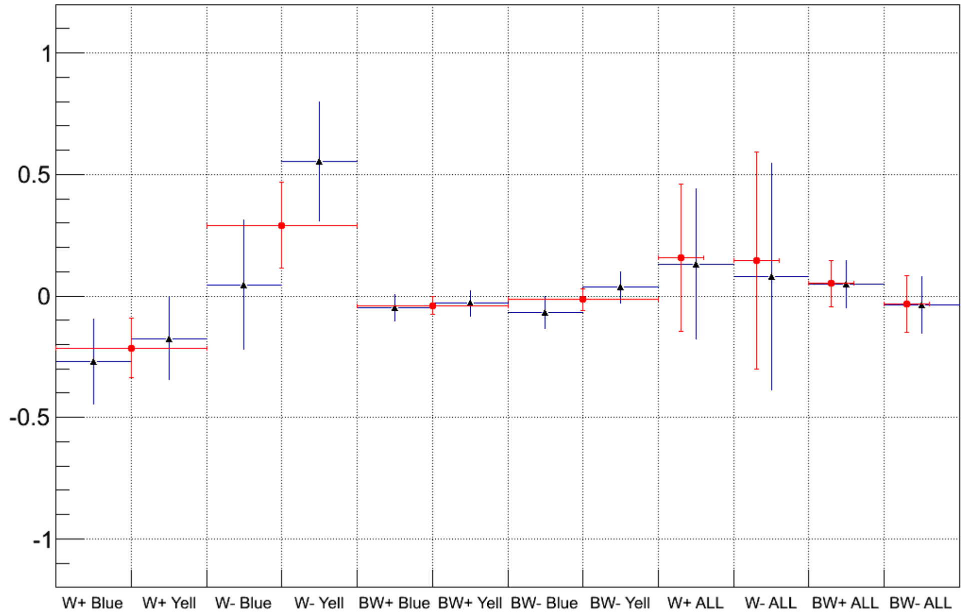

Figure 81: Single and double spin asymmetries for $W^{\pm}$ single and background regions for 2012 data. Blue shows classical asymmetry calculation values while red shows the Maximum Likelihood values.

the difference between the central values calculated with the GPR and the modified power law background estimations. This systematic uncertainty can be seen together with the statistical uncertainty in table 12.

Run	W^+	W^-
2011	$-0.37 \pm 0.17(\text{stat}) \pm 0.01(\text{syst})$	$0.20 \pm 0.26(\text{stat}) \pm 0.01(\text{syst})$
2012	$-0.22 \pm 0.12(\text{stat}) \pm 0.01(\text{syst})$	$0.33 \pm 0.20(\text{stat}) \pm 0.02(\text{syst})$

Table 12: Single spin asymmetry values for the signal region using the Maximum Likelihood calculation method.

As mentioned before, since the difference in beam energies between the two runs has a minimal effect on the asymmetries the two data sets have been combined using an uncertainty weighted average. The estimated systematic uncertainties for the two runs have been added in quadrature to provide a final systematic uncertainty. The results can be found in table 13.

Charge	A_L
W^+	$-0.27 \pm 0.10(\text{stat}) \pm 0.01(\text{syst})$
W^-	$0.28 \pm 0.16(\text{stat}) \pm 0.02(\text{syst})$

Table 13: Single spin asymmetry values for combined data sets using the values from table 12.

4 Discussion and Conclusions

The analysis in this thesis has been performed on the 2011 and 2012 data collected by PHENIX at $\sqrt{s} = 500$ and 510 GeV respectively. The extraction of large longitudinal parity violating single spin asymmetries from W decay electrons and positrons has been presented. Using the Gaussian Processes for Regression, a novel aproach for the determination of the background dilution factor has been developed and implemented in the PHENIX analysis framework. Two cross checks for the background shape determined from the GPR have been performed: a) the GPR background shape together with a simulated Jacobian peak have been shown to agree very well with the data b) an functional form ansatz was used for the background shape, providing results that were consistent with the GPR determination within uncertainties. Nevertheless, the small difference was taken as a systematic uncertainty.

Figure 82 shows the asymmetry results for the three data sets available (the published 2009 PHENIX result in black, the 2011 and 2012 data from this thesis in red and blue respectively). The boxes around the points represent the systematic uncertainties estimated for each data set. As explained before, because of the experimental imposibility to remove the Z to $e^{\pm}$ decay electrons/positrons, the asymmetries presented are for $W + Z$ decay electrons/positrons.

These asymmetries are compared with global analysis predictions performed under different conditions. The GRSV global analysis [45] is an early analysis performed on DIS and SIDIS data. It provides two different scenarios for the sea quarks. The standard (GRSV std) has a symmetric sea between the quarks and anti-quarks, while the GRSV valence (GRSV val) presents the case when the sea SU(2) symmetry is broken. A more recent global analysis, DSSV [4], analyzes an updated set of DIS and SIDIS data and takes into account for the first time proton proton collision data[10]. Furthermore, by replacing the DSS fragmentation functions and taking into account other fragmentation functions for the SIDIS data the global analyses can present the level of variation coming from this type of parametrization. As such, in figure 82 the *DNS kre* shows the results of the global analysis prediction using the KRE fragmentation functions [46], while the *DNS kkp* is the re-

---

[10] As explained previously in the introduction section, the effect of proton proton collisions on the anti-quark distributions is minimal. The largest impact so far as been on the gluon spin contribution.

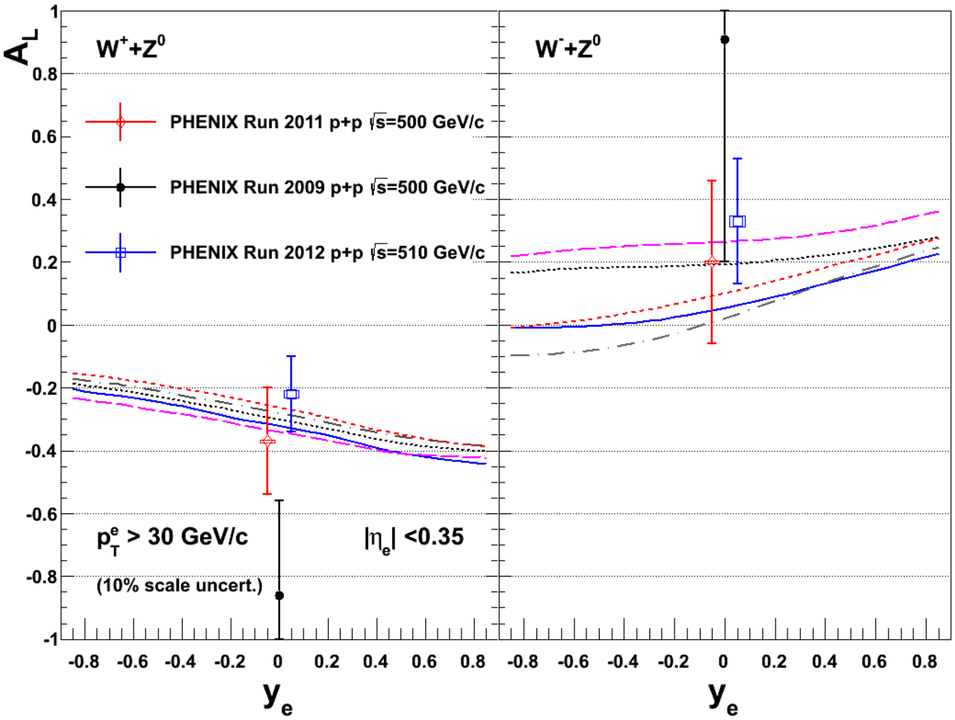

Figure 82: Single spin asymmetries for $W^+ + Z$(left) and $W^- + Z$(right) compared with theoretical predictions for the 2009 (black), 2011 (red) and 2012 (blue) data sets.

sult using the KKP fragmentation functions [47]. Both of these predictions were made using the DSSV global analysis framework. All the predictions presented take into account the Z contribution to the asymmetry.

As can be seen from the figure 82 the low statistics from the 2009 data set have been significantly improved with the 2011 and 2012 data. Furthermore, the asymmetry central values have moved in a region that is more consistent with the theoretical predictions obtained from the global analysis of previous DIS and SIDIS data.

The 2011 and 2012 results have been combined in order to obtain smaller statistical uncertainties and thus be able to compare better with the theoretical predictions. These combined data points can be seen in figure 83.

Although both the W^- and W^+ asymmetries are not centered with the

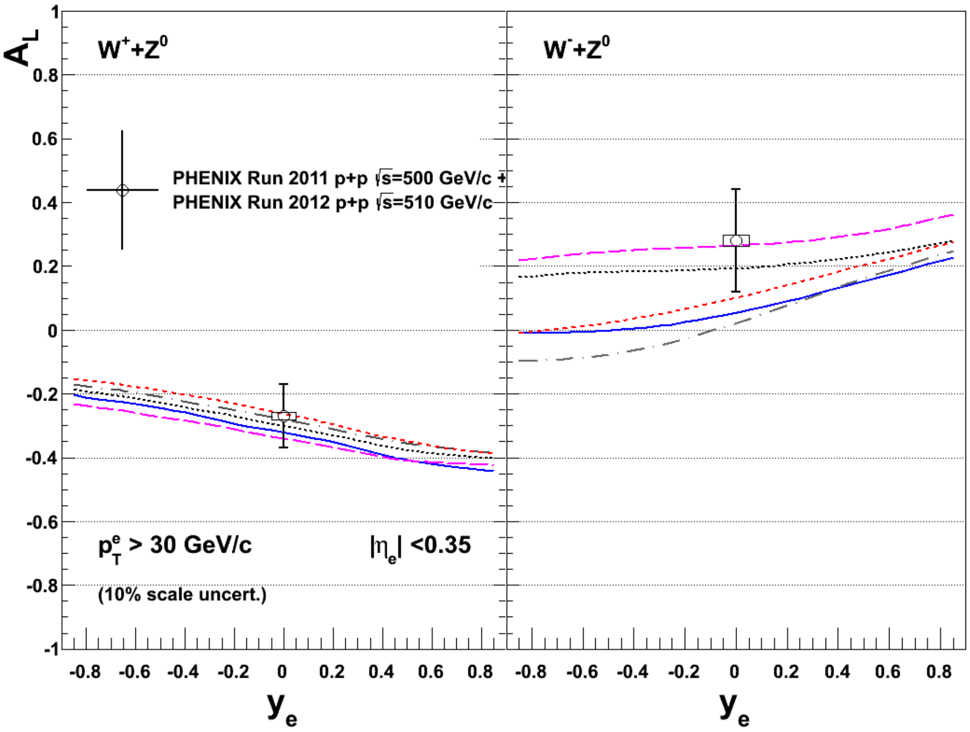

Figure 83: Single spin asymmetries for $W^+ + Z$(left) and $W^- + Z$(right) compared with theoretical predictions for the 2011 and 2012 data sets combined.

theoretical prediction in figure 83, the data is consistent with the theoretical predictions within uncertainties. This deviation will most likely have a significant impact on the central value of the best fit in future global analyses.

The measurement in this thesis has obtained for the first time a confirmation of large parity violating asymmetries at a level of 2.8σ and 1.8σ away from 0 for the W^+ and W^- respectively.

Similar measurements performed by the STAR collaboration show consistency with this measurement [48].

4.1 Future prospects

In 2013 a considerably larger data set has been obtained by the PHENIX collaboration (approximately 3 times larger than the 2011 and 2012 data set combined). An analysis modeled on the measurement presented in this thesis is being performed with preliminary results already obtained at the time of writing of this thesis. The results show very good consistency with the measurements in this thesis and with the theoretical predictions.

As mentioned before, PHENIX has the capability to perform measurements of these parity violating asymmetries at forward and backward rapidities through the muon decay channel. These asymmetries will have a larger impact on the polarized PDFs of the anti-quarks because they access directly the anti-quark distributions [6]. The impact of the RHIC data (with results from both PHENIX and STAR) can be seen in figure 84. The current (with only DIS and SIDIS data) global analysis uncertainty on the anti quark polarzied PDFs can be seen in yellow, while the uncertainty with projected RHIC proton proton data can be seen in red. Clearly, the uncertainty band in the range where these measurements are performed ($x \sim M_W/\sqrt{s} = 0.16$) will be significantly reduced with the inclusion of the W asymmetry data.

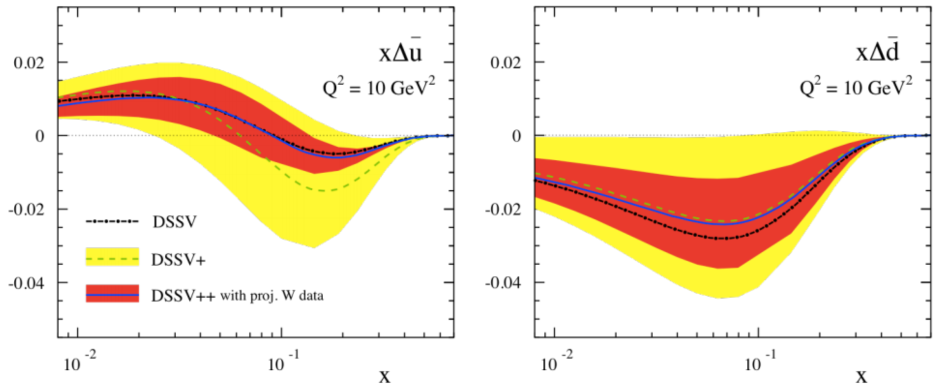

Figure 84: Polarized anti quark PDFs with DIS, SIDIS (in yellow) versus projection of all of the world data including RHIC proton proton collision data at the end of the program (in red)[8].

Appendices

A Fitting with Gaussian Process Regression

A.1 Introduction

A standard problem in statistics, known as regression, is the interpolation/extrapolation of information from a set of data points. This is generally done by assuming a functional form for the data and fitting the parameters of that functional form using either χ^2 or maximum likelihood. While these methods are well established and used extensively they have some shortcomings and there are certain types of problems for which they are not well suited. One such problem appears when there is no prior knowledge about the functional form or there is no reason to pick one functional form over another. In this appendix a method to tackle this type of problem and obtain a prediction at any point with appropriate uncertainties is presented.

Gaussian processes are a specific type of stochastic process where the variance of each of the random variables comprising the process is Gaussian. An important feature of stochastic processes is that, mathematically, they sample over the space of functions similar to how a random variable samples over a set space of possible outcomes. In defining the variances to be Gaussian, the space of possible functions is narrowed and the math needed to specify the process is simplified. Specifically, with this requirement of Gaussian uncertainties, the expectation of the process can be defined entirely in terms of a mean function and a covariance function similar to how the Gaussian distribution is defined purely by a mean and a variance.

In mapping the Gaussian process to the task of regression, the data points are interpreted as places where the "sampled" functions to go "near" or through. And by relying on Bayes' theorem, the data itself decides how "close" to the data points and the sampled functions need to be (for a given function to be assigned a probability of being in the 1σ band). This is a technique known as Automatic Relevance Determination or ARD.

It should be noted that the Gaussian process treatment of regression is not a silver bullet for all problems and it has its limitations, but for certain problems it can give a smooth functional form for complicated data complete with uncertainties with limited assumptions on the functional form underlying the data.

First a mathematical description of the method is presented, followed by an example examples using the developed implementation.

A.2 Data: From 1 to N to Infinity...

As a bridge to the mathematics of Gaussian processes, a pedagogical explanation of data and functions from a stochastic process viewpoint is given. When one is presented with a graph of a single data point, with Gaussian uncertainties, one implicitly (or explicitly) views that data point and its uncertainty as representing a Gaussian distribution. The data point can represent a series of measurements or, more aptly, for nuclear and particle physics, it represents a single measurement of a rate of a Poisson process and the uncertainty represents the expected variance of that rate for having measured the number of events you measured. Either way though, it really represents a 1-dimensional Gaussian probability distribution for the true quantity given the measured quantity, i.e. if one were to randomly sample from that distribution (or continue to make identical measurements), one would get a data point in that uncertainty band roughly 70% of the time.

Next lets imagine one has a plot with 2 data points again with Gaussian uncertainties. With 2 data points add an additional complication is presented; the data points can be related or not related. If these two data points are not related in any way, they just represent 2 independent Gaussian probability distributions or more simply, they just represent a single 2-d Gaussian distribution with no covariance (see figure 85). If the 2 data points are related though (i.e. correlated), then, when one point tends in one direction the other point must move according to how these points are related and vice-versa. And since they are probabilistic and Gaussian, one can view these two data points as being a 2-d Gaussian distribution with a non-diagonal covariance matrix (see figure 86). Another way to visual the data is to imagine the range of each measurement (typically the y-axis) as representing an independent axis for the Gaussian to vary along; therefore, for 2 data points one naturally gets a 2-d Gaussian.

To summarize a bit, one data point with Gaussian uncertainty represents a 1-d Gaussian distribution. Two data points with Gaussian uncertainties represent one 2-d Gaussian distribution, possibly with a non-diagonal covariance matrix representing how the data points move with one another. By extending this to N data points with Gaussian uncertainties, one could similarly represent this data with an N-dimensional Gaussian distribution, with the $N \times N$ covariance matrix representing how the data should move together.

So far, everything presented so far in this section is discrete, but there

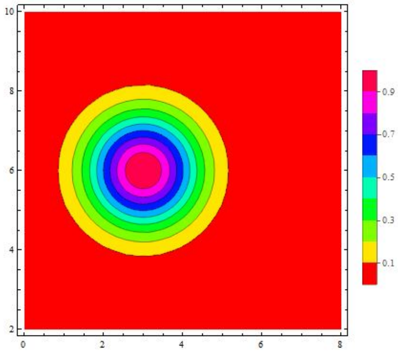

Figure 85: Two independent Gaussian distributions.

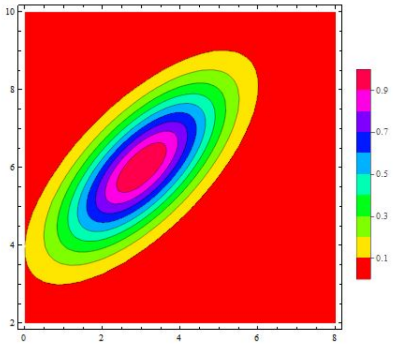

Figure 86: Two correlated Gaussian distributions.

is no reason that the motivation above only needs to apply to discrete data points. Moving from discrete to continuous, one also moves from random variables to stochastic processes. By having an uncountable infinity of data points, with uncertainties (which also can go to zero or nearly zero), one could represent this as an infinite dimensional Gaussian distribution with an infinite-by-infinite covariance matrix. Rephrasing, one could say that an uncountable infinity of data points is just a function and the uncountable infinity of uncertainties is also just a function. This is how functions arise as the sampled distribution for Gaussian processes (or uncountably infinite dimensional Gaussian distributions). Furthermore, a infinite-by-infinite covariance matrix is just another way of saying that it is a function of 2 variables. Therefore, a Gaussian processes is just an infinite dimensional Gaussian distribution with a covariance function.

A.3 Mathematical Description

A great description of the method can be found in [44], [49] or [50]. In standard nonlinear regression, given a set of **n** data points (situated at x_i with responses y_i), such that

$$y_i = f(x_i) + \mathcal{N}(0, \sigma_i^2), \tag{55}$$

where $\mathcal{N}$ is a normal distribution with 0 mean and σ_i uncertainty, one tries to get information about the function f, and after, make predictions at any other point x_{n+1}.

As intuited in the before, in a GP the relation between data points is codified through the *covariance function* (or kernel). A detailed description of different types of kernels can be found in chapter 4 of [49]. In this appendix and in the implementation the Radial Basis Function (RBF) kernel will be discussed.[11]

$$k(x_j, x_i) = \sigma_f^2 \exp\left(-\frac{(x_i - x_j)^2}{2l^2}\right) + \sigma_i^2 \delta(x_i, x_j), \tag{56}$$

where σ_i is the uncertainty on point i, $\delta(x_i, x_j)$ is the Kronecker delta and σ_f and l are hyperparameters for this covariance function. Note that the uncertainties from each point contribute only when we calculate the covariance of a point with itself.

Through the choice of form and the hyperparameters, the kernel has encoded in it the prior information about the function type: how much one point can influence another (through the characteristic length l), the amplitude of this correlation (through the σ_f parameter) and how smooth the function should be (through the differentiability of the function at 0).

Using the definition in equation 56 one can encode the covariance information from the data set into a matrix **K**:

$$K = \begin{bmatrix} k(x_1, x_1) & \cdots & \cdots & k(x_1, x_n) \\ \vdots & k(x_i, x_j) & \ddots & \vdots \\ k(x_n, x_1) & \cdots & \cdots & k(x_n, x_n) \end{bmatrix}.$$

This is a **n**×**n** matrix that will have elements on the diagonal be the largest and decrease (according to the characteristic length) as one moves to elements that are farther away (signifying that elements that have a large distance in x will influence each other less).

The next step is to calculate a prediction for a single point x_*. As before one can use equation 56 to describe the covariance of the prediction point with all the data and with itself by constructing two more objects:

$$K_* = [k(x_*, x_1), \cdots, k(x_*, x_n)] \tag{57}$$

$$K_{**} = k(x_*, x_*) \tag{58}$$

Extending the **n**-dimensional Gaussian distribution by adding the prediction point produces the response vector for our data $(y_1, \cdots, y_n, y_*)$. Then,

---

[11] However all of the math and derivations are equally valid for other kernels

the joint distribution can be written as:

$$\begin{bmatrix} \mathbf{y} \\ y_* \end{bmatrix} \propto \mathcal{N}\left(0, \begin{bmatrix} K & K_*^T \\ K_* & K_{**} \end{bmatrix}\right).$$

One of the most important features of a multivariate gaussian distribution is that any marginal distribution is in turn Gaussian. Looking at figure 86 making a vertical cut by setting the value of the x axis one is left with an 1 dimensional Gaussian distribution for the y axis. In the same way one can set the values of the input data (n points) and what is left is the conditional probability distribution for the prediction. This is called the conditional probability of y_* given the original data $\mathbf{y}$ and takes the following form (see Appendix A.2 of [49]):

$$P(y_* \mid \boldsymbol{y}) = \frac{P(y_*, \boldsymbol{y})}{P(\boldsymbol{y})} \sim \mathcal{N}(K_* K^{-1} \boldsymbol{y}, K_{**} K^{-1} K_*^T), \tag{59}$$

where the mean and variance will be the prediction:

$$\bar{y_*} = K_* K^{-1} \boldsymbol{y} \tag{60}$$

$$\mathrm{var}(y_*) = \sigma_{y_*}^2 = K_{**} - K_* K^{-1} K_*^T \tag{61}$$

The procedure relies on the covariance matrix **K** being invertible. Having only two of **n** data points being fully correlated will result in a singular matrix with a determinant of 0, which will make this procedure fail. Another note to make is that the uncertainty on the points depends only on the kernel (with it's parameters and the uncertainties from the points) and the distance of our prediction from the rest of the data.

This method can be as easily implemented with any number of prediction points (without increasing the computational time significantly) by replacing x_* with a **m** size vector of points, K_* by a **mxn** matrix and K_{**} by a **mxm** matrix; allowing one to make any number of predictions in a certain x range. Furthermore the uncertainty obtained before is now replaced by a covariance matrix that gives, besides the uncertainty of each point (on the main diagonal), the correlations between the different points.

There is one thing that has been overlooked so far: what the best hyper-parameters (θ) for the kernel function are. It can easily be seen that if the kernel parameters are not well suited for the problem the result that comes out will be useless. As is presented in detail in the references (for example subsection 45.5 in [44]) minimizing the the negative log of the posterior probability over the kernel parameters with respect to the data gives the optimal parameters. This conditional probability of θ given the data ($\mathbf{x}$,$\mathbf{y}$), $P(\theta \mid \mathbf{x}, \mathbf{y})$, can be expressed using Bayes' Theorem as:

$$P(\theta \mid \mathbf{x}, \mathbf{y}) = \frac{P(\theta) P(\mathbf{y} \mid \theta, \mathbf{x})}{P(\mathbf{x}, \mathbf{y})} \tag{62}$$

We can see here that only one terms varies with our parameters: $P(\mathbf{y} \mid \theta, \mathbf{x})$.

For a random variable $\mathbf{x}$ with responses $\mathbf{y}$, that can be described by a normal distribution $\mathbf{x} \sim \mathcal{N}(\mu, \Sigma)$ with μ being the mean and Σ being the variance (which can be shown to be the covariance function for a multivariate gaussian [51]) the probability density is known to be (as you can see in Appendix C of [51]):

$$P(\mu, \Sigma) = (2\pi)^{-n/2} (\det \Sigma)^{-1/2} \exp\left(-\frac{(\mathbf{y} - \mu)^T \Sigma^{-1} (\mathbf{y} - \mu)}{2} \right) \tag{63}$$

Considering the mean to be 0 one can derive the log of this density:

$$\log P(\boldsymbol{y} \mid \boldsymbol{x}, \boldsymbol{\theta}) = -\frac{1}{2} \left(\boldsymbol{y}^{\boldsymbol{T}} K^{-1} \boldsymbol{y} + \log(\det K) + n \log 2\pi \right) \tag{64}$$

The first term in equation 64 gives penalties for models that do not agree with the data, the second gives penalties for complex models while the third is constant.

In order to implement the optimization procedure the first and second derivatives for the RBF kernel were calculated. The first derivative of equation 64 is:

$$\frac{\partial}{\partial \theta} \left(-\log P(\mathbf{y} \mid \mathbf{x}, \theta) \right) = -\frac{1}{2} \left(\mathbf{y}^T K^{-1} \frac{\partial K}{\partial \theta} K^{-1} \mathbf{y} - \mathrm{Tr} \left(K^{-1} \frac{\partial K}{\partial \theta} \right) \right) \tag{65}$$

The second derivative is:

$$\begin{aligned} \frac{\partial^2}{\partial \theta_i \partial \theta_j} \left(-2 \log P(\mathbf{y} \mid \mathbf{x}, \theta) \right) = {} & \mathbf{y}^T K^{-1} \frac{\partial K}{\partial \theta_i} K^{-1} \frac{\partial K}{\partial \theta_j} K^{-1} \mathbf{y} \\ & + \mathbf{y}^T K^{-1} \frac{\partial K}{\partial \theta_j} K^{-1} \frac{\partial K}{\partial \theta_i} K^{-1} \mathbf{y} \\ & - \mathbf{y}^T K^{-1} \frac{\partial^2 K}{\partial \theta_i \partial \theta_j} K^{-1} \mathbf{y} - \mathrm{Tr} \left(K^{-1} \frac{\partial K}{\partial \theta_i} K^{-1} \frac{\partial K}{\partial \theta_j} \right) \\ & + \mathrm{Tr} \left(K^{-1} \frac{\partial^2 K}{\partial \theta_i \partial \theta_j} \right) \end{aligned} \tag{66}$$

Equations 65 and 66 are used in implementation to be able to derive the optimal hyperparameters by using a modified steepest descent algorithm.

A.4 Warped Gaussian Process Regression

As is described in [52], data that spans several orders of magnitude which has large varying uncertainties (and as a result different variances) may not be well described by a Gaussian Process. In this case a better solution is to transform the data through a function f, getting new points $z_i = f(y_i, \psi)$, and perform the GPR on the new dataset (ψ is the vector of parameters that determine the transformation). A standard warping in the statistical literature is to take the log of the data and assume the uncertainties will be Gaussian; bringing the uncertainties that go directly into equation 56 to the same size.

More generally, the only requirement for f is that it should be monotonic and the example presented in [52] is the neural-net style sum of tanh function:

$$f(y, \psi) = \sum_{i=1}^{M} a_i \tanh(b_i(y + c_i)) \tag{67}$$

,where M is the number of steps in the sum that needs to set beforehand. In each part of the sum a_i will set the size of the steps, b_i sets the steepness and c_i sets the offset of the step. This will allow the the integration of the warping function parameters in the optimization of the GPR, with a new log likelihood equation:

$$\begin{aligned} -\log P(\mathbf{y_N} \mid \mathbf{x}, \theta, \psi) =& \frac{1}{2}[f(\mathbf{y_N})^T K^{-1} f(\mathbf{y_N}) \\ & + \log(\mid K \mid) + N \log 2\pi - \sum_{i=1}^{N} \log \frac{\partial f(y)}{\partial y}] \end{aligned} \tag{68}$$

The uncertainty for the unwarped points can be calculated by making used of the covariance matrix that results from the GPR. In order to get the unwarped covariance matrix one simply needs to make use of standard error propagation. If one has $y_i^* = f(y_i, \psi)$ then the covariance term between points i and j will be:

$$cov_{i,j} = \frac{\partial f(y_i, \psi)}{\partial y_i^*} cov_{i,j}^* \frac{\partial f(y_j, \psi)}{\partial y_j^*} \tag{69}$$

where,$cov^*_{i,j}$ is the warped covariance term for points i and j. In the particular case where the data is warped using log, the unwarped data and uncertainty will be:

$$y_i = \exp(y^*_i) \tag{70}$$
$$cov_{i,j} = \exp(y^*_i) cov^*_{i,j} \exp(y^*_j) \tag{71}$$
$$\sigma^2_i = \exp(y^*_i) \left(\sigma^*_i\right)^2 \exp(y^*_j) \tag{72}$$

A.5 General Problem

The example that that is shown here has been taken from [53] and it's main purpose is to prove that the implementation is consistent with results from other sources. Figure 87 shows the set of 6 points with uncertainties that we can find in [53].

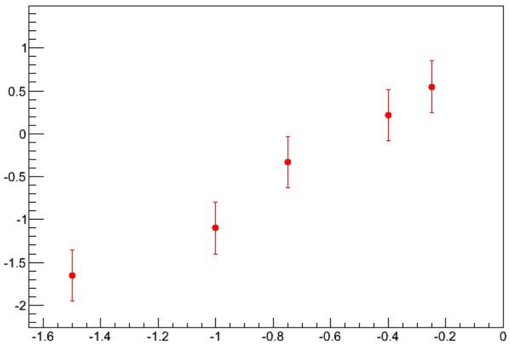

Figure 87: Input data for example.

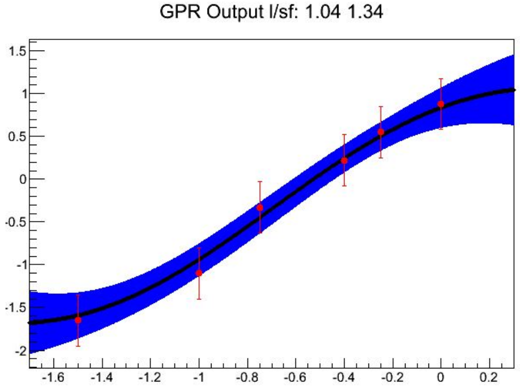

Figure 88: Predictions for example.

As explained above, one of the strong points of the GPR is that one can make predictions for a whole set of points at the same time. Figure 88 shows 1000 point between -1.7 and 0.3 each with its own uncertainty giving an overall 1σ uncertainty band (one can equally as easy construct a 95% confidence interval by increasing the size of the uncertainty bars by 1.96). The optimized parameters coming out of the implementation are very close to the ones obtained in [53].

B Local Polarimetry

Since the stable beam position in the RHIC ring is transversely polarized, in order to obtain longitudinal polarization the beam is passed through a set of spin rotators. Since the rotation of the spin direction depends quite a bit on the position of the beam in the beam pipe the spin direction must be monitored and measured constantly. The local polarimetry (performed by each of the experiments) measures the direction of a polarized beam by using the forward neutron asymmetry (as defined by equation 73).

$$A_N = \sqrt{A_{LR}^2 + A_{UD}^2} \tag{73}$$

Using the Zero Degree Calorimeter (ZDC) along with the Shower Maximum Detector(SMD)[33] as a neutron counter one can define left-right, up-down, and phi asymmetries as:

$$A_{LR/UD,b/y} = \frac{1}{P_{b/y}} \cdot \frac{\sqrt{N^{\uparrow}_{L/U} N^{\downarrow}_{R/D}} - \sqrt{N^{\uparrow}_{R/D} N^{\downarrow}_{L/U}}}{\sqrt{N^{\uparrow}_{L/U} N^{\downarrow}_{R/D}} + \sqrt{N^{\uparrow}_{R/D} N^{\downarrow}_{L/U}}} \tag{74}$$

where b/y stands for the blue or yellow beams and $N^{\uparrow}_{R/D}$ is the number of neutrons hitting the right/down part of the detector when the spin direction is up. This asymmetry can be calculated for the north or south detector representing the forward and backward asymmetries. Similarly the phi asymmetries were calculated using a phi segmentation of the face of the SMD.

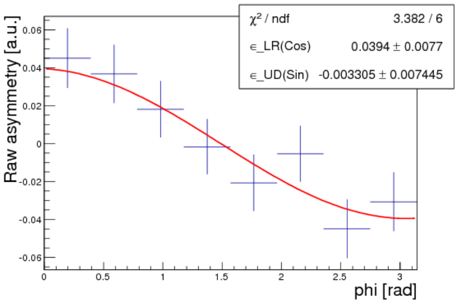

Figure 89: Phi forward raw asymmetry for the yellow beam as a function of phi angle for the transverse running.

In RHIC 2009 run PHENIX ran with longitudinal polarized beams. A calibration measurement was done with the spin rotators off to get a baseline for the left-right, up-down and phi asymmetries (see figure 89 for an example of forward transverse phi asymmetry). During the longitudinal (physics) running a small bandwidth of the data-acquisition (∼200 Hz) was reserved for the local polarmetry measurement. This data was aggregated for the whole Run and the three asymmetries mentioned above were calculated again.

With the asymmetries measured for both the transverse and the longitudinal periods one can calculate the transverse component as:

$$\frac{P_T}{P} = \sqrt{\left(\frac{A_{LR,long}}{A_{N,trans}}\right)^2 + \left(\frac{A_{UD,long}}{A_{N,trans}}\right)^2} \tag{75}$$

and subsequently the longitudinal component:

$$\tfrac{P_L}{P} = \sqrt{1 - \left(\sqrt{\left(\tfrac{A_{LR,long}}{A_{N,trans}}\right)^2 + \left(\tfrac{A_{UD,long}}{A_{N,trans}}\right)^2}\right)^2} \tag{76}$$

Because the beam can shift it's position on the face of the ZDC when the spin rotators are turned on (and during the course of the whole Run), a study was performed to estimate a systematic error for the longitudinal component of beam. Four points were selected off-center and for each of these points the left-right and up-down asymmetries were calculated for both the transverse and longitudinal running periods, giving a longitudinal component for each. In order to obtain the central value for this measurement it was assumed that the beam was centered on the face of the ZDC, and the spread of the four off-center points gave size of the systematic uncertainty.

The final results for the Blue beam and the Yellow beam during the RHIC 2009 run are as follows:

- $(0.994 \pm {}^{+0.006}_{-0.008}(\text{stat}) \pm {}^{+0.003}_{-0.010}(\text{syst}))$ Blue Beam
- $(0.974 \pm {}^{+0.014}_{-0.018}(\text{stat}) \pm {}^{+0.019}_{-0.035}(\text{syst}))$ Yellow Beam

For the 2011 and 2012 data runs a similar procedure was performed during the beam commissioning in an effort to minimize the transverse component of the beam polarization. The results for the remaining transverse components were:

- (0.060 ± 0.004) 2011 Blue Beam
- (0.054 ± 0.002) 2011 Yellow Beam

- (0.061 ± 0.006) 2012 Blue Beam
- (0.070 ± 0.008) 2012 Yellow Beam

C DC beam offset calibration

The α_{DC} is determined during the reconstruction phase of the data processing. Because of the importance of this parameter for the analysis in this thesis, special care has been take in 2011 and 2012 to have the best possible resolution for it. As can be seen from the left panel of figure 90 α_{DC} is determined as the angle between a straight track from the interaction vertex and the straight track going through the DC at 220 cm (the mid-point of the DC system). If the vertex position is shifted in either x or y (as is depicted in the right panel of figure 90) the straight track that is assumed by the DC during reconstruction is wrong and can provide a smaller or larger α_{DC} depending on the situation.

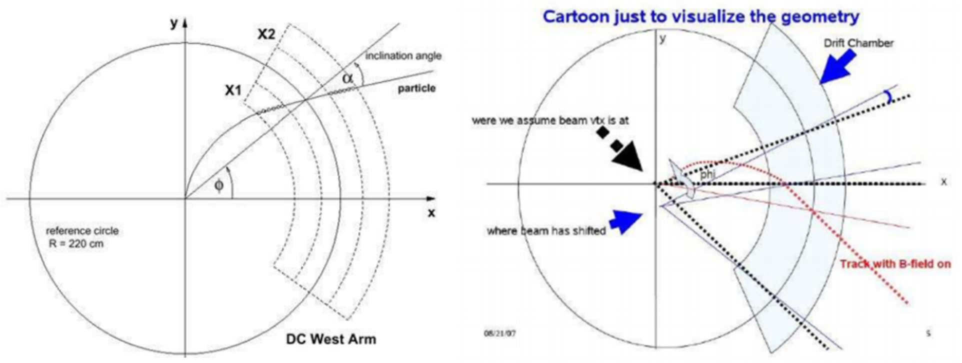

Figure 90: Left: Alpha determination diagram for the PHENIX Drift Chambers. Right: Cartoon explaination of beam offset and it's impact.

This effect is corrected through the analysis of zero field runs (data taking periods where the magnetic field of the PHENIX Central Arms is turned off). During the 2011 and 2012 data taking periods, besides weekly zero field runs, additional field off runs were taken every time one the PHENIX central arms was moved for maintenance. Each zero field run was analyzed and beam offsets were determined for each period of time. These parameters were then hard coded into the reconstruction software. For depiction purposes the analysis on a single zero field run is explained below.

As can be seen from the right panel of figure 90 there is a clear relation between the offset of the beam in the x and y plane and the α_{DC} determined at each ϕ coordinate. These deviations are called dx and dy. The relation between these parameters is:

$$\alpha_D C = \frac{dx}{220}\sin\phi + \frac{dy}{220}\cos\phi \tag{77}$$

where 220 is the nominal DC radius in cm. For both arms an independent analysis is performed and dx, dy offset parameters are determined.

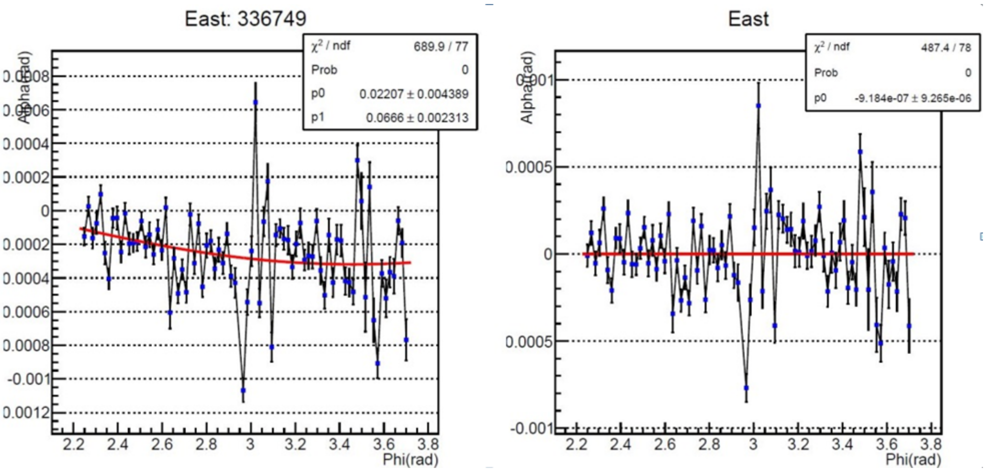

Figure 91: α_{DC} vs ϕ in the east arm for a zero field run before (left) and after (right) applying the beam offset corrections (left).

Figures 91 and 92 show α_{DC} before the correction were applied (on the left hand side) and after the corrections were applied (on the right) for one of the zero field runs. Before the beam offset parameters were applied a clear dependence of α_{DC} with ϕ can be seen. As expected after the correction, this dependence vanishes. The fluctuation that can be seen in both the before and after panels are due to DC card mis alignment. Through studies made by the DC experts it was determined that these small mis alignments would not have a large effect on the analyses and can be safely ignored. The large deviations that be seen (for example in figure 92 at ϕ of approximately -0.1)

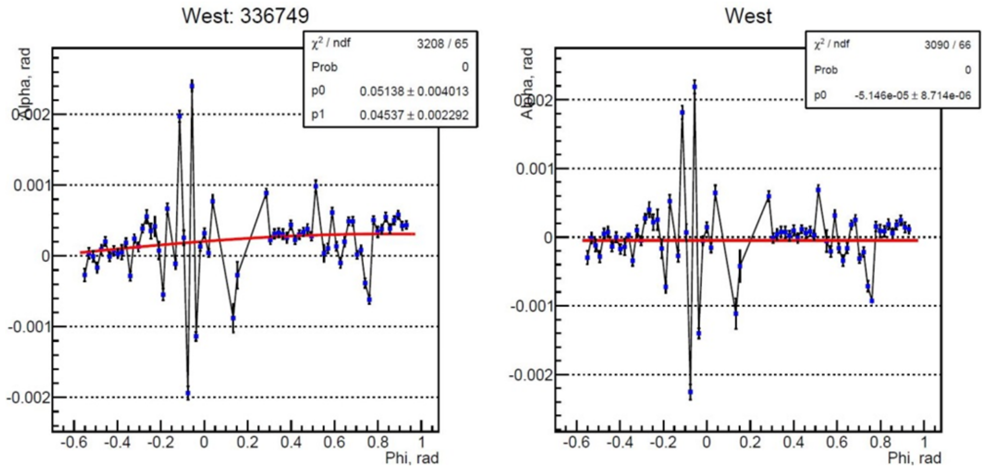

Figure 92: α_{DC} vs ϕ in the west arm for a zero field run before (left) and after (right) applying the beam offset corrections (left).

are due to severe card mis alignments. For the 2011 data (where this zero field run is from) excluding these sections of the DC does not an effect on the asymmetry analysis in this thesis. For the 2012 data, the DC experts performed a recalibration that corrected these large fluctuations.

For the 2011 data taking period 11 distinct periods were established for which beam offset parameters were determined. Similarly for the 2012 data 7 periods with their respective zero field runs were determined and analyzed.

D Maximum Likelihood plots

The maximum likelihood probability projection plots can be found below in figures 93 through 107 for the 2011 and 2012 data, double and single spin asymmetries and signal and background regions.

E Trigger Efficiency Plots

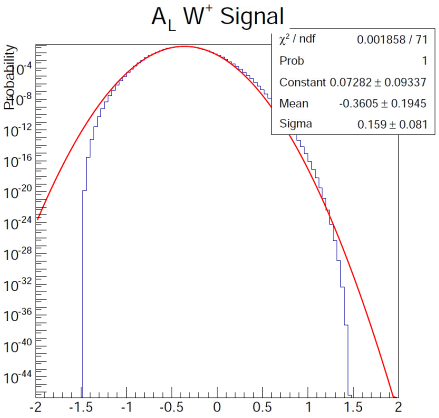

Figure 93: 2011 W$^+$ Signal single spin asymmetry.

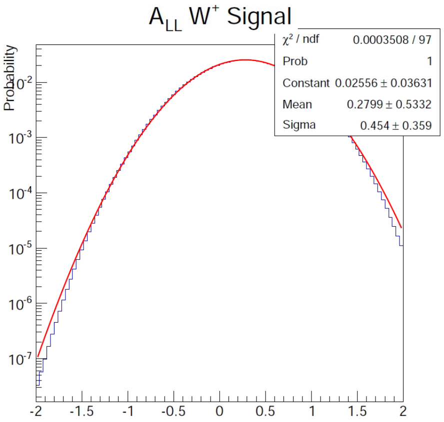

Figure 94: 2011 W$^+$ Signal double spin asymmetry.

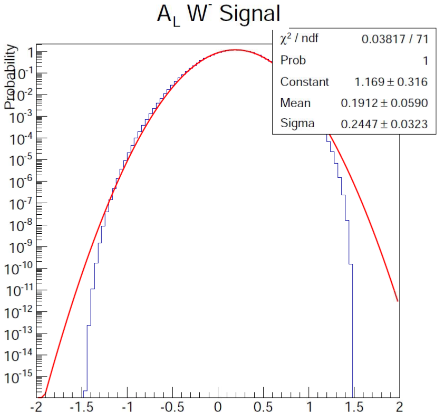

Figure 95: 2011 W$^-$ Signal single spin asymmetry.

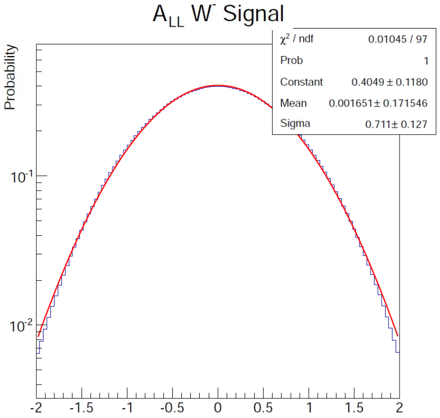

Figure 96: 2011 W$^-$ Signal double spin asymmetry.

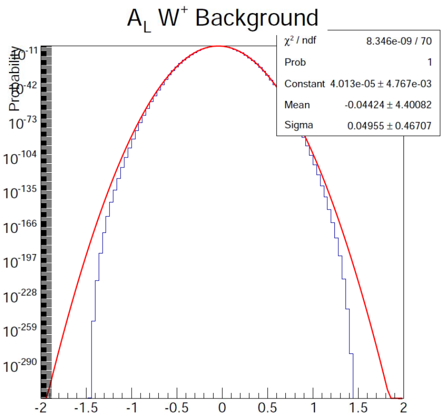

Figure 97: 2011 W^+ Background single spin asymmetry.

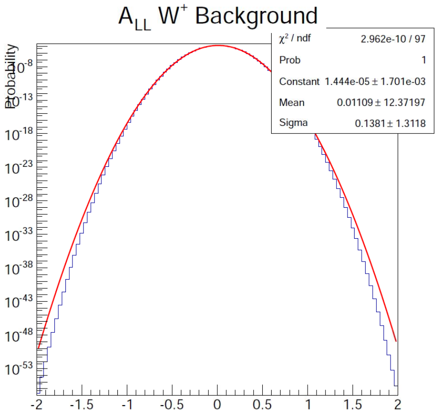

Figure 98: 2011 W^+ Background double spin asymmetry.

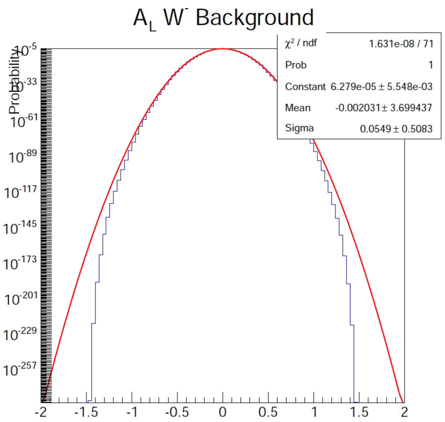

Figure 99: 2011 W^- Background single spin asymmetry.

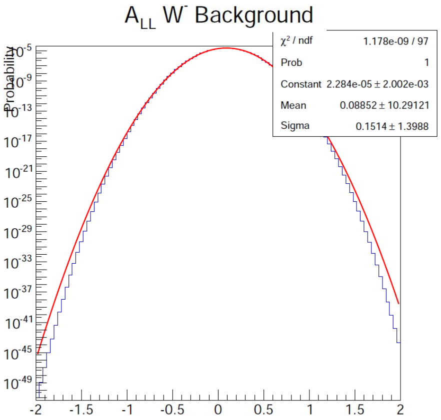

Figure 100: 2011 W^- Background double spin asymmetry.

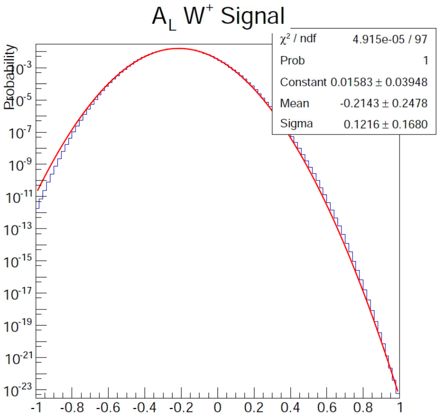

Figure 101: 2012 W^+ Signal single spin asymmetry.

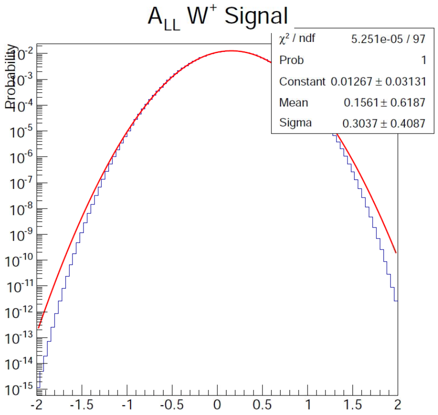

Figure 102: 2012 W^+ Signal double spin asymmetry.

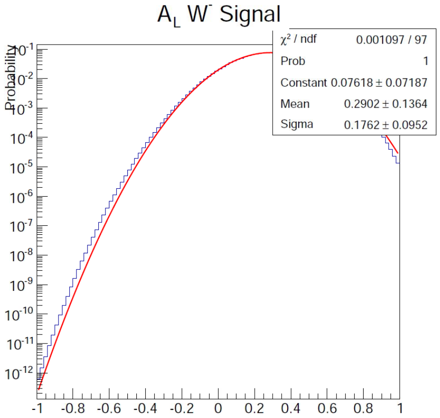

Figure 103: 2012 W^- Signal single spin asymmetry.

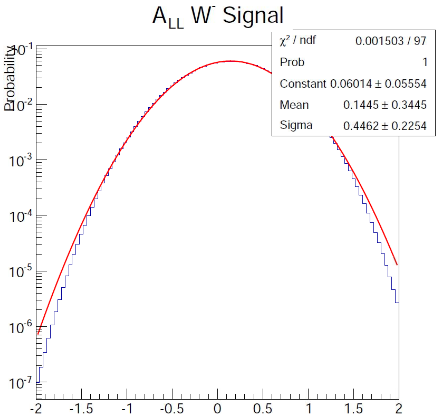

Figure 104: 2012 W^- Signal double spin asymmetry.

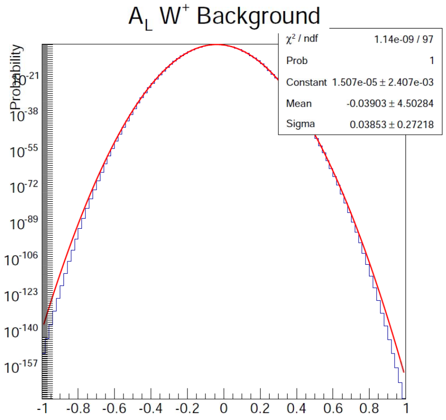

Figure 105: 2012 W^+ Background single spin asymmetry.

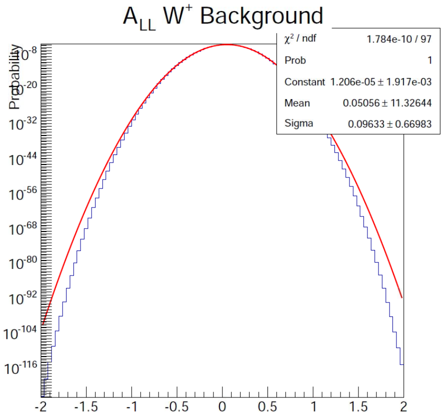

Figure 106: 2012 W^+ Background double spin asymmetry.

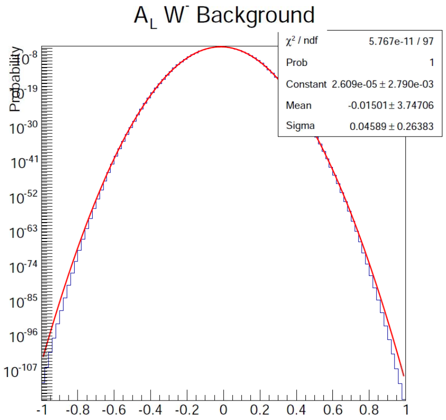

Figure 107: 2012 W^- Background single spin asymmetry.

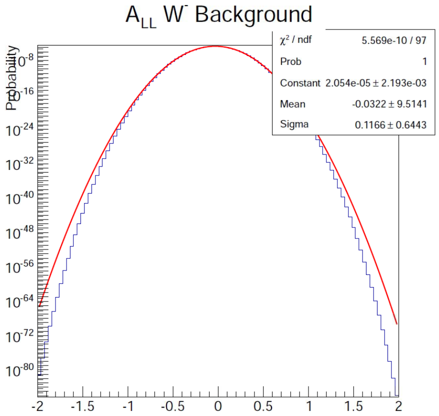

Figure 108: 2012 W^- Background double spin asymmetry.

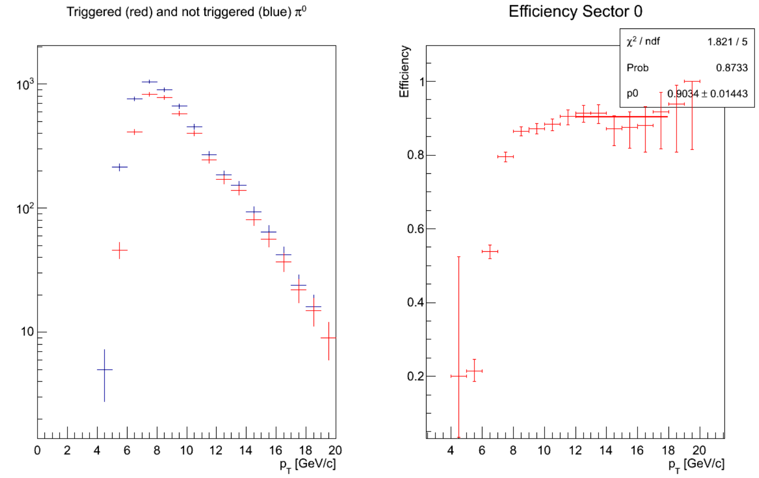

Figure 109: Left: Spectrum for π^0s with an ERT4×4 trigger (red) and all π^0s in each sector for EMCal Sector 0. Right: Efficiency calculated as the fraction of π^0s with an ERT4×4 trigger to the total number of π^0s for sector 0.

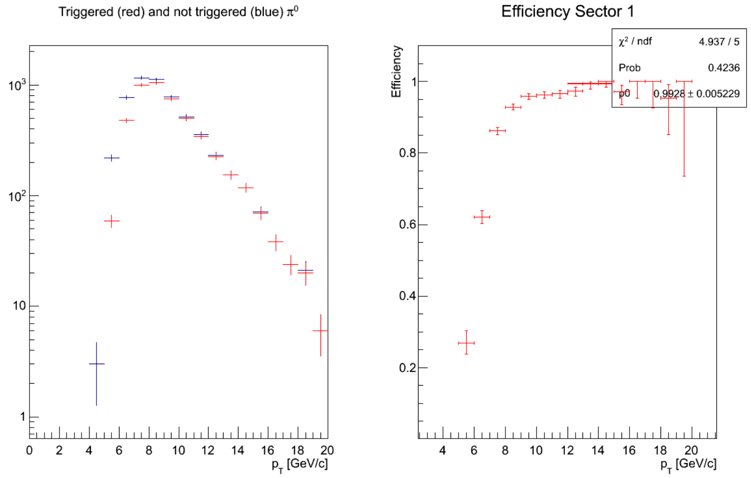

Figure 110: Left: Spectrum for π^0s with an ERT4×4 trigger (red) and all π^0s in each sector for EMCal Sector 1. Right: Efficiency calculated as the fraction of π^0s with an ERT4×4 trigger to the total number of π^0s for sector 1.

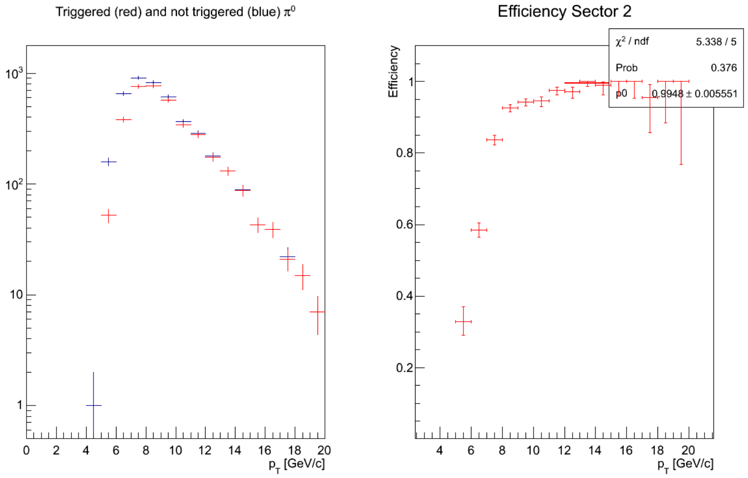

Figure 111: Left: Spectrum for π^0s with an ERT4×4 trigger (red) and all π^0s in each sector for EMCal Sector 2. Right: Efficiency calculated as the fraction of π^0s with an ERT4×4 trigger to the total number of π^0s for sector 2.

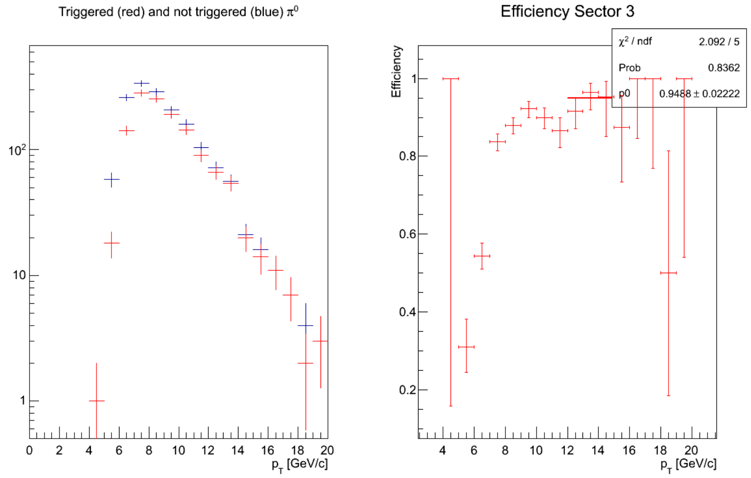

Figure 112: Left: Spectrum for π^0s with an ERT4×4 trigger (red) and all π^0s in each sector for EMCal Sector 3. Right: Efficiency calculated as the fraction of π^0s with an ERT4×4 trigger to the total number of π^0s for sector 3.

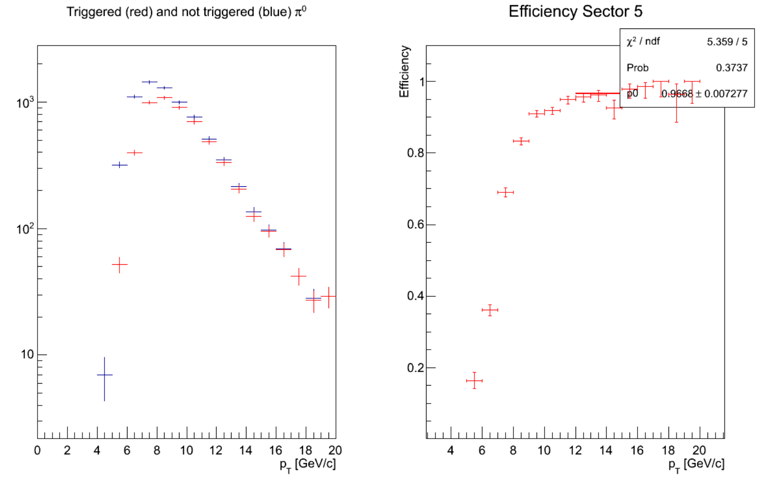

Figure 113: Left: Spectrum for π^0s with an ERT4×4 trigger (red) and all π^0s in each sector for EMCal Sector 5. Right: Efficiency calculated as the fraction of π^0s with an ERT4×4 trigger to the total number of π^0s for sector 5.

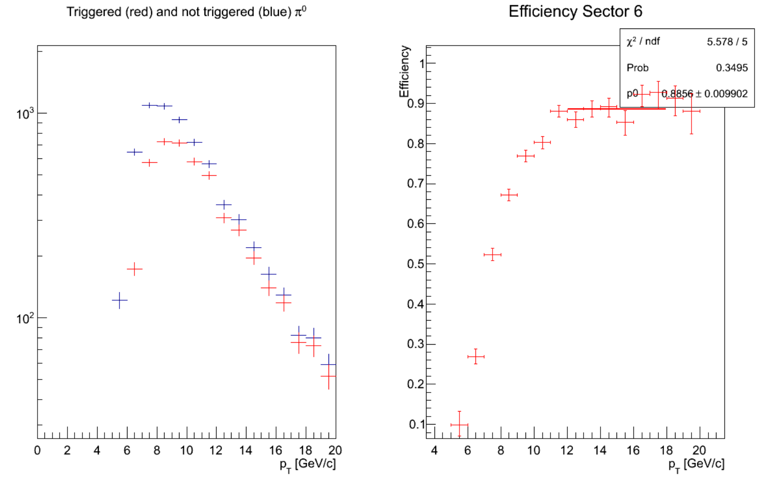
Triggered (red) and not triggered (blue) π^0

Efficiency Sector 6

Figure 114: Left: Spectrum for π^0s with an ERT4×4 trigger (red) and all π^0s in each sector for EMCal Sector 6. Right: Efficiency calculated as the fraction of π^0s with an ERT4×4 trigger to the total number of π^0s for sector 6.

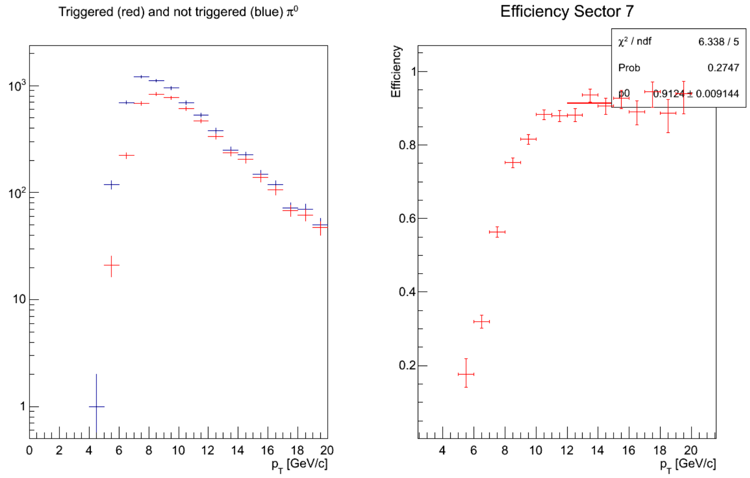

Figure 115: Left: Spectrum for π^0s with an ERT4×4 trigger (red) and all π^0s in each sector for EMCal Sector 7. Right: Efficiency calculated as the fraction of π^0s with an ERT4×4 trigger to the total number of π^0s for sector 7.

References

[1] Kieran Boyle. Measurements of the double helicity asymmetry in pion production in proton collisions at $\sqrt{s} = 200$ gev and the resulting constraints on the polarized gluon distribution in the proton, April 2014. URL `https://www.phenix.bnl.gov/phenix/WWW/talk/archive/theses/2008/Boyle_Kieran-KieranBoyleThesis.pdf`.

[2] J. Beringer et al. Review of Particle Physics (RPP). *Phys.Rev.*, D86: 010001, 2012. doi: 10.1103/PhysRevD.86.010001.

[3] J. Ashman et al. An Investigation of the Spin Structure of the Proton in Deep Inelastic Scattering of Polarized Muons on Polarized Protons. *Nucl.Phys.*, B328:1, 1989. doi: 10.1016/0550-3213(89)90089-8.

[4] Daniel de Florian, Rodolfo Sassot, Marco Stratmann, and Werner Vogelsang. Extraction of Spin-Dependent Parton Densities and Their Uncertainties. *Phys.Rev.*, D80:034030, 2009. doi: 10.1103/PhysRevD.80.034030.

[5] RHIC Spin Collaboration. W physics program at rhic, April 2014. URL `http://spin.riken.bnl.gov/rsc/report/spinplan_2008/Appendix/AppendixD.pdf`.

[6] Gerry Bunce, Naohito Saito, Jacques Soffer, and Werner Vogelsang. Prospects for spin physics at RHIC. *Ann.Rev.Nucl.Part.Sci.*, 50:525–575, 2000. doi: 10.1146/annurev.nucl.50.1.525.

[7] Kenichi Karatsu. Measurement of cross section and single spin asymmetries of w-boson production in polarized pp collisions at $\sqrt{s} = 500$ gev, April 2014. URL `https://www.phenix.bnl.gov/phenix/WWW/talk/archive/theses/2011/Karatsu_Kenichi-main.v8.pdf`.

[8] E.C. Aschenauer, A. Bazilevsky, K. Boyle, K.O. Eyser, R. Fatemi, et al. The RHIC Spin Program: Achievements and Future Opportunities. 2013.

[9] Murray Gell-Mann. A Schematic Model of Baryons and Mesons. *Phys.Lett.*, 8:214–215, 1964. doi: 10.1016/S0031-9163(64)92001-3.

[10] M. Breidenbach, J. I. Friedman, H. W. Kendall, E. D. Bloom, D. H. Coward, H. DeStaebler, J. Drees, L. W. Mo, and R. E. Taylor. Observed behavior of highly inelastic electron-proton scattering. *Phys. Rev. Lett.*, 23:935–939, Oct 1969. doi: 10.1103/PhysRevLett.23.935. URL `http://link.aps.org/doi/10.1103/PhysRevLett.23.935`.

[11] D. Griffiths. *Introduction to Elementary Particles*. Physics textbook. Wiley, 2008. ISBN 9783527406012. URL `http://books.google.com/books?id=w9Dz56myXm8C`.

[12] A. De Roeck and R.S. Thorne. Structure Functions. *Prog.Part.Nucl.Phys.*, 66:727–781, 2011. doi: 10.1016/j.ppnp.2011.06.001.

[13] Yuri L. Dokshitzer. Calculation of the Structure Functions for Deep Inelastic Scattering and e+ e- Annihilation by Perturbation Theory in Quantum Chromodynamics. *Sov.Phys.JETP*, 46:641–653, 1977.

[14] V.N. Gribov and L.N. Lipatov. Deep inelastic e p scattering in perturbation theory. *Sov.J.Nucl.Phys.*, 15:438–450, 1972.

[15] Guido Altarelli and G. Parisi. Asymptotic Freedom in Parton Language. *Nucl.Phys.*, B126:298, 1977. doi: 10.1016/0550-3213(77)90384-4.

[16] A. Airapetian et al. Quark helicity distributions in the nucleon for up, down, and strange quarks from semi-inclusive deep-inelastic scattering. *Phys.Rev.*, D71:012003, 2005. doi: 10.1103/PhysRevD.71.012003.

[17] A. Sandacz. Polarised quark distributions in the nucleon from semiinclusive spin asymmetries. 1998.

[18] John Ellis and Robert Jaffe. Sum rule for deep-inelastic electroproduction from polarized protons. *Phys. Rev. D*, 9:1444–1446, Mar 1974. doi: 10.1103/PhysRevD.9.1444. URL `http://link.aps.org/doi/10.1103/PhysRevD.9.1444`.

[19] Yoshitaka Hatta, Kazuhiro Tanaka, and Shinsuke Yoshida. Twist-three relations of gluonic correlators for the transversely polarized nucleon. *JHEP*, 1302:003, 2013. doi: 10.1007/JHEP02(2013)003.

[20] Masashi Wakamatsu. Is gauge-invariant complete decomposition of the nucleon spin possible? *Int.J.Mod.Phys.*, A29:1430012, 2014. doi: 10.1142/S0217751X14300129.

[21] Martin Leitgab. Fragmentation Functions at Belle. pages 955–958, 2012. doi: 10.3204/DESY-PROC-2012-02/64.

[22] M. Leitgab. Precision measurement of charged pion and kaon multiplicities in e^+e annihilation at $q = 10.52$ gev, April 2014. URL `https://www.ideals.illinois.edu/bitstream/handle/2142/44363/Martin_Leitgab.pdf?sequence=1`.

[23] Daniel de Florian and Werner Vogelsang. Helicity Parton Distributions from Spin Asymmetries in W-Boson Production at RHIC. *Phys.Rev.*, D81:094020, 2010. doi: 10.1103/PhysRevD.81.094020.

[24] A. Zelenski, A. Kponou, J. Ritter, A. Belov, and V. Zubets. The RHIC polarized H- source. *AIP Conf.Proc.*, 1149:847–852, 2009. doi: 10.1063/1.3215777.

[25] I.G. Alekseev, K.A. Brown, A. Dion, C.J. Gardner, T. Hayes, et al. RHIC Polarized Proton Operation. *Conf.Proc.*, C110328:41–45, 2011.

[26] F. Méot, R. Gupta, H. Huang, and N. Tsoupas. Where are the ags snakes?, April 2014. URL `http://public.bnl.gov/docs/cad/Documents/Where%20are%20the%20AGS%20snakes.pdf`.

[27] H. Okada, I.G. Alekseev, A. Bravar, G. Bunce, S. Dhawan, et al. Measurement of the analyzing power A(N) in pp elastic scattering in the CNI region with a polarized atomic hydrogen gas jet target. 2006.

[28] Hiromi Okada. Measurement of the analyzing power a_n in pp elastic scattering in the cni reagion with a polarized atomic hydrogen gas jet target, April 2014. URL `http://www.bnl.gov/userscenter/Thesis/2007/Okada_Thesis.pdf`.

[29] I. Nakagawa, I. Alekseev, A. Bazilevsky, A. Bravar, G. Bunce, et al. p-carbon polarimetry at rhic, April 2014. URL `https://www.phenix.bnl.gov/WWW/publish/shura/2009/DSPIN09/PSTP2007_itaru.pdf`.

[30] K.A. Brown, D. Bruno, A. Dion, A. Poblaguev, W.B. Schmidke, et al. RHIC Polarized Proton Status and Operation Highlights. *Conf.Proc.*, C110904:1888–1890, 2011.

[31] A. Anders, K.A. Brown, D. Bruno, A. Dion, C.J. Gardner, et al. RHIC Polarized Proton Operation in Run 12. *Conf.Proc.*, C1205201:184–186, 2012.

[32] K. Adcox et al. PHENIX detector overview. *Nucl.Instrum.Meth.*, A499: 469–479, 2003. doi: 10.1016/S0168-9002(02)01950-2.

[33] M. Allen et al. PHENIX inner detectors. *Nucl.Instrum.Meth.*, A499: 549–559, 2003. doi: 10.1016/S0168-9002(02)01956-3.

[34] L. Aphecetche et al. PHENIX calorimeter. *Nucl.Instrum.Meth.*, A499: 521–536, 2003. doi: 10.1016/S0168-9002(02)01954-X.

[35] K. Adcox et al. PHENIX central arm tracking detectors. *Nucl.Instrum.Meth.*, A499:489–507, 2003. doi: 10.1016/S0168-9002(02) 01952-6.

[36] S. Belikov, J. Hill, J. Lajoie, H. Skank, and G. Sleege. PHENIX trigger system. *Nucl.Instrum.Meth.*, A494:541–547, 2002. doi: 10.1016/ S0168-9002(02)01546-2.

[37] S.H. Aronson et al. PHENIX magnet system. *Nucl.Instrum.Meth.*, A499: 480–488, 2003. doi: 10.1016/S0168-9002(02)01951-4.

[38] K. Adcox, J. Ajitanand, J. Alexander, J. Barrette, R. Belkin, et al. Construction and performance of the PHENIX pad chambers. *Nucl.Instrum.Meth.*, A497:263–293, 2003. doi: 10.1016/S0168-9002(02) 01791-6.

[39] A. Adare et al. Cross Section and Parity Violating Spin Asymmetries of $W^{\pm}$ Boson Production in Polarized $p + p$ Collisions at $\sqrt{s} = 500$ GeV. *Phys.Rev.Lett.*, 106:062001, 2011. doi: 10.1103/PhysRevLett.106. 062001.

[40] Polarimetry Group. Polarimetry results wiki page, April 2014. URL `https://wiki.bnl.gov/rhicspin/Results`.

[41] C. Gal, K. Okada, et al. Phenix internal note 1071:mid-rapidity w boson asymmetry measurements in longitudinal polarized proton-proton collisions at *sqrts*=500 gev from rhic run 11, April 2014. URL `https://www.phenix.bnl.gov/phenix/WWW/p/info/an/1071/Run11_PHENIX_prelim_MRWA-04.pdf`.

[42] M. Stepanov. $W^{\pm}$ boson production at mid-rapidity in 500 gev p+p collisions in the phenix experiment. Presented at the APS April Meeting, 2012.

[43] A. Adare et al. Detailed measurement of the e^+e^- pair continuum in $p+p$ and Au+Au collisions at $\sqrt{s_{NN}} = 200$ GeV and implications for direct photon production. *Phys.Rev.*, C81:034911, 2010. doi: 10.1103/PhysRevC.81.034911.

[44] David J. C. MacKay. *Information Theory, Inference, and Learning Algorithms.* Cambridge University Press, New York, USA, 2003.

[45] M. Gluck, E. Reya, M. Stratmann, and W. Vogelsang. Models for the polarized parton distributions of the nucleon. *Phys.Rev.*, D63:094005, 2001. doi: 10.1103/PhysRevD.63.094005.

[46] S. Kretzer. Fragmentation functions from flavor inclusive and flavor tagged e+ e- annihilations. *Phys.Rev.*, D62:054001, 2000. doi: 10.1103/PhysRevD.62.054001.

[47] Bernd A. Kniehl, G. Kramer, and B. Potter. Fragmentation functions for pions, kaons, and protons at next-to-leading order. *Nucl.Phys.*, B582:514–536, 2000. doi: 10.1016/S0550-3213(00)00303-5.

[48] L. Adamczyk et al. Measurement of longitudinal spin asymmetries for weak boson production in polarized proton-proton collisions at RHIC. 2014.

[49] C. E. Rasmussen and K. I. Williams. *Gaussian Processes for Machine Learning.* MIT Press, Boston, USA, 2006.

[50] D. Barber. *Bayesian Reasoning and Machine Learning.* Independent, USA, 2013.

[51] S. L. Lauritzen. *Graphical Models.* Oxford University Press, USA, 1996.

[52] E. Snelson, C. E. Rasmussen, and Z. Ghahramani. Warped gaussian processes, April 2014. URL `http://papers.nips.cc/paper/2481-warped-gaussian-processes.pdf`.

[53] M. Ebden. Gaussian process regression: A quick introduction, April 2014. URL `http://www.robots.ox.ac.uk/~mebden/reports/GPtutorial.pdf`.